Engineering and Applied Science Theses & Dissertations

McKelvey School of Engineering

Summer 8-15-2021

Flexible Electronics for Neurological Electronic Skin with Multiple Sensing Modalities

Haochuan Wan
Washington University in St. Louis

Recommended Citation

WASHINGTON UNIVERSITY IN ST.LOUIS

School of Engineering & Applied Science
Department of Electrical and Systems Engineering

Dissertation Examination Committee:
Chuan Wang, Chair
Shantanu Chakrabartty
Srikanth Singamaneni
Yong Wang
Xuan Zhang

Flexible Electronics for Neurological Electronic Skin with Multiple Sensing Modalities
by
Haochuan Wan

A dissertation presented to
The Graduate School
of Washington University in
partial fulfillment of the
requirements for the degree
of Doctor of Philosophy

August 2021
St. Louis, Missouri

Table of Contents

List of Figures

ix

List of Tables

Acknowledgments

The past four years of PhD program has been and always will be a piece of unforgettable memory in my life. Throughout this journey of life I was helped, encouraged, and inspired by many people along the way. I would like to express my sincere gratitude to them all for making this dissertation possible.

First of all, I would like to thank my advisor, Dr. Chuan Wang for his continuous support, encouragement, caring and invaluable mentorship throughout my PhD study. His smart mind, immense knowledge and bright insight have always been a great guidance in my research. I also admire his great enthusiasm for life and empathy with other people. These precious qualities inspire me not only to be a better researcher, but also to be a better man. I would also want to thank my committee members Dr. Shantanu Chakrabartty, Dr. Srikanth Singamaneni, Dr. Yong Wang and Dr. Xuan Zhang for their constructive guidance and valuable feedback.

Furthermore, I would like to thank my labmates and lab alumni including Li-Wei Lo, Zhihao Xu, Junyi Zhao, Yiheng Zhang, Dr. Suoming Zhang, Dr. Jinshui Miao, Dr. Min Yu, Dr. Le Cai, Dr. Lei Zhang. My researches cannot be done smoothly without the idea sharing, discussion, assistance and advice from them. I would also like to thank my friends Huifeng

Zhu and Shuying Li from other research groups for providing valuable suggestions from different perspectives.

I would also like to thank our collaborators including Dr. Yong Wang, Dr. Shantanu Chakrabartty, Dr. Nelson Sepúlveda, Dr. Yunqi Cao, Dr. Xiaobo Tan for the guidance and fundings. Thank the IMSE staff Huafang Li, Rahul Gupta, Tyrone Daulton for their help on equipment training and operating and ESE staff for their assistance.

Last but not least, I would also like to express my deepest gratitude to my family and friends in China, especially my mother Ling Wang and my father Hui Wang, for their unconditional and endless support and encouragement throughout my years of study in United States. None of this accomplishment would have been possible without them. Thank you!

<div align="right">Haochuan Wan</div>

Washington University in Saint Louis

August 2021

Dedicated to my family and friends.

ABSTRACT OF THE DISSERTATION

Flexible Electronics for Neurological Electronic Skin with Multiple Sensing Modalities

by

Haochuan Wan

Doctor of Philosophy in Electrical Engineering

Washington University in St. Louis, 2021

Research Advisor: Professor Chuan Wang

The evolution of electronic skin (E-skin) technology in the past decade has resulted in a great variety of flexible electronic devices that mimic the physical and chemical sensing properties of skin for applications in advanced robotics, prosthetics, and health monitoring technologies. The further advancement of E-skin technology demands closer imitation of skin receptors' transduction mechanisms, simultaneous detection of multiple information from different sources, and the study of transmission, processing and memory of the signals among the neurons. Motivated by such demands, this thesis focuses on design, fabrication, characterization of novel flexible electronic devices and integration of individual devices to realize prototype biomimetic E-skin with neurological and multimodal sensing functions.

More specifically, we have studied flexible carbon nanotube thin-film transistors (CNT-TFTs) as control and signal processing units of E-skin and flexible ferroelectret nanogenerator (FENG) and triboelectric nanogenerator (TENG) as skin mechanoreceptors. Multiple fabrication methods, such as low-cost printing and conventional cleanroom-based microfabrication have been implemented to fabricate flexible CNT-TFTs with different structures and functions, especially the synaptic functions. Based on the research on individual devices, we have demonstrated a prototype force-sensing flexible neurological E-skin and its sensory nerve and synapse, with FENG serving as the sensory mechanoreceptor that generates action potentials

(pulsed voltages) to be processed and transmitted by the flexible synaptic CNT-TFT. It allows for instantaneous detection of force stimuli and offers biological synapse-like behavior to store the stimulus information and relay the stimulus signals to the next stage. The force-sensing neurological E-skin was further augmented with visual and auditory sensing modalities by introducing phototransistor-based optical sensor and FENG-based acoustic sensor. Successful transduction of visual, auditory and tactile stimuli and synaptic processing and memory of those signals have all been demonstrated. Thanks to the multimodal sensing capability of the neurological E-skin, psychological associative learning experiment-"Pavlov's dog's experiment", was also successfully implemented electronically by synergizing actual visual and auditory signals in the synaptic transistor. Flexible electronics and prototype neurological E-skin system demonstrated in this thesis may offer an entry into novel multimodal, user-environment interactive soft E-skin system for soft robotic and diagnostic applications.

Chapter 1

Background

1.1 Introduction of Human Skin and Sensory Neurons

Skin is the largest organ of human body. For an adult, skin takes up around 16% of total body weight and covers the body area of nearly 1.8 m^2. Skin shields human-being against pathogens, helps regulating body temperature and hydration, and allows the perception of physical contacts, object shapes and textures, and heat and cold. The importance of the functions of skin to the human interaction with the world cannot be overemphasized and the sophisticated functions cannot be realized without complex sensory bioreceptors and transmitting/processing nerves.

The primary sensory functions of human skin are touch sensing and temperature sensing. The reason why people can easily differentiate between a hard, smooth wood surface and a soft, rough fabric is because of the highly specialized mechanoreceptors arrays embedded in our skin. As illustrated in Figure 1.1, each of the four principal types of mechanoreceptors has distinct shape and responds to mechanical stimuli on different timescales and amplitude
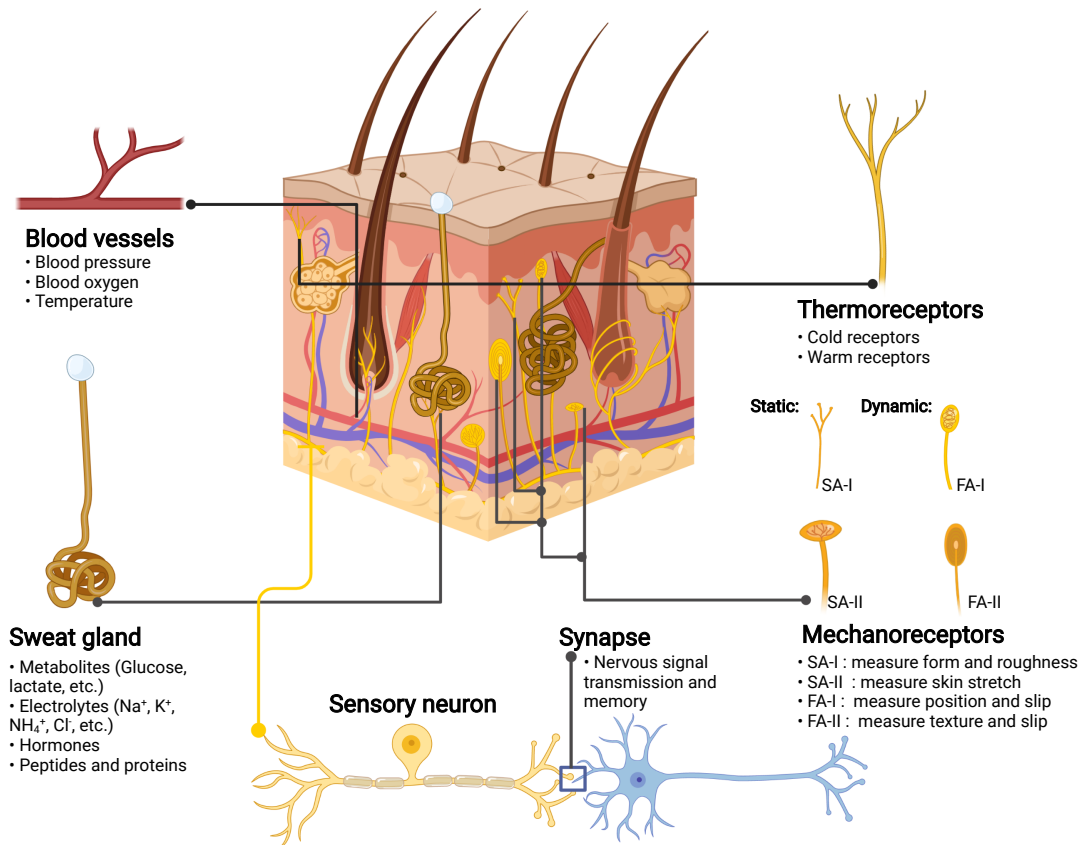
Figure 1.1: Schematic illustration of human skin structure, major biosignal sources and sensory receptors, and sensory neuron and synapse. Created with BioRender.com.

range.[1] The temperature sensory functions are enabled by cold and warm thermoreceptors, which can be more accurately described as the free nerve endings of the sensory neurons. The temperature change of the skin would induce the change of action potential firing rates of the thermoreceptors and thus causing the perception of cold or warm.[2]

After the skin sensory receptors receive stimuli, they will first transduce all different forms of stimuli into information-encoded, brain-interpretable electrical pulses called "action potentials". Depending on the type of the stimulus, the action potentials will then be passed along the axon of the afferent neurons to the dedicated cognitive areas of brain cortex to be processed. Signal communication between a sensory afferent neuron and a neuron in the brain cortex, as

well as other perceptual processes among the brain neurons, are enabled through a junction structure called synapse. The synapse, as shown in Figure 1.2, functioning as an essential
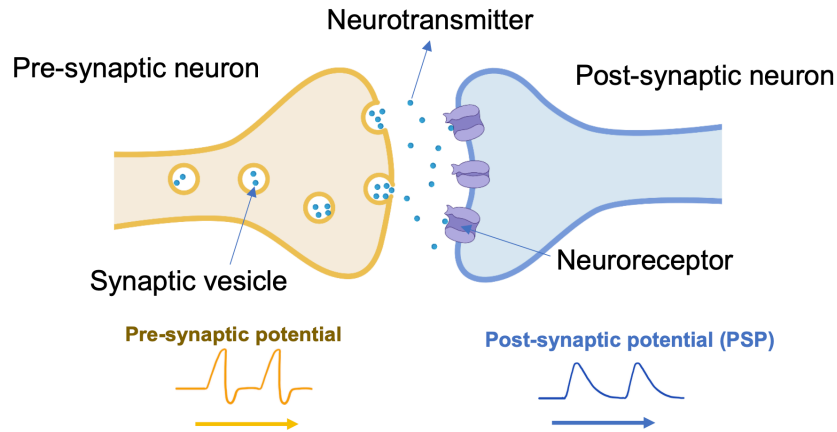
Figure 1.2: Schematic of biological synapse structure and signal communication process. Created with BioRender.com.

structure between the input (pre-synaptic) neuron and the target (post-synaptic) neuron, permits the transmission of action potentials from one neuron to another, through the releasing of the neurotransmitters from the input neuron and receiving of them at the target neuron receptors.[3] How strongly the pre- and postsynaptic cells are correlated and can exert influence over each other is evaluated by the weight of the synapse, which can evolve over time and adjust to nervous activities. The adaptation of synaptic weight to the neuron stimulus (usually in the form of action potential) is known as "synaptic plasticity". Based on how synaptic plasticity changes in response to different presynaptic action potentials, the synaptic weight can either be increased for an improved signal transmission between two cells through the synapse, decreased for a suppressed signal transmission, or simply remain

unchanged. The aforementioned three basic synaptic plasticities are named potentiation, depression, and elasticity, respectively. Moreover, the synaptic plasticity can be maintained even after the extinction of input action potentials and such behavior is widely accepted as one of the fundamental cellular mechanisms that underlies the formation of memory and learning operations in human brain.[4]

Furthermore, skin can act as a diagnostic platform that provides biological signals such as perspiration from sweat gland and vital signals (blood pressure, pulse rate, etc.) from blood vessels. These skin-based biosignals, if collected and analyzed properly, can offer critical information about the physiological condition of human body.[5, 6]

Inspired by the intriguing structure and function of human skin, over the past decade, tremendous efforts have been made to emulate skin sensory receptors, neurons and synapses electronically to build biomimetic skin systems with sensing, nervous (neurological) and diagnostic functions. Thanks to the advancement in electronic materials, microelectronic design and fabrication technologies, such artificial skin systems nowadays can finally be achieved in flexible formats similar to the actual human skin.[7] In the next sections of this chapter, the fundamental flexible electronic devices (sensors, transistors, neuromorphic devices, etc.) will be introduced. This is accompanied by a brief discussion of materials and device fabrication methods. Finally, several multifunctional neurological E-skin systems that inspire the works of this thesis will be presented and discussed.

1.2 Flexible Electronics for Sensing and Neuromorphic Processing of Electronic Skin

The realization of the biomimetic artificial skin system is based on the understanding and application of the electronic devices that constitute it. Traditionally, electronic devices based on Si technologies are often regarded as fast and precise but rigid, mechanically fragile and bio-incompatible. Biological human skin, on the other hand, exhibit high degrees of mechanical robustness that is hard to be implemented by conventional devices. With demands of mechanically compliant and multifunctional electronics for diversified flexible sensory systems, researchers have managed to develop flexible electronic devices with distinct structures and functions from a wide spectrum of materials and fabrication methods. The electronic paradigm of human skin is called electronic skin (E-skin) and was initially implemented primarily as a network of soft pressure sensors for spatial and temporal mapping of tactile information, has recently been reinforced with a variety of additional sensing modalities. By covering the E-skin related flexible electronics in this chapter, we can form an overall understanding of the E-skin systems through their fundamental components.

1.2.1 Flexible Sensors

Just as human skin, the primary function of E-skin need to be spatial and temporal mapping of tactile information. It is realized by implementing a network of soft tactile sensors. The tactile sensors can be generally classified into two catergories: passive and active. The passive tactile sensors can operate base on the change of resistance or change of capacitance with applied forces. For resistive sensor, such as pressure sensitive rubber (PSR), the resistivity of the PSR decreases with applied force.[8] For capacitive sensors, such as cross-bar structured

capacitive sensor based on PDMS, the capacitance of the sensors increases with positive pressure and decreases with negative pressure.[9] The active tactile sensors, on the other hand, can directly generate pulsed elecrtrical signal when pressed or bended. The active sensors can be categorized into three categories- piezoelectric, ferroelectret and triboelectric, according to their different operating mechanisms. Due to the active nature of the sensors, they are sometimes being referred as nanogenerators (NGs) that can also be used in mechanical energy harvesting. Piezoelectric behavior can occur in crystals that have anisotropic unit cells or in macroscopically separated regions with different charges, like dipoles, as shown in Figure 1.3a.[10] By breaking of central symmetry in the crystal structure or change the dipole moment under external force, a piezoelectric potential is formed. Ferroelectret material would exhibit similar macroscopic behavior as piezoelectric polymers or piezocomposite.[11] In Figure 1.3c, while the dipole dimension in piezoelectric polymer in is defined by the lattice parameter, dipole dimensions in the ferroelectret materials are determined by the sizes of the charged voids. Triboelectric sensor (TENG), operating through a conjunction of triboelectrification and electrostatic induction mechanism is also demonstrated in Figure 1.3b.[12] Active sensors can be readily used to convert external force stimulus to a pulsed electrical signal without the need for a power supply, and they exhibit behaviors that closely resemble skin mechanoreceptors, which are preferred for applications in neurological E-skin.

Another critical sensory function of human skin is temperature sensing that provides information of the environment to adjust body temperature and prevent injury, and it is implemented electronically by temperature sensors. Resistance-based temperature sensors utilize the resistance changes of metal such as Pt in response to temperature changes.[13] They possess the advantages of simple structure, good mechanical robustness and linearity, but suffer from low sensitivity due to the small change of resistance.[14] Organic materials, on the other hand, shows large resistance change in response to temperature change and
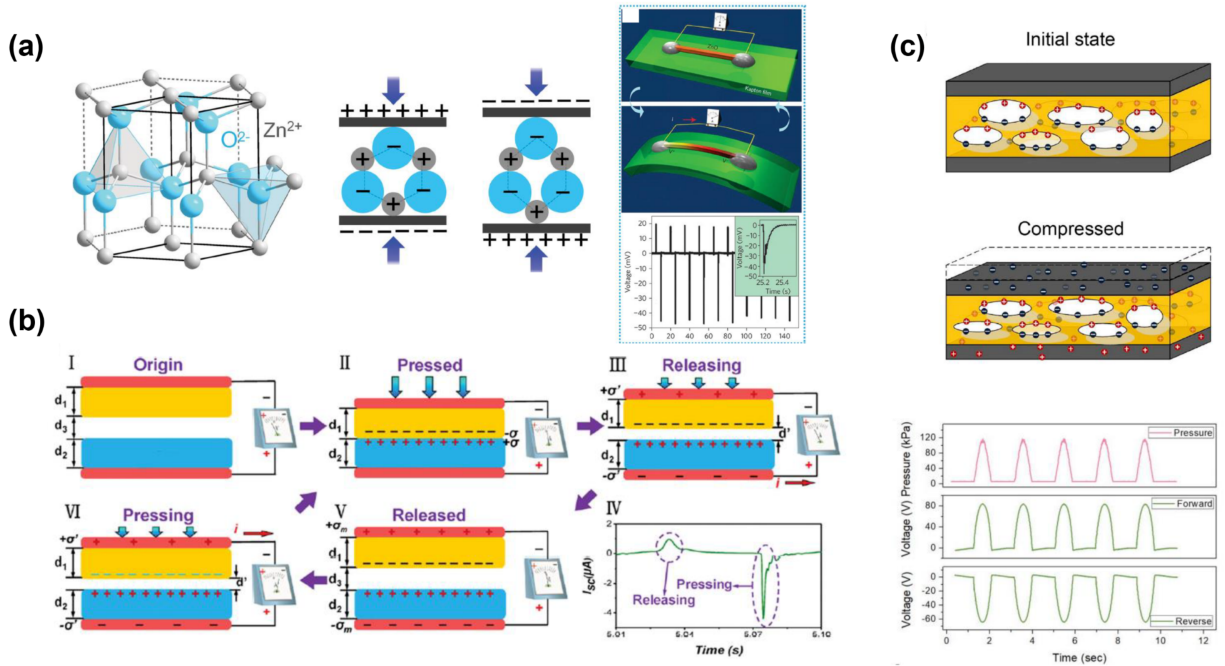
Figure 1.3: Working principle and mechano-electrical output of (a) Piezoelectric sensor (PENG). Reprinted from Ref.[10]. (b) Triboelectric sensor (TENG). Reprinted from Ref.[12]. (c) Ferroelectret sensor (FENG). Reprinted from Ref.[11].

broad sensing range,[15] can be utilized as alternatives of metals in temperature sensor design and fabrication. Moreover, semiconductor p-n junction diodes which exhibit temperature dependency have also been demonstrated to be useful in skin temperature measurement.[16]

Not only can skin be a source of biomimetic inspiration, but also can be the platform and information source for skin-based wearable electronics, thus, the concept of E-skin can be expanded into skin-based wearable electronics that collect and analyze body information from and through skin. With the development of organic electronic materials, flexible sensors that are not contained in typical human skin can be introduced into the E-skin system to realize multimodal and multiplex sensory and health monitoring functions. The development of such enhanced E-skin majorly focused on developing health monitoring, wearable E-skin systems with chemical and physical sensing abilities. One example is the wearable electrochemical sensor arrays developed by Gao *et al.* to analyze skin sweat *in situ*, as shown in Figure

7

1.4.[17] Human sweat is regarded an easily retrievable but important body fluid that contains
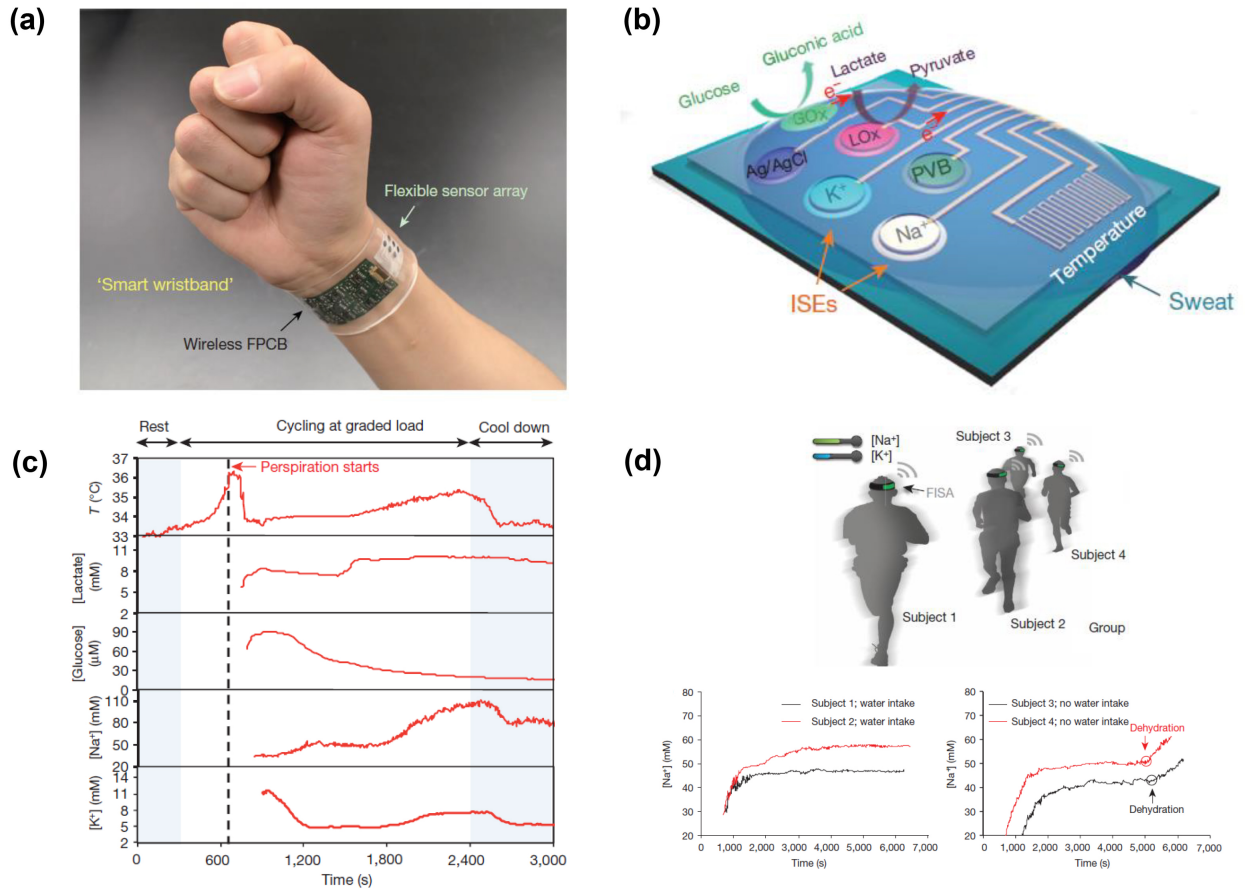
Figure 1.4: (a) Optic image of the fully integration of flexible electrochemical sweat sensors array with wireless FPCB. (b) Schematic illustration of the electrochemical sweat sensors array with sweat metabolites, electrolytes and skin temperature sensors. (c) On-body real-time analysis of sweat and body temperature during exercise using the wearable sensors array. (d) Detection of hydration status during exercise. Reprinted from Ref.[17].

a wealth of chemicals including metabolites, electrolytes, hormones, and proteins that can reflect the body's physiological state. By depositing amperometric glucose and lactate sensors with immobilized glucose and lactate oxidase enzymatic electrodes and electrolyte sensors with Na^+ and K^+ ion-selective electrodes (ISEs) on a flexible PET substrate, the sweat sensing E-skin can be wrapped around the wrist and can simultaneously, selectively and

continuously measure chemical bio-signals of sweat such as Na^+, K^+ and glucose and lactate. By further interfacing the electrochemical sensor arrays with a FPCB, the signals from the sensors even can be conditioned and processed locally and transmitted wirelessly.

Beside skin sweat, the blood vessels embedded in dermis layer can also provide some of the physical vital signs, such as body temperature, blood pressure and blood oxygen, which can also be related to the individual's health state. In the aforementioned sweat sensor array, a metal (Cr/Au)-based temperature sensor is also included in the array to monitor the skin temperature. For measuring more complex physiologic signals such as blood oxygen level and pulse rate, the collaboration of different flexible electronics are usually required. Yokota *et al.* developed a ultraflexible organic pulse oximeter that contains two color (green and red) polymer LEDs (PLEDs) and organic photodetectors (OPDs) on a 1 μm thick parylene films.[18] The three devices form the photoplethysmography (PPG) sensory system that can optically detect blood volume changes in the microvascular bed of the skin and outputs PPG waveforms that contains the information of pulse rate.[19] Moreover, by detecting the body-reflected red and green light from PLEDs with the OPDs and comparing the output PPG waveforms, the change of blood oxygen level can be readily monitored.

In short summary, by equipping the E-skin systems with a variety of flexible physical sensors and chemical sensors, multimodal and multiplex sensory functions can be achieved not only as traditional skin receptors to measure input pressure and temperature, but also as health monitoring devices to measure the detailed and dynamic body profile of the users in prolonged physical activities for the assessment of the physiological state of the individuals.

1.2.2 Flexible Transistors and Fabrication Methods

As mentioned in the last section, flexible E-skins generally consist of a network of tactile sensor and/or temperature sensors. A transistor backplane is needed to control the sensor pixels. Similar to sensors, the backplanes can also be categorized into passive matrix and active matrix. The passive matrix address the pixel with row and column signals directly through conductor lines, similar to the passive liquid crystal displays (LCDs). The active-matrix backplanes of E-skin, on the other hand, work similar to the active-matrix organic light-emitting diode (AMOLED) display. The sensors array employs an active-matrix circuitry, where each sensor pixel is connected to a thin-film field-effect transistor (TFTs) that actively maintains the pixel state while other pixels are addressed.[8] The active matrix backplane can achieve better resolution compared to the passive one by suppressing the crosstalk from other sensor pixels and will be the focus of this section. A example of TFT is presented in Figure 1.5a [20], it
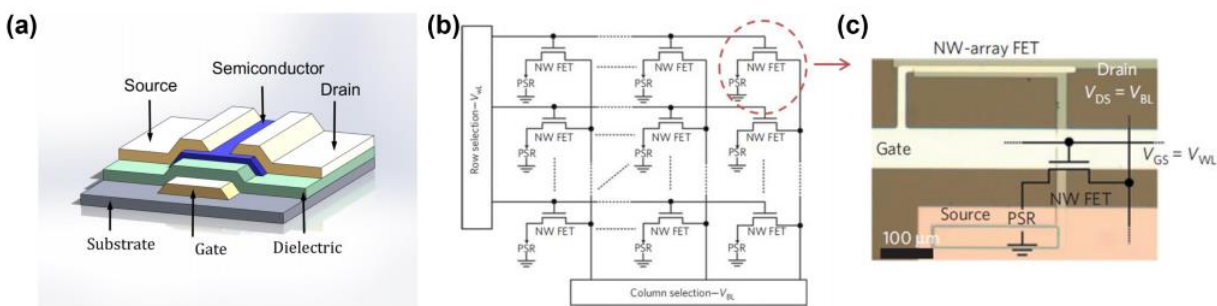
Figure 1.5: (a) Typical structure of thin-film transistor. Reprinted from Ref.[20]. (b) Circuit diagram of E-skin with integration of active-matrix backplane (TFTs array) and sensors array (PSRs array). (c) Microscopic image of one TFT in the array. (b-c) Reprinted from Ref.[8].

is fabricated by depositing thin films of metallic gate, source and drain electrodes as well as the dielectric layer and active semiconductor channel layer over a supporting insulator substrate. To render the flexibility of the TFTs, the TFTs arrays, as shown in Figure 1.5b

and c,[8] are typically fabricated on polymer thin films such as polyethylene terephthalate (PET) or polyimide (PI) through photolithographic patterning, vacuum-based deposition and etching processes. The mechanical robustness and the electrical performances (represented by field-effect mobility-μ) of the TFT are majorly limited by the semiconductor material. Among the commercialized semiconductor materials, the low-temperature polycrystalline silicon (LTPS) has high μ of over 70 cm$^2 \cdot$V$^{-1} \cdot$s^{-1}[21] but requires high temperature laser annealing which is not suitable for large-area backplane manufacturing.[22] The indium gallium zinc oxide (IGZO) has good uniformity and scalability compared with LTPS, but its μ of ~10 cm$^2 \cdot$V$^{-1} \cdot$s^{-1}[22] is regarded as moderate. Therefore, applications to large-area, high-resolution backplane of E-skins require development of methods to overcome the limitation of these semiconductor materials. For the purpose, various kinds of semiconducting materials including two dimensional semiconductors,[23, 24] organic semiconductors[25, 26] and carbon nanotubes.[27, 28, 29] Among them, the carbon nanotube is found to be attractive due to its superior carrier mobility and long-term stability.[30, 31, 32] The use of sorted high-purity semiconducting single-wall carbon nanotubes (sSWCNTs) has been demonstrated to significantly enhance the performances of TFTs.[33, 34] Moreover, the solution-processed sSWCNTs is intrinsically suitable for printed flexible TFT arrays for large-area manufacturability and low-cost applications with less demanding requirements such as disposable E-skin patches.[35] Printed sSWCNTs TFTs have been demonstrated by various printing methods such as gravure printing,[36] screen printing,[37] aerosol jet printing[38] and inkjet printing.[27, 28] The printing methods and conventional clean room-based microfabrication methods compliment each other and can expand the applications of E-skin even further.

1.2.3 Flexible Neuromorphic Devices: Memristor and Synaptic Transistors

The history of the neuromorphic devices is intriguing. The prototype of neuromorphic device-memristor, was first predicted by Prof. Leon Chua in 1971 as the fourth fundamental two-terminal (2T) circuit element besides resistor, capacitor and inductor.[39] It was not until 37 years later, in 2008, that the memristor was finally realized in experiment by Hewlett Packard Labs.[40] The behavior of memristor is contained in its own name and can be understood, although very simplified, as a resistor with memory effect. The main working principle of the memristor is the reconfiguration of resistance/conductance states of the memristor through electrical stimulation. Crucially, the programmed resistance/conductance states depend on the history of the stimulation and can be retained even the power supply is removed, creates a non-volatile memory effect. From microscopic point of view, such memory effect is caused by ion migration, phase transition and electron migration in the active layers of the memristor.[7] A representative memristor device based on ion migration mechanism is shown in Figure 1.6a,[41] the memristor has a Metal-Insulator-Metal (MIM) structure, which a cosputtered Ag-Si active layer is sandwiched between two tungsten electrodes. When a voltage bias is applied, Ag ions will move between the Ag-rich region and the Ag-poor region, thus results in the change of resistance/conductance states in Figure 1.6b.[41] The simple structure and operating mechanism of memristor make it possible to fabricate high-density neural networks with memristors in cross-bar configuration. The disadvantages of memristors, however, are the device-to-device and cycle-to-cycle variations and unstable output current.[43, 44] To address such problems, the three-terminal (3T) neuromorphic devices- synaptic transistors, have also been investigated. Figure 1.6c illustrates a representative synaptic transistor.[42] In analog to the biological synapse described in Section 1.1, in a biomimetic synaptic transistor, the gate terminal is used to imitate the presynaptic neuron, whereas the drain terminal is used to
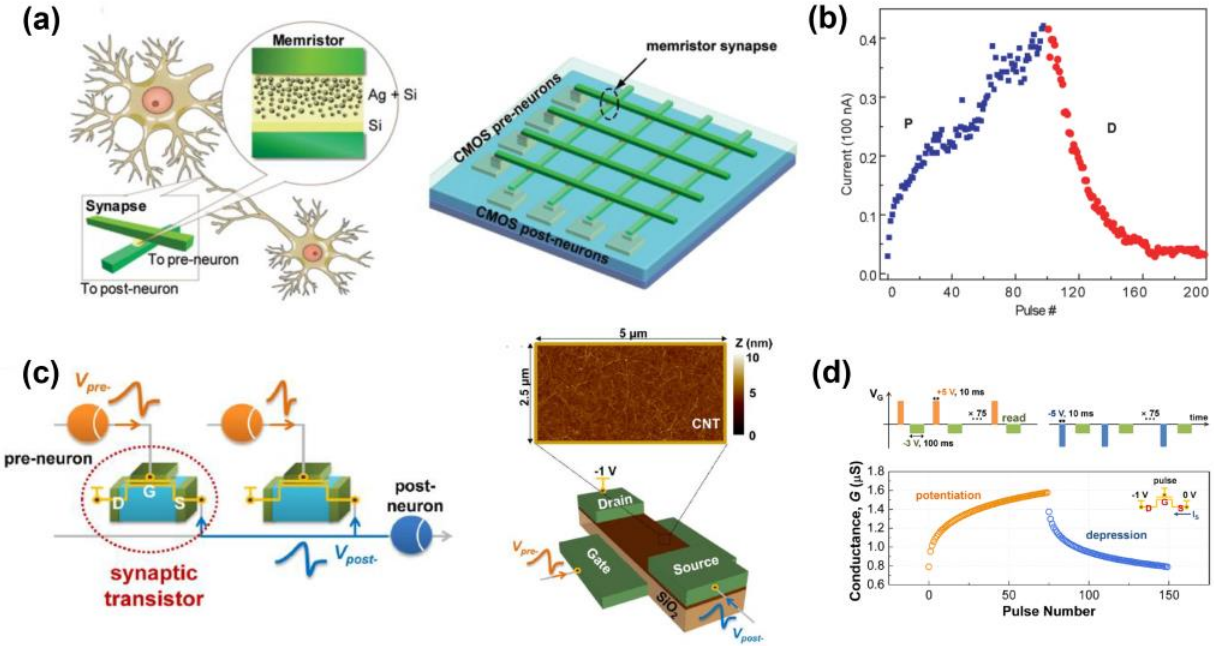
Figure 1.6: (a) Schematic illustration of metal-insulator-metal (MIM) structure memristor and cross-bar memristors array. (b) Reconfiguration of memristor conductance by potentiating and depressing electrical pulses. (a-b) Reprinted from Ref.[41]. (c) Device schematic of a CNT-based synaptic transistor and a neuromorphic processing unit consists of two synaptic transistors and a neuron. (d) Schematics of the applied potentiating and depressing electrical pulses and the reconfiguration of synaptic transistor conductance the by the pulses. (c-d) Reprinted from Ref.[42].

imitate the postsynaptic neuron. The drain-source current (I_{DS}) or the channel conductance (G) is used to represent the synaptic weight (w). Similar to memristor, the synaptic transistor is also characterized by reconfiguration of conductance states with non-volatile memory effect, as shown in Figure 1.6d.[42] The difference is that with an extra terminal, the synaptic transistor is able to process the input signal and deliver the output current via the channel layer while independently modulate its synaptic weight through the gate terminal. Also, the output current from synaptic transistor is more stable than memristor.[43]

The synaptic transistors can be implemented with different mechanisms, materials and structures. The semiconducting single-wall carbon nanotubes (sSWCNTs), as the previously

introduced as promising emerging material for TFTs backplane of active-matrix E-skin, can also be explored for neuromorphic applications with its outstanding combination of mechanical robustness,[33, 45] large on/off ratio and high carrier mobility,[31, 46] and favourable scalability. The reported works of sSWCNTs synaptic transistor can be roughly divided into three types based on their different underlying working principles- electrical-double-layer (EDL) transistors, charge trapping transistors, and floating gate transistors and some of the representative works will be briefly introduced. Peng *et al.* demonstrated a EDL-based sSWCNTs synaptic TFT by aerosol-jet printing CNT channel and spin-coating poly(pyromellitic dianhydride-co-4,4-oxydianiline) dielectric layer.[47] Under applied gate voltage, ions in the dielectric layer are driven to the surface of the sSWCNT, forming an EDL that acts as interfacial capacitors of nanoscale thickness with the sSWCNT channel. Carrier concentration, thus the conductance of the sSWCNT channel, can be effectively modulated by gate voltage through the EDL effect. And due to the high coupling efficiency of such EDL effect,[48] the operating gate voltage can be lower to a few tenths of a volt. Kim *et al.* fabricated flexible floating-gate sSWCNT synaptic transistors.[49] The Au control gate electrode is embedded in the SiO_2 dielectric layer. Charges in the channel can readily be injected into the floating gate and stored when a gate voltage is applied. By modulating the trapped charges in the floating gate, the gate voltage can effectively alters the channel conductance. The fabricated transistors can also be transferred into flexible substrates such as paper, rendering full flexibility of the transistors array.[49] Sanchez *et al.* described a wafer-scale, charge-trapping sSWCNT synaptic transistors array.[43] The highly aligned sSWCNTs were deposited on silicon wafer with a solution-based process. Owing to its 1D geometry and small physical size, the conductance of the sSWCNT is demonstrated to be highly sensitive to charged trap states in the sSWCNTs/dielectric interface.[50] Based on such phenomenon, the conductance of sSWCNT synaptic transistor can be effectively tuned by gate voltage stimulation which will change the charge distribution among the trap states. It

14

is also worth noting that in this work, the fabrication methods and materials used in making the sSWCNT synaptic transistors array is compatible with the existing CMOS technologies, which may improve the practicality of neuromorphic networks in industrial level.

1.3   Multifunctional Neurological E-skin Systems

Although a single type of device is arguably advanced in carrying out its own job, the realization of a more complex biomimetic E-skin still requires various types of devices to work together in harmony under an integrated system. Also, in some applications scenarios of E-skin such as prosthetics, wearable medical diagnosing devices and soft robotics, functions of other organs, such as neurological functions of brain or the chemical sensing functions of tongue or nose, can be incorporated into the E-skin system to extend its capabilities. In this section, some representative works of the E-skin system with multiple functionalities, especially neurological/neuromorphic functions will be briefly reviewed.

A multilayer stretchable E-skin based on ultrathin silicon nanoribbon (SiNR) mechanical and temperature sensors and metallic thermal actuators has been demonstrated by Kim's group[16] in Figure 1.7a. As illustrated in Figure 1.7b, in such a stacked structure of the E-skin, the sensors and actuators are implemented in different layers. The strain, pressure and temperature sensor arrays reside in the middle layer, and each type of the sensors adopt distinct geometrical and structural configurations (shown in Figure 1.7c), despite the same active material- SiNR is being used. Measuring multiple stimuli with same or similar sensory materials can simplify the fabrication process and potentially relieve the spacial constraints. In addition to mechanical and temperature sensing, capacitance-based humidity sensors arrays are introduced in the top encapsulating layer to monitor the skin moisture and metallic electroresistive thermal actuators arrays are embedded in the bottom layer to adjust the skin

15
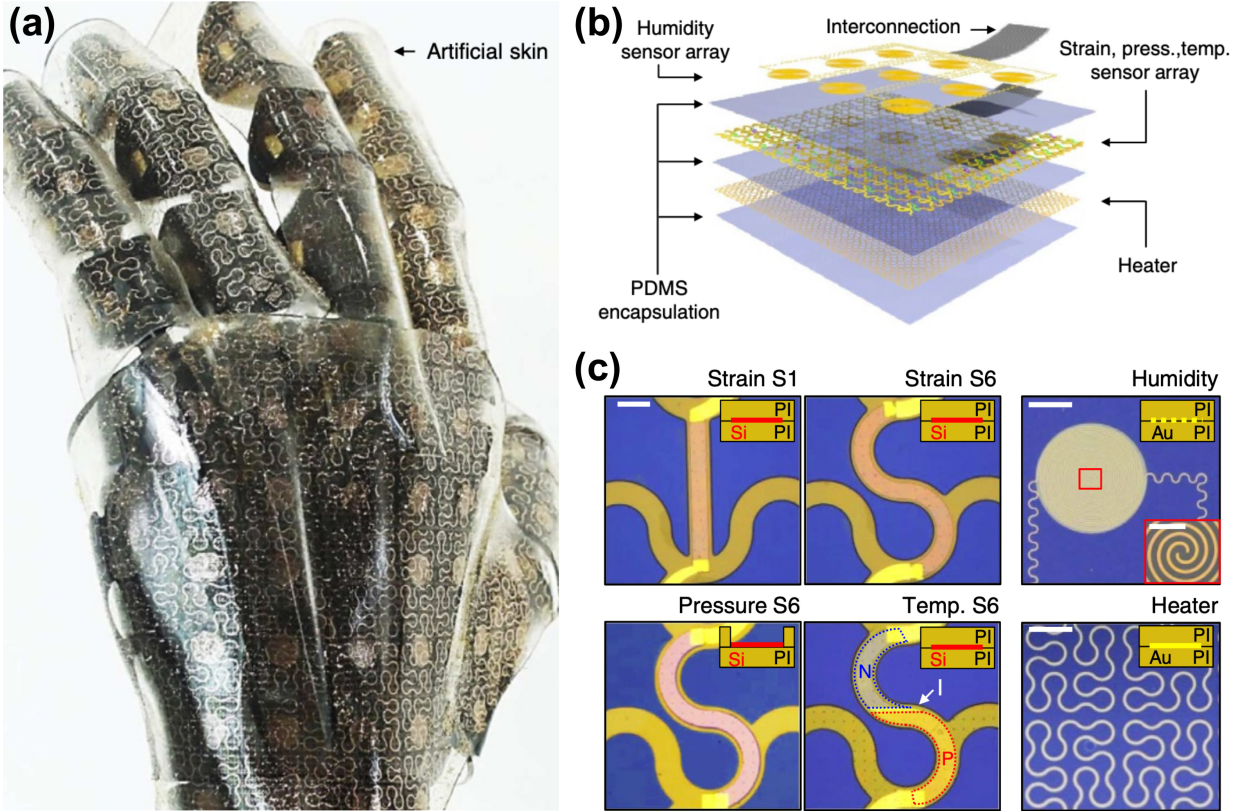
Figure 1.7: (a) Optical image of the multifunctional stretchable E-skin covering a prosthetic hand. (b) Schematic diagram showing the stacked multiple sensing and actuating layers in the E-skin. (c) Microscopic images of SiNR-based strain sensor, pressure sensor, temperature sensor and metallic humidity sensor and electroresistive heater. Reprinted from Ref.[16].

temperature, realizing a closer imitation of actual skin functions. Furthermore, by relaying the transduced tactile signals to a stretchable stimulating electrodes array and interface the electrodes with afferent nerves, the sensory signals from the pressure sensors can be transmitted to the central nervous system (spinal cord) and eventually induce the muscle responses in a rat. Such E-skin is equipped with neurological stimulation functions and can be regarded as a part of neuroprosthetic systems.

In the neurological E-skin applications, not only the sensory receptors of biological skin, but also the afferent nerves, efferent nerves and muscles and more importantly, the synaptic functions of synapses in nervous system, can be implemented electronically. Bao's group

16

reported a artificial peripheral nerve consists of pressure sensors, ring oscillators circuit and an EDL synaptic transistor, as shown in Figure 1.8a.[51] As mentioned in Section 1.1, signal
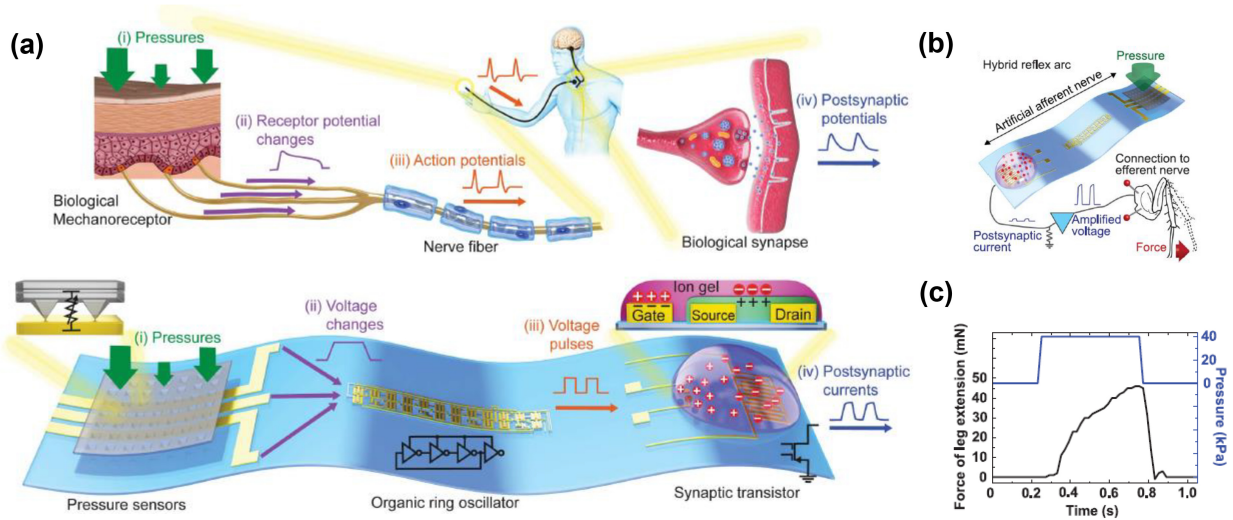
Figure 1.8: (a) Biological skin mechanoreceptors and sensory nerves in comparison with its artificial electrical counterpart consists of pressure sensors, ring oscillators circuit and an EDL synaptic transistor. (b) Interfacing artificial afferent nerve with the biological motor efferent nerves of a discoid insect's leg. (c) Detection of force of insect's leg extension in response to the tactile input to the artificial afferent nerve. Reprinted from Ref.[51].

transmission and processing in the biological nervous system through synapses are in the format of electrical spikes call "action potentials". Therefore, a biocompatiable artificial nerve will need to use spike-encoding method to match the signal form of the biological system. In this system, the resistance-based pressure sensors (PSR) are utilized as biomimetic skin mechanoreceptors. The ring oscillators circuit is connected to pressure sensors to convert the static voltage signals from the sensors into signal spikes, which are similar to action potentials. The signal spikes are then processed by the EDL synaptic transistor. Due to the EDL effect, the synaptic transistor is able to adopt a planar structure which gate and source/drain electrodes exist on same layer. Compared to the traditional stacked transistor structure, the planar EDL synaptic transistor enables the multi-gate configuration and consequentially

allows the transistor to combine signals from multiple ring oscillators. In Figure 1.8b, to demonstrate a comprehensive hybrid reflex arc, the artificial peripheral nerve is interfaced with the biological motor efferent nerves of a discoid insect's leg, and the results in Figure 1.8c show the muscle fibers of the insect's leg can be activated in response to the input pressure signals, suggesting a coherent flow of information and outstanding signal biocompatiability of the artificial nerve.

Inspired by such system, modifications and improvements of the neurological E-skins are being carried out in recent works. Shim *et al.* reported stretchable tactile sensory skins with rubbery synaptic transistors and tested both passive pressure sensors (PSRs) and active pressure sensors (TENGs) as stretchable mechanoreceptors.[52] While PSRs have simpler structures that are suitable for integrating with synaptic transistors array for spatial detection, the TENGs possess more biomimetic transduction mechanisms that the voltage spikes are generated directly in response to the tactile inputs. Also, since the sensing parts in this system is self-powered, the overall circuit design of this artificial nerves can be consequentially simplified and the total power consumption can be lowered. The processed tactile signals from synaptic transistors were used to control the locomotion of a "worm"-like soft pneumatic robots, as illustrated in Figure 1.9a. In this soft neurorobot system, the sensory skin on the top side is used to start or stop the programmed movement through synaptic (robotic) memory signals, which are represented by the number of tapping on TENG. The sensory skins on the left and right sides are designed to control the moving direction and the turning angles are also controlled by the number of tapping, as shown in Figure 1.9b. This research has achieved stretchability in neurological E-skins systems and expanded the potential applications of neurological E-skins from neuroprothestics to soft neurorobotics.

Furthermore, the sensory functions of neurological E-skins are not limited to detecting mechanical or temperature signals like biological skin. By stacking an optoelectronic synaptic
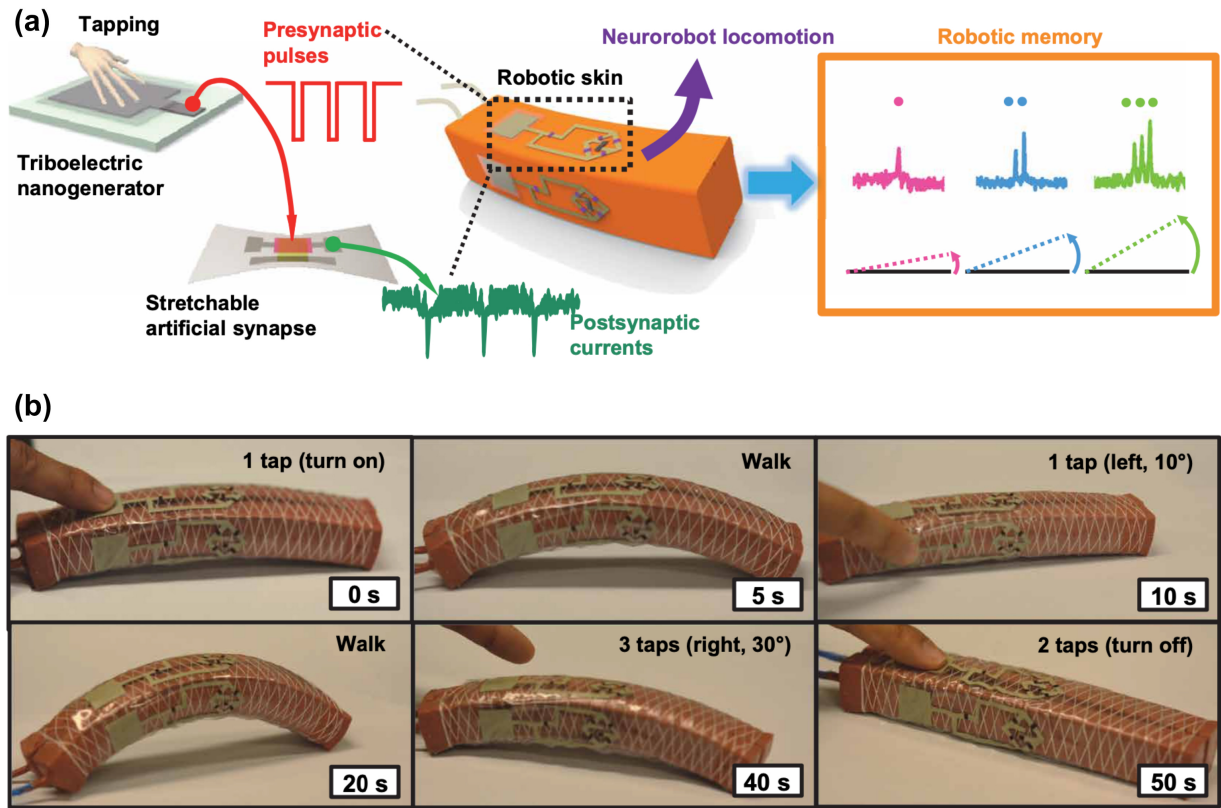
Figure 1.9: (a) Schematic illustration of the soft neurorobot with integrated TENG and synaptic transistor and its designed operations based on the synaptic (robotic) memory signals. (b) Optical images showing the programmed movements of the soft neurorobot under different commands. the Reprinted from Ref.[52].

transistor based on graphene/MoS_2 with a contact-separation mode TENGs, Yu *et al.* developed a hybrid neuromorphic device that can response to both optical stimuli and mechanical movement.[53] The performance of the synaptic transistor is evaluated by the image testing accuracy of a simulated artificial neural network (ANN). Aided by the mechanical tuning of the synaptic weights, the test accuracy can achieve as high as 92%. Although in this study, the synaptic transistor is fabricated on a rigid Si/SiO_2 substrate, the idea of detecting multiple signals from a variety of sources can inspire the development of neurological E-skin with multimodal sensing functions.

1.4 Motivation, Challenges and Contribution
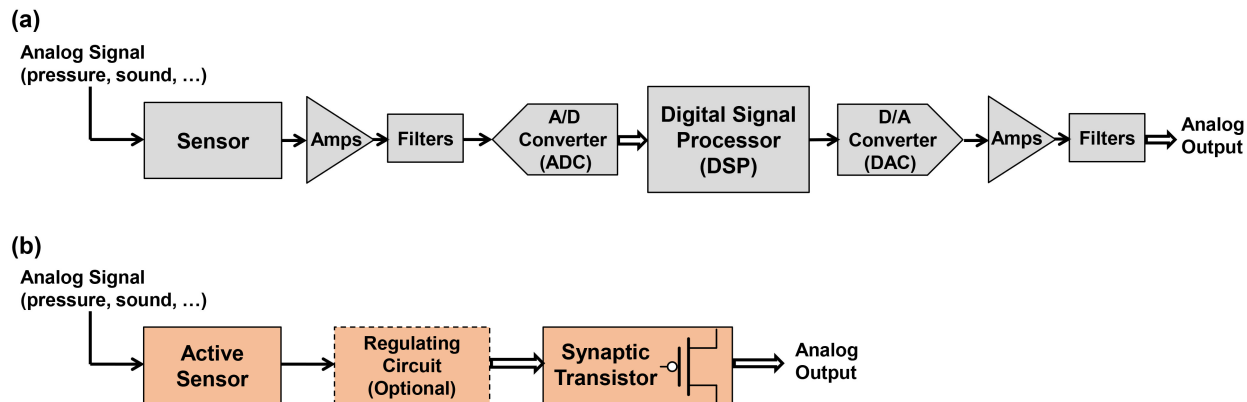
Figure 1.10: (a) Conventional digital signal processing system. (b) Neurological E-skin signal processing system.

For conventional digital signal processing system, such as pressure or sound sensing systems, the basic elements are shown in Figure 1.10a. In the sensing stage, the data is acquired by a sensor which transduces actual physical signal into analog electrical signal. Next, in the signal conditioning stage, the analog signal will go through analog amplifiers (Amps) and filters for the purpose of increasing its signal-to-noise ratio. Then, in the processing stage, the conditioned analog signal will be converted to digital signal via an analog-to-digital converter (ADC) and the signal will be processed by a digital signal processor (DSP). The processed, digitized signal can be reconstructed and re-conditioned to analog signal through a digital-to-analog converter (DAC) and amplifiers and filters. The analog signal output can be further used for applications such as display or actuation. The conventional digital signal processing system has been known for its ability to acquire, process and output information with high speed and precision, thus makes it suitable for handling sophisticated tasks. However, the conventional system is rigid and consists of complex circuits, which limits its application in skin-based system. Moreover, each stage of the conventional signal

20

processing system would consume considerable amount of power (tens of mW).[54, 55] Since the conventional system is based on central-only data processing, meaning all the data need to go through the DSP to be processed, the increase of the amount of tasks would increase the overall power consumption,[56] which further limits its application in wearable electronic system. For signal processing systems in bioinspired robotics or prosthetics, such circuit and power constraints can be eased by partitioning the tasks into sophisticated, higher-level ones and basic, lower-level ones. The lower-level tasks can be processed separately in flexible, power-efficient signal processing system, such as the biomimetic neurological E-skin. The basic elements of neurological E-skin are illustrated in Figure 1.10b. The neurological E-skin signal processing system adopts a simpler structure than the conventional digital signal processing system. In the signal sensing and conditioning stages, the active sensor will first transduce the actual physical signal into pulsed electrical signal. The active sensor can be self-powered, and the regulating circuit can potentially be simplified or even eliminated by improving the output signal level from the active sensor and lowering the operation voltage of the synaptic transistor. In this case, the power consumption in the signal sensing and conditioning stages can be lowered significantly. Next, in the signal processing stage, the synaptic transistor receives the pulsed electrical signal in its gate terminal and outputs the processed signal in the form of drain-source current. The synaptic transistor is also highly power-efficient. The reported synaptic transistors have been demonstrated to consume very low energy (<20 fJ/spike) in pulsed signal processing.[57, 58] By interfacing active sensor with synaptic transistor or by integrating them monolithically, the neurological E-skin can achieve extremely low overall energy consumption. In bioinspired robotic, while DSP in conventional digital signal processing system can be regarded the "brain" that performs higher-level tasks such as decision-making and reasoning, the neurological E-skin can be efficient in performing lower-level but crucial tasks such as reflexes, which in nature require minimum brain involvement.[59] Due to neurological E-skin's simple structure, flexibility

21

and power-efficiency, the neurological E-skin can complement the conventional digital signal processing system by conducting lower-level tasks, thus reduces the overall circuit complexity, minimizes requests for central signal processor and decrease the overall power consumption of the system.

As elaborated in Section 1.3, signal processing and control capabilities have already been demonstrated in the neurological E-skin systems. Despite the significant progress they have made, several challenges still remain to be addressed. For example, in the sensing stage, most of the sensors in current neurological E-skin systems are unable to directly generate pulsed electrical signal by themselves like skin receptors.[51, 59] They are still heavily relying on power supplies and auxiliary circuits to generate pulsed electrical signals, which can lower the overall power-efficiency of the system. Also, the auxiliary circuits are usually complex, which can potentially increase the fabrication complexity, lower the yield and increase the unit cost. In the processing stage, the dimensions of the synaptic transistors in those systems are usually large (over several millimeters in channel width),[51, 52] makes it hard to achieve miniaturized, monolithically integrated neurological E-skin. Furthermore, while most of the current neurological E-skin systems primarily focus on pressure sensing, additional sensing components can potentially be incorporated into the neurological E-skin system to enable sensory responses of stimuli in other forms.

Starting from the basic elements, we managed to make improvements to address the aforementioned challenges by promoting the flexibility, functionality and minimizing the dimension, complexity and power consumption of the neurological E-skin system. In this thesis, we developed the flexible active sensors that require no power supply to generate pulsed electrical signal. The self-powered active sensors can potentially replace the current passive sensors and their auxiliary circuits to reduce both the circuit complexity and power consumption. We also developed highly flexible, micrometer-scale synaptic transistor, which can potentially be

interfaced directly with the active sensors to form the monolithically integrated neurological E-skin. Moreover, the synaptic transistor exhibits synapse-like, non-volatile memory behavior. In the multi-sensing neurological E-skin we developed, such memory effect may not only enable lower-level functions such as motion control through artificial reflex arc, but also higher-level functions such as associative learning.

1.5   Thesis Overview

This thesis mainly focuses on the device-level study of novel flexible electronics related to the neurological E-skin applications. The study is conducted by designing, fabricating, characterizing novel flexible fundamental electronic devices, such as transistors and mechanical sensors, and demonstrating prototype biomimetic E-skins with multiple sensory and neuromorphic functions by integrating individual devices. Specifically:

Chapter 2 is dedicated to the innovative studies on active tactile sensors. In this chapter, we first examine the polypropylene-based ferroelectret nanogenerator (FENG) for its potential as multifunctional sensing device such as flexible tactile and acoustic sensor. We then demonstrate a soft, PDMS-based triboelectric nanogenerator (TENG) as active tactile sensor and/or energy harvesting device. The soft TENG device is made of screen-printed stretchable PEDOT:PSS electrodes and porous-structured PDMS thin-film. The mechanical loading test is conducted to illustrate the device's improved output performances compared with non-porous structure device and mechanism of such improvement is described.

Chapter 3 mainly discusses the research works on semiconducting single-wall carbon nanotube (sSWCNT) thin film transistor (TFT) with novel structures, functions and fabrication methods. This chapter first covers the microfabrication process of the flexible sSWCNT TFTs and some of the preliminary test results such as transfer and output characteristics of the

devices. Later in this chapter, we present fully printed flexible dual-gate sSWCNT TFTs that exhibit almost symmetric ambipolar characteristics. The dual-gate TFTs are fabricated by inkjet-printing methods and made entirely of intrinsic flexible materials. The tunable ambipolar characteristics of the dual-gate TFTs are then exploited to enable threshold voltage tuning and device polarity switching. A complementary inverter is built by integrating two printed dual-gate TFTs to demonstrate the potential application of the dual-gate TFTs in logic circuit.

Chapter 4 focuses on the synaptic functions of the flexible sSWCNT synaptic thin film transistor (TFT). In this chapter, the underlying operating mechanism of the synaptic TFT is firstly described. A systematically characterization of the synaptic functions is then carried out on the synaptic TFT. In addition, the mechanical bending and cyclic tests are also conducted on the synaptic TFT to validate its mechanical robustness. A prototype force-sensing neurological E-skin, with FENG as flexible artificial skin mechanoreceptor and sSWCNT synaptic TFT as flexible artificial synaspe, is demonstrated. The detection, transmission, processing and memory of the input tactile stimulus through this E-skin is studied later in this chapter.

Chapter 5 explores the integration of multiple sensing devices and neuromorphic device to realize the neurological E-skin with multiple sensing modalities. In this chapter, neurological E-skin (also adopts the name "sensory-memory system") with optical, acoustic and tactile sensing capabilities and synapse-like signal processing and memorizing functionalities is achieved. It is done by interfacing the FENG-based tactile sensor and acoustic sensor and phototransistor-based optical sensor with the flexible sSWCNT synaptic TFT. The synaptic weight response behavior of the synaptic TFT to different types of stimuli has been systematically studied to characterize the dynamic modification profile of the synaptic memory. Based on this system, some of the well-known psychological models and experiments,

such as the "Pavlov's dog's experiment" and the "Atkinson-Shiffrin memory model" are managed to be reproduced electronically.

Chapter 6 summarize the works of the thesis and an outlook of the future work is discussed.

Chapter 2

Soft Ferroelectret/Triboeletric Tactile Sensors (Nanogenerators)

2.1 Introduction

Rapid growth in the wearable electronics market has led to tremendous amount of new scientific discoveries and technological developments recently. The flexible electronics and stretchable electronics technologies have been extensively studied for applications in flexible/stretchable display,[60, 61, 62] smart sensing and health care devices,[9, 17, 63, 64] soft bionic devices[51] and many more. Despite the significant progress, one of the bottlenecks that researchers are still striving to address is the power source issue, which has limited the wearable device applications to a certain extent. For example, for wearable health care devices that are designed to be soft and can conformably adapt to human skin, not only the electronic circuits but also the power sources need to be soft and compliant, which is beyond the capability of existing industrial battery technologies. Soft nanogenerators based on piezoelectric,[65]

ferroelectret[66, 67] or triboeletric[68] effects, on the other hand, have been demonstrated to be highly efficient, sustainable, and low-cost for powering the wearable devices and serving as self-powered tactile sensors. Such nanogenerators can scavenge the ambient mechanical energy from ubiquitous human motion and convert the harvested energy into electricity or electrical signals.

2.2 Flexible Polypropylene-based Ferroelectret Nanogenerator (FENG)

In this chapter, we first study flexible polypropylene-based ferroelectret nanogenerator (FENG). The device structure and working mechanism of FENG are illustrated in Figure 2.1.[66] The FENG adopts a sandwiched structure which the ferroelectret polypropylene (PPFE) film is coated with Ag electrodes on both sides by sputter deposition . The charged voids insides the PPFE film are created by gas injection and plasma discharging and they serve as the highly oriented giant dipoles. A mechanical input (displacement, force, pressure, *etc.*) to the FENG will generate dipole moments across polypropylene's thickness, creating an electric field that is compensated by the accumulation of charge of opposite polarities at both surfaces of the material. This charge can be collected through thin metal film contacts on the polymer surface, resulting in an electrical current that is proportional to the rate of change in the applied mechanical input and flows in opposite directions depending on the direction of the input cycle (*e.g.*, compression/relaxation). Based on this working mechanism, FENG has been demonstrated to be efficient in generating pulsed electrical signals in response to tactile stimulus, which closely mimics the biological sensing mechanism. Moreover, due to the thin-film structure (thickness of $\sim 80 \mu$m), large electromechanical transformation efficiency (d_{33} of 300 pC/N)[69] and low Young's modulus ($\sim 1 \times 10^6$ N·mm^{-2}),[67] FENG has also
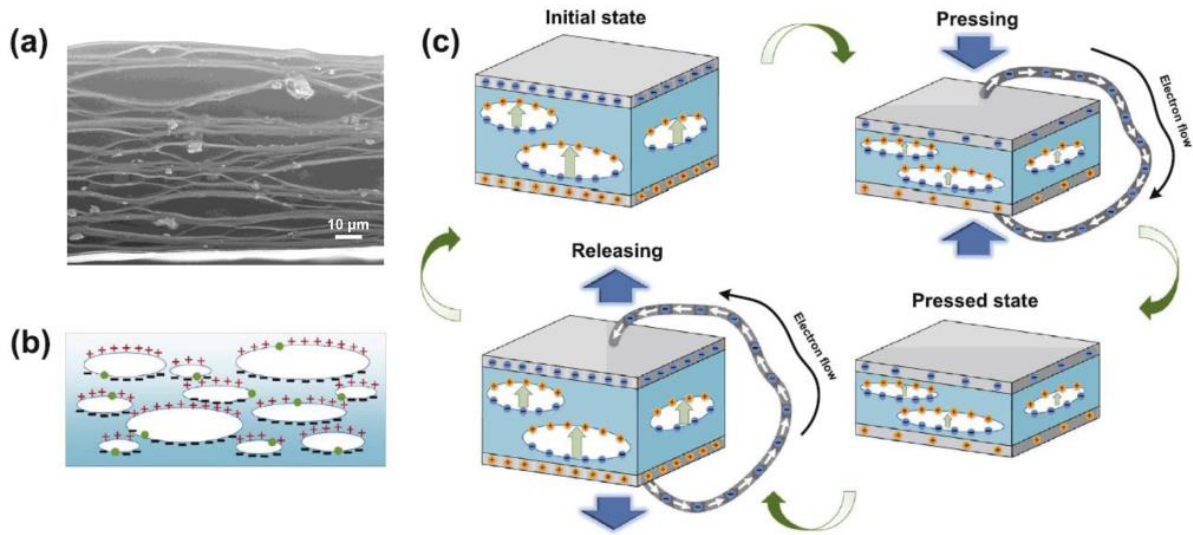
Figure 2.1: (a) Cross-sectional SEM image image of PPFE film. (b) Schematic illustration of the void-based dipoles within the PPFE film. (c) Schematic illustration of the charge generation mechanism of FENG within one compression-release cycle. (b-c) Reprinted from Ref. [66]

shown the capability as a multifunctional flexible mechanoreceptor which not only response to touch,[11] but also to sound vibration.[70] The fabrication process and characterization of FENG-based tactile sensor and acoustic sensor will be described in Chapter 5.

2.3 Soft Porous PDMS-based Triboeletric Nanogenerator (TENG)

Although the polypropylene-based FENG have exhibited outstanding flexibility and electromechanical transformation efficiency, the mechanical properties of polypropylene and sputtered Ag films will eventually limit its application as a stretchable sensor. Among the alternative approaches to constructing self-powered stretchable tactile sensor, triboelectric nanogenerator (TENG) has stood out due to its high output voltage and biocompatibility. The TENG

structure offers an extremely wide range of triboelectric material choices,[10] which renders it possible to fabricate intrinsically stretchable TENG devices by simply combining elastic triboelectric materials with stretchable conductors. Among various stretchable triboelectric materials, elastomer polydimethylsiloxane (PDMS) has been widely used in wearable TENG applications due to its high electronegativity, biocompatibility and simple processing.[71, 72] In order to increase the surface charge density, the surface of PDMS is usually texturized and one commonly studied method is the introduction of micro-sized protruding structure patterned by microfabrication.[73, 74] Nonetheless, due to the use of microfabrication, this method is limited by the sophisticated pattern design and size of wafer. Alternatively, porous PDMS film made from self-assembled microparticle template has also been demonstrated to be an effective way to further enhance the output performances of PDMS-based TENG.[75] Fabricated through a solution-based self-assembly process, such porous structure can be made over large area at extremely low cost and its structure could potentially lead to both increased surface area for friction and increased surface charge density, both of which are desirable properties for high-performance TENG applications.

Here, we demonstrate a PDMS-based TENG device with screen-printed stretchable electrode and porous PDMS thin film formed by using self-assembled polystyrene beads as the sacrificial template. The conductive polymer poly(3,4-ethylenedioxythiophene) polystyrene sulfonate (PEDOT:PSS) mixed with bis(trifluoromethane)sulfonimide lithium salt was used as the stretchable conductor and screen-printed onto the porous PDMS, which serves as both the contacting surface and as an electrode. Compared to similar TENG device made with non-porous PDMS, we have observed 2.5 times improvement in output voltage and 1.6 times improvement in output current. The scalable and low-cost fabrication process and great performance offered by the porous PDMS TENG makes it promising for a wide range of applications in wearable energy harvesting devices and tactile sensors.

2.4 Device Fabrication and Material Characterization of Soft TENG

Schematic diagrams illustrating the fabrication processes and photographic images of porous PDMS TENG are illustrated in Figure 2.2a, b and g. 50 μL of polystyrene (PS) latex microspheres water dispersion (6 μm, 2.5 wt%, Alfa Aesar) was drop-casted on Si substrate (1.2 $\times$ 1.2 cm^2), followed by heat treatment at 65 ℃ for 30 min to completely evaporate the solvent. A thin-layer ($\sim$100 μm) of PDMS (Dow Corning, Sylgard 184, 10:1) was then spin-coated (1000 rpm, 60s) on the sample and heated on a heating plate at 80 ℃ for 2.5 h to cure the PDMS. After the PDMS thin film was cured, the sample was immersed in acetone briefly to detach the PS/PDMS thin film from the handling Si substrate. The fabrication of the porous PDMS thin film was completed by completely etching away the PS beads encompassed by PDMS. This was done by exposing the PS-containing side of the PDMS thin film to O$_2$ plasma treatment (30 W, 15 s), followed by bath sonication in dimethylformamide (DMF) for 3 h and immersion in DMF at room temperature for 12 h. Figure 2.2c and d are the cross-sectional view and top view scanning electron microscopy (SEM; JEOL, JEM-7001 LV) images of the porous PDMS thin film. The results show that highly-ordered, multilayer porous PDMS structure was successfully obtained. The composite PEDOT:PSS ink was prepared by mixing commercial PEDOT:PSS conductive screen printable ink (5 wt%, Sigma-Aldrich, Inc) with 10 wt% of bis(trifluoromethane)sulfonimide lithium salt (Sigma-Aldrich, Inc) and stirring for 15 min to further increase its stretchability.[76] Next, the PEDOT:PSS electrode was screen-printed on the porous side of the porous PDMS film using a PET (Grafix, Inc.) shadow mask with opening of 8 $\times$ 8 mm^2 in area and 0.3 mm in thickness. The printed PEDOT:PSS electrode was then cured at 70 ℃ for 1 h. The SEM images of PEDOT:PSS and its interface with porous PDMS are shown in Figure 2.2e and f, respectively. After the
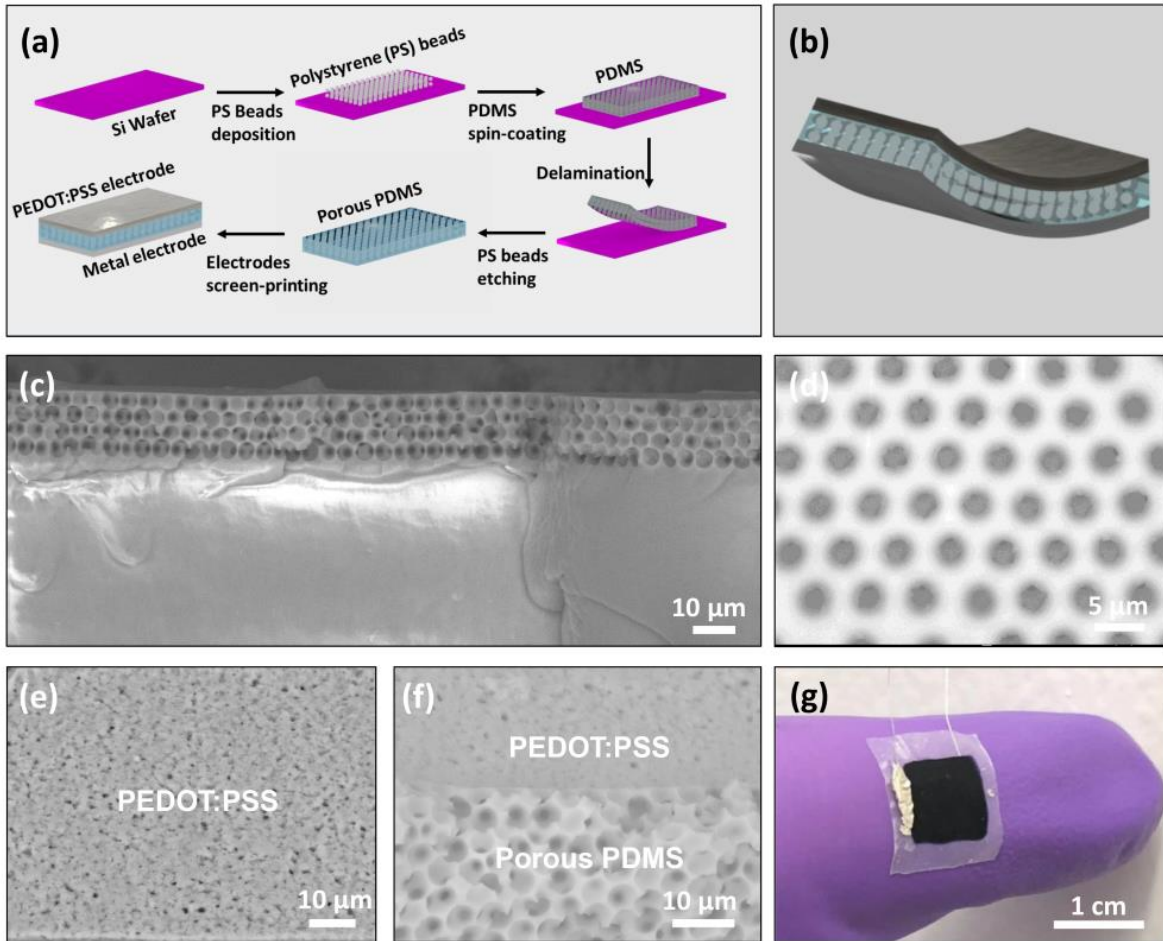
Figure 2.2: (a) Schematic illustration of the fabrication process of porous PDMS TENG device. (b) Schematic illustration of structure of porous PDMS TENG device. SEM images of porous PDMS thin film from (c) cross-sectional view (d) top view. SEM images of (e) PEDOT:PSS electrode (f) PEDOT:PSS/Porous PDMS interface. (g) photograph of fabricated porous PDMS TENG.

PEDOT:PSS electrode was cured, one edge of the electrode was connected to a leading wire using silver paint (PELCO 16062, Ted Pella, Inc.) as the adhesive. A metal electrode was fabricated on the other side (non-porous side) of the porous PDMS film using conductive nickel paste (841AR, Super Shield, Inc.) following the similar printing and wiring processes. In order to understand the effect of having porous PDMS structure on the performance of the TENG, a reference sample with entire non-porous PDMS film of the same thickness and the same device structure was also fabricated following the processes above. To confirm the template formed by PS beads has been completely etched away in the porous structure, energy dispersive X-ray analysis (EDX; JEOL, JEM-7001 LV) was conducted to the cross-sessional area of the porous PDMS structure shown in Figure 2.3a. Structural formula of PDMS and PS shown in Figure 2.3b suggest the element content of carbon in PS (92.3 wt%) is much higher than PDMS (32.4 wt%) while the element content of silicon in PDMS is 37.8 wt% and in PS is essentially zero. EDX analysis results in Figure 2.3c and d indicate that the voids in Figure 2.3a have nearly zero carbon content while the silicon content is similar to the background PDMS, which suggests that all PS beads have been completely etched away in the porous PDMS structure. It is also worth noting that the fabricated porous PDMS structure remains elastic and is highly resilient to compressive strain. SEM images of the porous PDMS cross-sectional structure before (Figure 2.3f) and after (Figure 2.3e) pressure of up to 43.6 kPa was applied show the porous structure was fully retained after compression. The electrical property and stretchability of the screen-printed composite PEDOT:PSS electrode were also characterized. A linear stretching stage shown in Figure 2.3g was used to apply tensile strain to a sample with PEDOT:PSS electrode, whose electrical resistance was measured under various levels of applied strain. As reported in our previous paper,[9] the addition of salt could render the PEDOT:PSS electrode to become stretchable. This is confirmed by the results presented in Figure 2.3h, which shows that the resistance variation of the PEDOT:PSS electrode is less than 10 Ω under strain of up to 20 %.
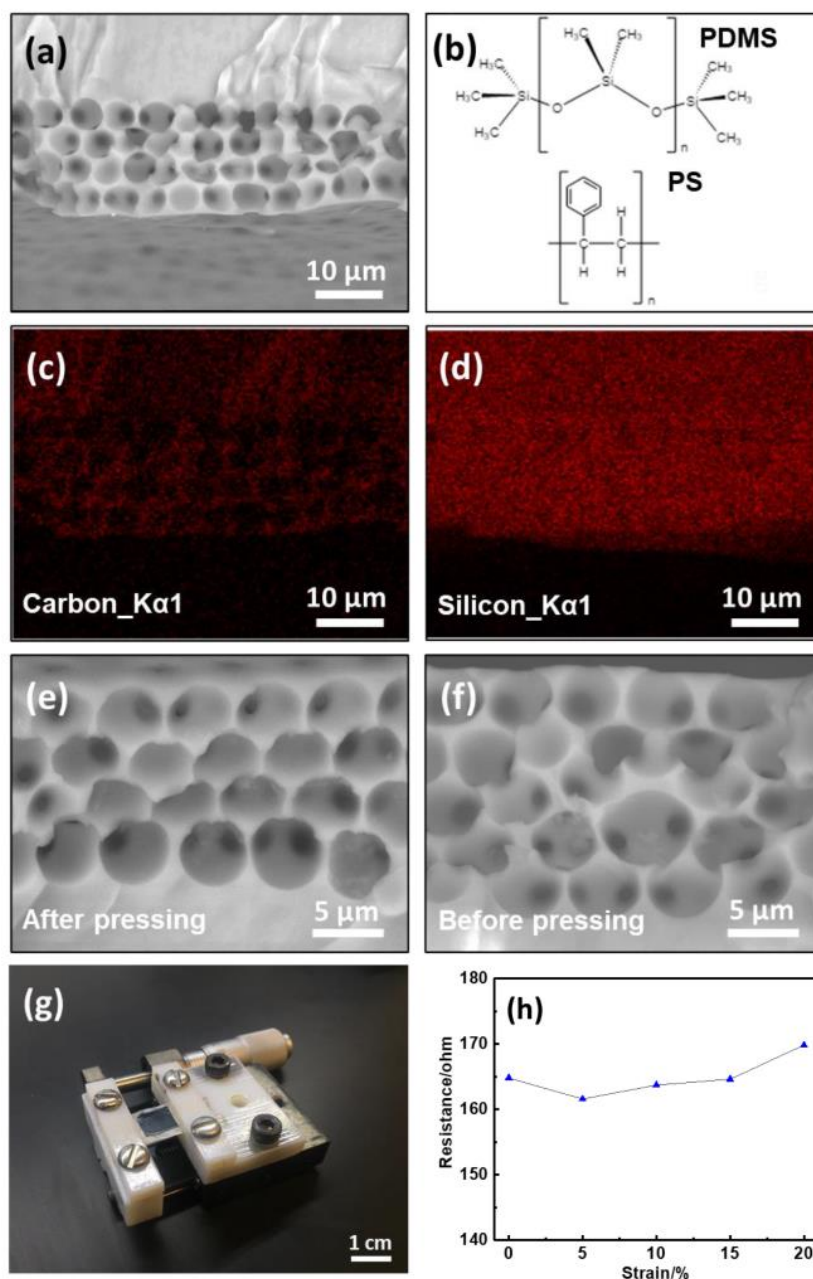
Figure 2.3: (a) SEM image of porous PDMS structure examined in EDX. (b) structural formula of polydimethylsiloxane (PDMS) and polystyrene (PS). Energy dispersive X-ray analysis (EDX) images of (c) carbon element and (d) silicon element of porous PDMS structure. SEM images of porous PDMS structure (e) after compressive pressure (f) before compressive pressure. (g) Stretching test equipment setup. (h) Resistance change of screen-printed PEDOT:PSS under applied strains.

2.5 Working Mechanism of Soft TENG

As shown in Figure 2.4, the charge generation mechanism of porous PDMS TENG device can be explained by tribo-electrification and electrostatic effect[71, 75, 77] between tribo-positive PEDOT:PSS electrode and tribo-negative PDMS layer. Initially the PEDOT:PSS electrode is separated from non-porous PDMS surface by porous PDMS layer. When the TENG device is being pressed for the first time, PEDOT:PSS is brought into contact with non-porous PDMS surface, the friction of two materials causes the separation of triboelectric charges with different polarity, where positive charges accumulate on PEDOT:PSS and negative charges accumulate on non-porous PDMS surface due to different electron affinity of the material.[78] Under this situation, the negative charges on the non-porous PDMS is balanced entirely by the positive charges on top PEDOT:PSS electrode and electrostatic equilibrium is achieved. After the loading force is released, the deformed porous PDMS layer gradually restores to its original shape, giving rise to a large dipole moment through electrostatic effect, which resulting in an electrical potential difference created between the top and bottom electrode. Since the top PEDOT:PSS electrode has higher potential than the bottom electrode and two electrodes are connected through an external load, this potential difference would drive electrons to flow from bottom electrode to top electrode, generating electrical current in the load. When the TENG is pressed again, an inversed potential difference will be created between the two electrodes, which results in the transfer of electrons from top to the bottom electrode and generates current flow in the reverse direction. For the reference non-porous PDMS TENG, the charge generation mechanism is similar. However, compared with the porous PDMS, the non-porous PDMS layer has less frication area with PEDOT:PSS and higher Young's modulus, which leads to its different output performance from porous PDMS TENG.
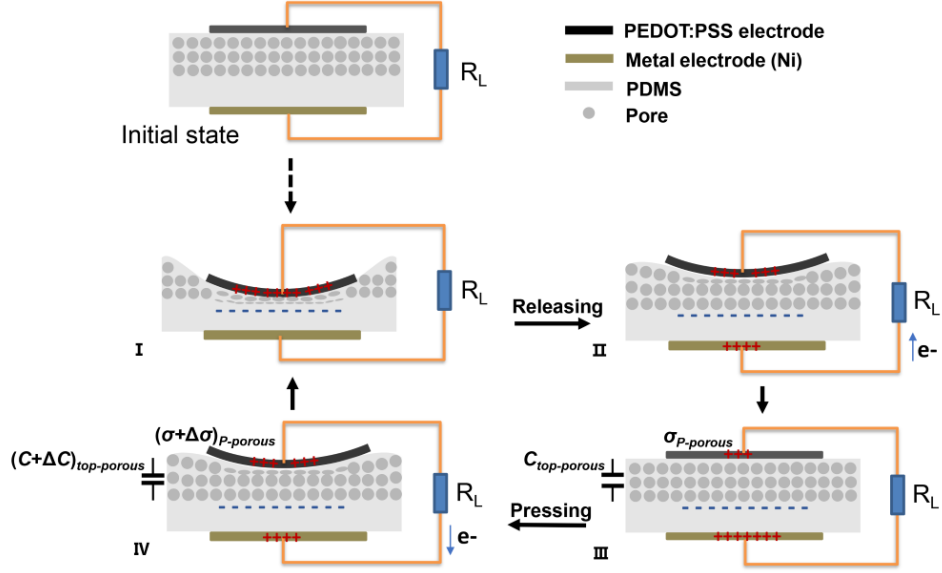
Figure 2.4: Charge generation mechanism of the porous PDMS TENG under external compressive force.

For sandwich-structured TENG device working in contact-separation mode, the nanogenerator acts as both energy output device and energy storage device which operates similarly as a parallel-plate capacitor. The porous PDMS layer has lower elastic modulus than non-porous PDMS,[75] and thus would exhibit larger displacement under the same compressive force, resulting in greater reduction in distance (Δd) between the two electrodes of the capacitor. Meanwhile, the dielectric constant of PDMS ($\epsilon_{r\ PDMS}$=2.7) is nearly three times higher than air ($\epsilon_{r\ air}$= ϵ_0 =1). When the porous PDMS layer is compressed, air will be expelled out of the porous layer and the deformed pores will lead to denser PDMS composition in porous layer and thus results in higher dielectric constant ($\Delta\epsilon_r$). Therefore, with the same loading force and frequency, the change in capacitance of porous PDMS layer, expressed as $\Delta C_{porous} = \frac{\Delta\epsilon_r}{\Delta d}\epsilon_0 A$, would be greater than that of the non-porous PDMS layer. Due to the existence of both porous PDMS layer and non-porous PDMS layer, the porous PDMS TENG could be considered as two parallel-plate capacitors in stack, where the top capacitor consists

of PEDOT:PSS electrode/porous PDMS layer/non-porous PDMS surface and the bottom capacitor consists of non-porous PDMS surface/non-porous PDMS layer/metal electrode. In contrast, for the non-porous PDMS TENG, the capacitors are based only on non-porous PDMS layer. Assuming the negative charge density on non-porous PDMS surface saturates at a value of σ_N, those negative charges are being balanced by positive charges from both the top PEDOT:PSS electrode and the bottom metal electrode during the movements. The charge density on PEDOT:PSS electrode (σ_P) and metal electrode (σ_M) should satisfy the relation of $\sigma_P + \sigma_M = \sigma_N$. According to the report by He *et al.*,[77] σ_P is positively related to the capacitance (C_{top}) of top PDMS capacitor as $\sigma_P \propto C_{top}$. As discussed above, the top capacitor based on porous PDMS layer would undergo greater capacitance change ($\Delta C_{top-porous}$) compared to top non-porous PDMS capacitor of the non-porous PDMS TENG ($\Delta C_{top-non\,porous}$) when pressed and released at same loading force and frequency. This effect would lead to larger charge density change, represented by $\Delta \sigma_{P-porous} > \Delta \sigma_{P-non\,porous}$. When the top PEDOT:PSS electrode and bottom metal electrode are connected through an external load resistor, the output voltage and current generated can be expressed by the two equations below:

$$I(t) = -\frac{d\sigma_P}{dt}A \tag{2.1}$$

$$V(t) = -\frac{d\sigma_P}{dt}A \times R_L \tag{2.2}$$

where σ_P represents the charge density on the PEDOT:PSS electrode, A is the electrode surface area and R_L is the electrical resistance of the load resistor.

2.6 Electro-mechanical Performance of Soft TENG

The structural difference between the porous PDMS and non-porous PDMS TENG are illustrated in Figure 2.5a. To test and compare the performance of the porous PDMS and non-porous PDMS TENG, the electromechanical properties of both devices were measured. The loading force was exerted by a rubber piston with a contact area of 6×6 mm^2 mounted on a horizontal-moving stepping motor that is carefully aligned with the PEDOT:PSS electrode of the nanogenerator. The nanogenerator devices were mounted on a stationary stage and a commercial force sensor (A502, Tekscan, Inc) placed behind the nanogenerator was used to precisely measure the magnitude and frequency of the applied force. Output voltage and current were both measured by a Keithley 2450 Source Meter. After the measurement, a low-pass filter was applied to the output voltage and current data in MATLAB to filter out the noise. From the data presented in Figure 2.5b and c, one can see that when pressed under the same amount of loading force (100 N) and frequency (0.8 Hz), due to the larger change in charge density ($\Delta\sigma_P$) with the porous PDMS layer, the porous PDMS TENG exhibits larger average peak output voltage and output current at 1.65 V and 0.54 nA compared to non-porous PDMS TENG with 0.66 V and 0.34 nA. Furthermore, the improvement in output voltage and current might also be attributed to the increase in frictional area due to the larger surface-area-to-volume ratio offered by the porous PDMS structure, which could lead to larger charge density change as well.[75] From this point of view, the size of the pole could also play a role in enhancing the output performance of porous PDMS TENG. Although in this study only porous PDMS layer with pore size of 6 μm were fabricated, prior research by Lee *et al.*[75] has shown that the decrease of pore size would increase the output voltage and current due to the increased surface area-to-volume ratio. The effect of loading force and loading frequency on the output of the TENG device has also been studied. Figure 2.6a and b present the output voltage and current of the porous PDMS TENG under various
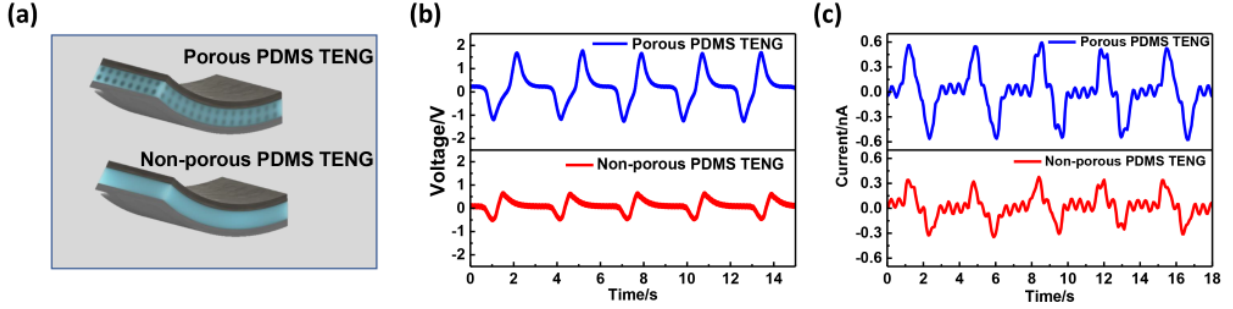
Figure 2.5: (a) Schematic illustrations of porous PDMS TENG (top) and non-porous PDMS TENG (bottom). (b) output voltage and (c) output current of porous PDMS and non-porous PDMS TENG at loading force and frequency of 100 N, 0.8 Hz

loading force from 50 to 150 N. Lee *et al.* has previously reported that increasing the loading force would lead to an increase in output voltage.[75] This is because greater loading force could result in larger deformation in the PDMS layer, which would lead to larger capacitance change and thus higher output voltage. However, according to the results in Figure 2.6a and b, both the output voltage and current exhibit negligible amount of change under loading forces of 50 N, 100 N and 150 N, suggesting that the porous PDMS is likely already fully compressed when the applied force exceeds 50 N and the output voltage and current have both reached their saturation values. Similar to the phenomena observed from piezoelectric and ferroelectret based nanogenerators,[66, 79] the output voltage and current also increase with increasing loading frequency as shown in Figure 2.6c and d. This could be explained through equations Eqs.(2.1) and (2.2), from which one can see that higher loading frequency at given magnitude of force would result in an increased value of $d\sigma_P/dt$, thus resulting in larger output voltage and current.
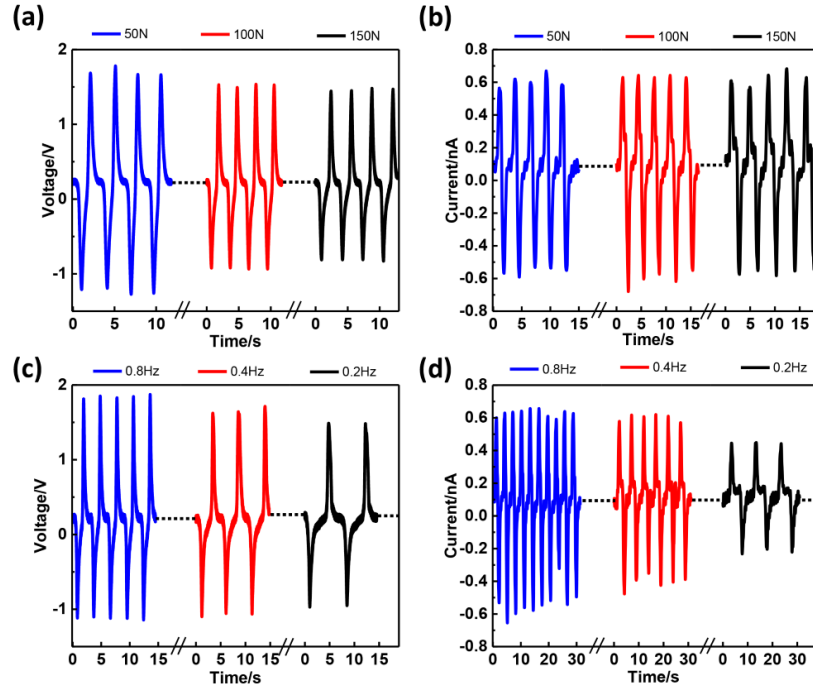
Figure 2.6: Loading force and frequency response of porous PDMS TENG. (a) output voltage (b) output current response under different loading forces at same loading frequency of 0.8 Hz. (c) output voltage (d) output current response under different loading frequencies at same loading force of 100 N.

2.7 Summary

In summary, first we have studied the polypropylene-based FENG for its potential as self-powered flexible multifunctional sensing device such as tactile and acoustic sensor. Next, we have demonstrated a porous PDMS film-based TENG device using intrinsically stretchable materials and a solution-based fabrication process. The formation of highly ordered, homogeneous porous PDMS structure has been confirmed by SEM and EDX and we have shown that the use of such porous PDMS could lead to TENG device with improved energy output (2.5 times improvement in output voltage and 1.6 times in output current) that outperforms similar device with non-porous PDMS. Its output responses to different loading force and loading frequency have also been studied to characterize the device and to explore

its performance limitations for further improvements. The porous PDMS film processing method and the use of intrinsically stretchable electrode materials applied in this research might pave the way for the development of low-cost and large-area stretchable TENG for wearable electronics as self-powered tactile sensor and self-sustained power source.

Chapter 3

Flexible Carbon Nanotube Thin-Film Transistors

3.1 Microfabrication of Carbon Nanotube Thin-Film Transistors

Microfabrication refers to conventional device manufacturing processes adapted from the semiconductor industry, such as multi-staged photolithographic patterning, vacuum-based deposition and physical/chemical etching processes. Although suffer from several drawbacks such as high cost, low throughput and limited scalability, the micro-fabricated devices prevail in device performances, reliability and compatibility with the existing CMOS technologies. In such a case, in this chapter, we first study the microfabrication of flexible carbon nanotube TFTs on polymer substrate.

3.1.1 Device Fabrication

Key steps in micro-fabricating the carbon nanotube TFTs on a polyimide (PI) substrate are illustated in Figure 3.1.[60]
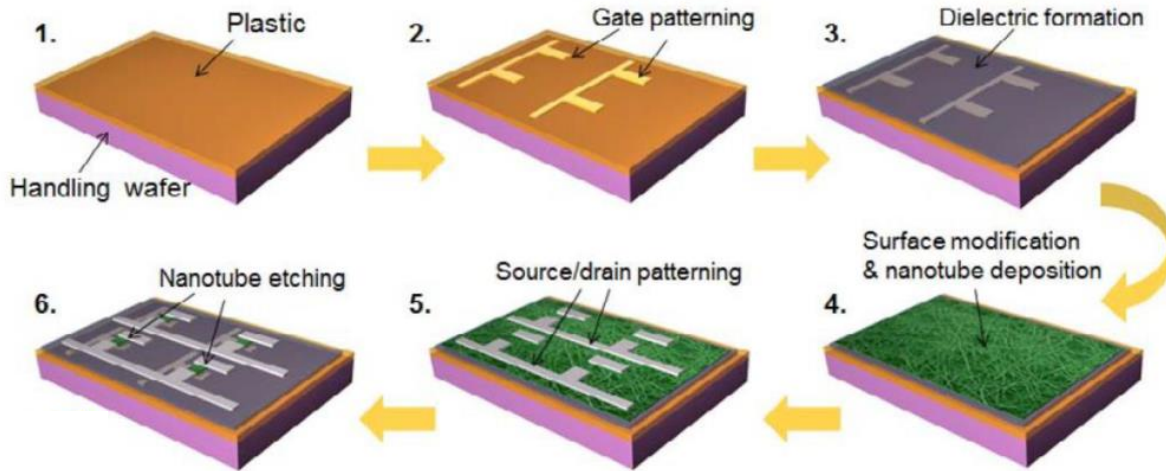
Figure 3.1: Schematic illustration of microfabrication process of flexible carbon nanotube thin-film transistors on polymer substrate. Reprinted from Ref.[60].

Polyimide from HD Microsystems is spin-coated (1000 rpm, 30 s; 2000 rpm, 1 min) onto a Si/SiO$_2$ wafer and baked on a hot plate at 300 °C for 10 min to form a uniform PI thin film with a thickness of around 10 μm. On top of the PI substrate, a Ti/Au (5/30 nm) bottom-gate electrode is formed by photolithography and lift-off, followed by dielectric layer deposition of Al$_2$O$_3$/SiO$_x$ (20/15 nm) using atomic layer deposition and e-beam evaporation. Before the CNT channel material deposition, poly-L-lysine solution (0.1% w/v; Sigma-Aldrich) is used to functionalize the dielectric layer surface to improve the adhesion of the CNT and thus increase the CNT network uniformity. After functionalization, the sample is rinsed with DI water and immersed into the as-purchased sSWCNT solution (0.01 mg/mL, NanoIntegris

Inc.) for 15 min to deposit active channel material. The sample is then taken out and rinsed with DI water and isopropyl alcohol, blow-dried by N_2, and annealed in a vacuum oven at 200 °C for 1 h to evaporate the residues. After that, Ti/Pd (0.5/35 nm) source and drain electrodes are formed by photolithography and e-beam evaporation, and as a final step, the transistor is finalized by etching away the sSWCNT outside the source-drain-defined channel region using oxygen plasma. After the fabrication is completed, the PI substrate can be delaminated from the handling wafer to render full flexibility of the device.

3.1.2   Electrical Characterization

The transfer characteristics (family of $-V_{GS}$ curves) and output characteristics (family of I_{DS}-V_{DS} curves) of the transistor are shown in Figure 3.2a and b, respectively.
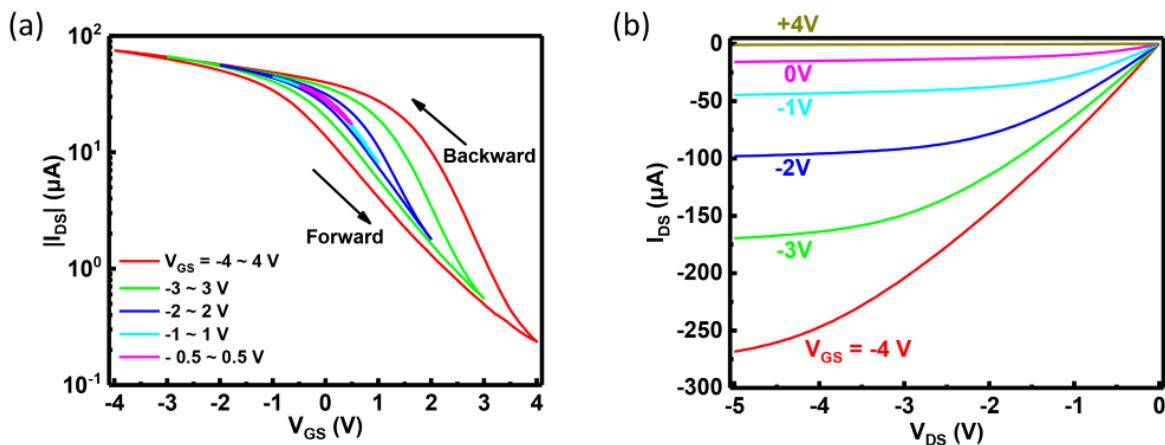
Figure 3.2: (a) Double sweep transfer characteristics of sSWCNT thin-film transistor. V_{DS}=-1 V. (b) Output characteristics of sSWCNT thin-film transistor.

The output curves exhibit good saturation at different V_{GS} values from +4 to -4 V. From the transfer curve measured with $V_{DS} = $ -1 V and V_{GS} sweeps from -4 to +4 V shown in Figure

3.2a, the device current on/off ratio (I_{on}/I_{off}) is 320 and the field-effect mobility is calculated to be 22.0 cm^2·V^{-1}·s^{-1} using the equation $\mu = (L \cdot g_m)/(W \cdot C_G \cdot V_{DS})$, where V_{DS} = -1 V, g_m is the peak transconductance and C_G is the unit-area gate capacitance from our previous work.[33] The high mobility of the sSWCNT thin-film transistors (TFTs) will be beneficial for applications such as active matrix of E-skin backplane to improve the operation speed. Furthermore, due to the large on/off ratio and the programmable hysteresis, such a device can be exploited for neuromorphic applications as biomimetic transistor with functions of a synapse. The details will be described in Chapter 4.

3.2 Introduction of Work on Printed Dual-Gate Transistors

Although the mainstream semiconductor industry has been pursuing high performance highly integrated electronic systems following the Moore's Law for decades, there are more and more emerging applications that demand large-scale and low-cost electronics with moderate performance and integration density.[8, 37, 60, 80] This leads to the rapid growth in printed electronics technology development. Remarkable progress has been made and a broad range of applications have been demonstrated recently.[23, 24, 27, 28, 81, 82, 83, 84] Compared to the conventional Si-based metal oxide semiconductor field-effect transistor (MOSFET), thin-film transistor (TFT) made directly by printing has its unique advantages in terms of processing temperature, sample size and cost.[85] The low processing temperature makes it possible to fabricate TFTs on a variety of plastic or elastic substrates and at large scale, which was previously hard to achieve for Si-based technologies due to the substrate rigidity and limited wafer size. The printing process also results in greatly reduced cost and it is

being widely adopted for flexible electronics fabrication with applications in areas such as display, sensing, wearable electronics, biomedical devices and soft robotics.

Various kinds of semiconducting materials including 2-dimensional semiconductors,[23, 24] organic semiconductors,[25, 26] metal oxides,[86, 87] and carbon nanotube[27, 28, 29] have been studied for printed TFTs. Among them, the carbon nanotube is found to be attractive due to the superior carrier mobility[30, 31, 32] and long-term stability, and the use of sorted high-purity semiconducting single-wall carbon nanotubes (sSWCNTs) has been demonstrated to significantly enhance the performance of printed TFTs.[33, 34] On the other hand, the sSWCNT TFTs generally exhibit only p-type characteristics in air, which is a formidable obstacle to form complementary metal-oxide semiconductor (CMOS) logic circuits that would require both p-type and n-type transistors. Although n-type printed TFTs using metal oxides such as zinc tin oxide[88] or indium zinc oxide[29] have been utilized to implement CMOS logic circuits with p-type printed sSWCNT TFTs, it is still appealing to use sSWCNT alone as the channel material for CMOS circuits as it will result in better device matching and can also utilize the full potential of the carbon nanotube material. Several kinds of n-type sSWCNT transistors have been reported by applying methods such as using low work function metal,[89, 90] organic reducing reagents,[91] or passivation with high-k dielectric film.[92] Similar advancement has been extended to printed transistors with electron donating agent[84] but it remains very challenging to precisely control the doping effect especially during a printing process. Another more flexible and effective solution is the use of dual-gate transistor structure, which offers fine-tuning of the transistor threshold voltage and polarity.[93, 94] With the second gate as a control gate, the charge distribution and electrical field in the channel region can be adjusted, allowing the device to be tuned to either predominantly p-type or n-type.[95] Devices with dual-gate structure based on various types of materials such as organic semiconductors,[96] semiconducting oxides,[97] carbon nanotube,[93, 95] graphene,[98]

45

and PbS quantum dots[99] have all been reported. It is worth noting that the devices above are all made by conventional cleanroom-based microfabrication processes. In this chapter, we report dual-gate carbon nanotube TFTs that are fabricated entirely using inkjet-printing processes. In such a device, the printed sSWCNTs channel semiconductor is sandwiched in between two gate stacks, one on top and one underneath, both employing composite film of barium titanate $BaTiO_3$ (BTO) nanoparticles and poly (methyl methacrylate) (PMMA) as the gate dielectric layer. The encapsulation by the BTO/PMMA layer effectively converts the sSWCNT TFT from unipolar p-type into almost symmetric ambipolar, allowing precise adjustment of the threshold voltages and n-type conduction to be achieved by using the top gate as the control gate. By integrating two printed dual-gate ambipolar TFTs biased with different control gate voltages, a CMOS inverter circuit with close to rail-to-rail output voltage swing is demonstrated.

3.3 Device Structure and Fabrication

Figure 3.3a schematically illustrates the key steps involved in fabricating the fully-printed dual-gate carbon nanotube TFTs on a polyimide (PI) substrate.The polyimide (HD Microsystems) is spin-coated (1000 rpm for 30 s followed by 2000 rpm for 1 min) onto a Si/SiO_2 wafer and baked on a hot plate at 300 °C for 10 min to form a uniform PI thin film. In addition to the PI substrate, similar dual-gate TFTs are also printed directly on rigid Si/SiO_2 wafers (with 300 nm SiO_2) by utilizing the SiO_2 as the dielectric layer and heavily doped Si as the back gate. A GIX Microplotter (Sonoplot Inc.) is used for all printing processes. The nozzle is first lowered down to let the ink inside of the nozzle touch the sample surface and then pulled up to a small but safe height of tens of micrometers to allow the formation of a liquid meniscus between the printing nozzle and the substrate. This maintains the continuity of the ink from nozzle to the surface while avoiding any physical contact or scratch between
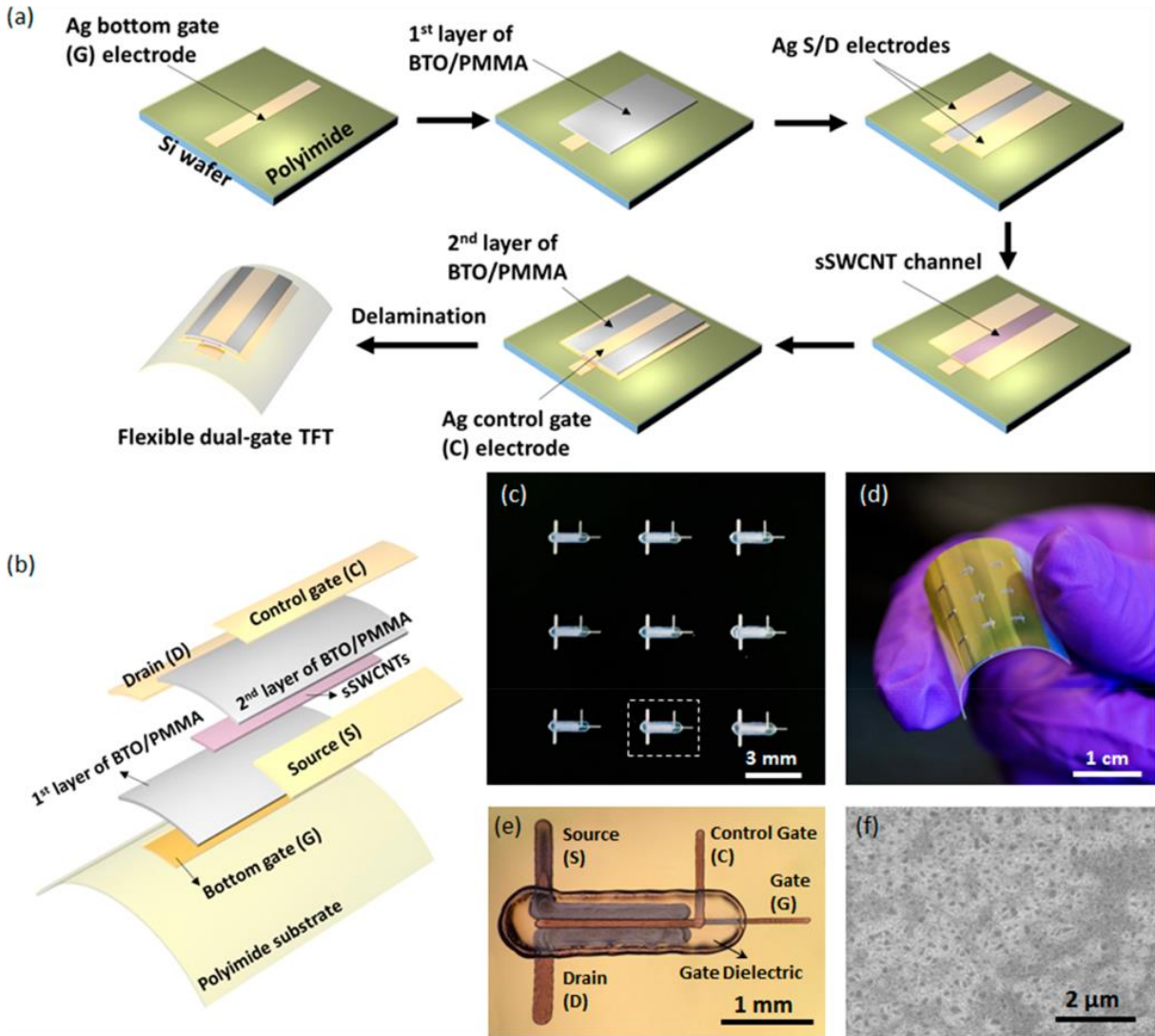
Figure 3.3: Fully-printed flexible dual-gate carbon nanotube thin-film transistors. (a) Schematic diagrams illustrating the fabrication process flow. (b) Schematic diagram showing the various layers in a printed dual-gate TFT. (c, d) Optical photographs showing a sample consisting of a 3×3 TFT array printed on a flexible polyimide substrate. (e) Optical micrograph of an individual TFT. (f) SEM image showing the printed sSWCNT film in the channel region of the TFT.

the nozzle and the sample. The bottom gate electrode is first printed on the substrate using silver nanoparticle ink (PG-007AA from Paru Corp., South Korea) followed by baking at 150 °C for 15 min on a hot plate to evaporate the solvent and sinter the silver nanoparticles. The first layer of gate dielectric is then printed using a hybrid dielectric ink composed of $BaTiO_3$ nanoparticles and PMMA (PD-100 from Paru Corp., South Korea) at a temperature of around 60-65 °C. After printing, the sample is baked at 150 °C for 10 min to further evaporate the ink solvent and solidify the BTO/PMMA dielectric layer. Source and drain electrodes are printed next, following the same printing and baking recipes of the bottom gate electrode. High purity (>99%) sSWCNT solution (IsoNanotubes-S from NanoIntegris) is printed in the channel region of the TFT followed by baking at 150 °C for 10 min, and the uniformity of the printed sSWCNT network is examined by SEM. After the printing of the carbon nanotube channel material, a second layer of BTO/PMMA dielectric and the top gate electrode are printed sequentially using the same methods as the first dielectric layer and the bottom electrode. Once the fabrication is completed, the PI substrate is delaminated from the handling wafer and placed on a polyethylene terephthalate (PET) supporting substrate for characterization and bending tests. Additionally, as a reference sample for performance benchmarking, we have also fabricated similar printed dual-gate TFTs on rigid SiO_2/Si substrates. The fabrication process of such dual-gate TFTs on silicon substrate is almost identical to the fabrication of the flexible dual-gate TFTs on PI substrate, except that the bottom gate electrode and the bottom gate dielectric layer are skipped as the heavily-doped silicon substrate is employed as the bottom gate instead. A more detailed view of the various layers comprising the printed flexible dual-gate TFT is shown in Figure 3.3b. In such a dual-gate TFT, the bottom gate electrode serves the role of the regular gate electrode in a conventional field-effect transistor while the top gate electrode works as a control gate to tune the TFT characteristics to either predominantly p-type or predominantly n-type. Figure 3.3c and d shows an array of 3×3 TFTs printed on a single piece of PI substrate. Because of

the printing process used, the fabrication can be easily scaled up to much larger sample size at relatively low cost. Figure 3.3e shows the optical micrograph of a representative dual-gate TFT on PI substrate. The typical channel length (L) and channel width (W) of the TFTs used in this study are in the range of 50~150 μm and 1000~2000 μm, respectively. Scanning electron microscopy (SEM) image of the printed sSWCNT film in the channel region of the TFT is shown in Figure 3.3f, indicating dense and uniform distribution of carbon nanotubes

3.4   Electrical Characterization of Single and Dual-Gate Transistors

The effect of adding the top gate stack on the electrical characteristics of the printed TFTs is systematically studied in Figure 3.4. Before printing the top BTO/PMMA gate dielectric layer, the sSWCNTs in the channel were exposed under ambient conditions, and unipolar p-type transfer characteristics ($I_{DS} - V_{GS}$ curves) were observed from both devices fabricated on silicon (Figure 3.4a) and PI substrate (Figure 3.4b). Even after moderate baking or slight toluene rinsing of the sSWCNT channel, no noticeable change was observed from the transfer curves of both types of samples. Interestingly, after another layer of BTO/PMMA dielectric was printed on top of the sSWCNT channel, the $I_{DS} - V_{GS}$ curves of the same devices underwent drastic changes from unipolar p-type to almost symmetric ambipolar type as shown in Figure 3.4c and d. Similar phenomenon was also observed previously from microfabricated carbon nanotube transistors and graphene transistors when fully encapsulated by dielectric layers. [92, 100] Here for the printed TFT with ambipolar characteristics, we define its threshold voltage (V_{th}) as the gate voltage under which the drain current is at its minimum. As the V_{DS} increases from -2 to -10 V, the V_{th} only varies slightly from 2.7 to 3.2 V for TFTs on SiO$_2$/Si and from 8.0 to 5.4 V for TFTs on PI. The V_{th} variations

of both types of printed devices are almost negligible compared to the sweeping range of V_{GS} (80 V), indicating little dependence of V_{th} on the drain voltage. The fact that the addition of a top BTO/PMMA layer can significantly alter the polarity of the printed carbon nanotube TFTs can be explained as the removal of oxygen, moisture, and other impurities from the sSWCNT film during BTO/PMMA printing process. It is also worth noting that the transfer curves are almost symmetrical with very slight predominance in the p-branch, which indicates comparable hole and electron conductivities in the printed TFTs. For the p-branch characteristics (V_{GS} = -40 V) that correspond to the hole conduction, when measured under a V_{DS} of -10 V, the width-normalized on-current (I_{on}/W) is 9.8 μA/mm and 10.7 μA/mm for devices printed on PI and SiO_2/Si, respectively, and the current on/off ratio (I_{on}/I_{off}) is 1.23×10^2 and 8.8×10^2 for devices on PI and SiO_2/Si, respectively. Similarly, for the n-branch (V_{GS} = 40 V) that corresponds to the electron conduction, the I_{on}/W and I_{on}/I_{off} are 3.8 μA/mm and 47 for devices printed on PI and 3.3 μA/mm and 2.67×10^2 for devices printed on SiO_2/Si. The electron and hole field-effect mobilities of the printed dual-gate TFTs are further extracted using the equation $\mu = (L \cdot g_m)/(W \cdot C_G \cdot V_{DS})$, where g_m is the peak transconductance measured at V_{DS} = -10 V and C_G is the unit-area gate capacitance. For better accuracy, the C_G value of the TFT on PI substrate was obtained directly from the capacitance-voltage curves (Figure 3.4g) measured at a low frequency of 1 kHz following the method previously reported in our earlier work.[27] For the flexible device on PI substrate (Figure 3.4d), the hole mobility is calculated to be 0.51 $cm^2 \cdot V^{-1} \cdot s^{-1}$ with a peak g_m of 5.6×10^{-7} S and the electron mobility is calculated to be 0.24 $cm^2 \cdot V^{-1} \cdot s^{-1}$ with a peak g_m of 2.2×10^{-7} S. As a comparison, for similar devices printed on rigid SiO_2/Si substrate, the hole mobility is calculated to be 0.44 $cm^2 \cdot V^{-1} \cdot s^{-1}$ with a peak g_m of 1.02×10^{-6} S and the electron mobility is calculated to be 0.13 $cm^2 \cdot V^{-1} \cdot s^{-1}$ with a peak g_m of 3.0×10^{-7} S. While we did not attempt to further optimizing the printing process for the dual-gate TFTs in this work, it is still worth noting that the printed flexible TFTs exhibit more or less comparable performance
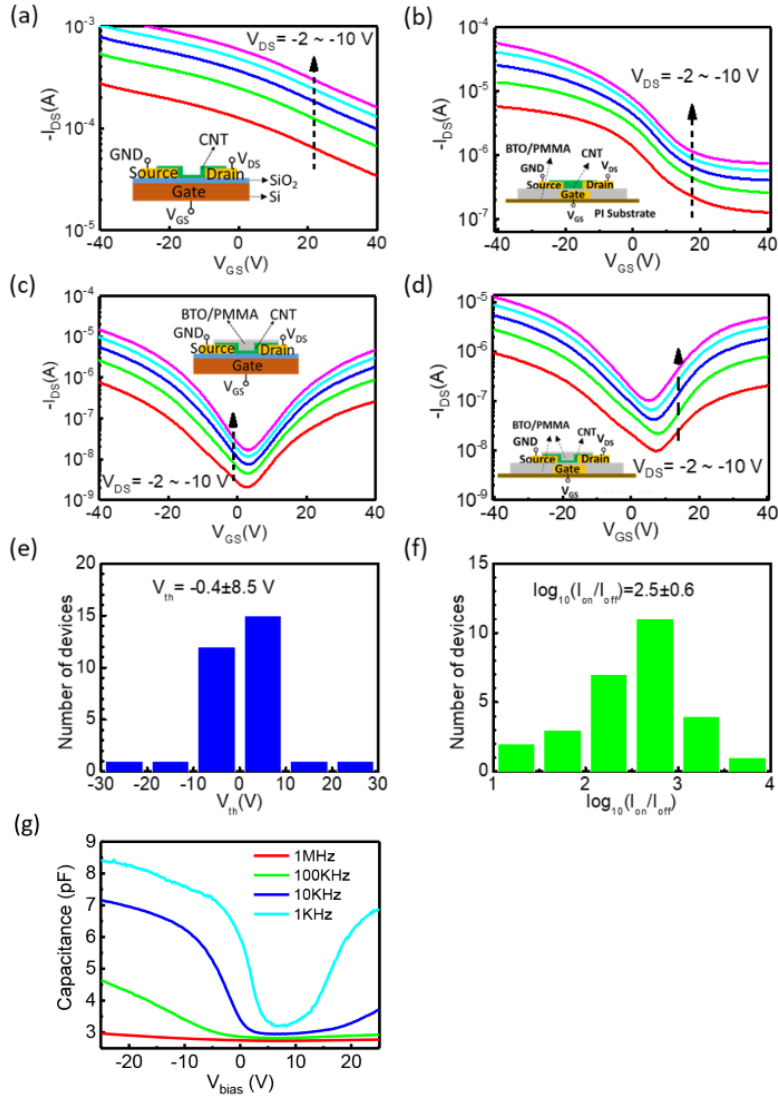
Figure 3.4: Conversion of the TFT transfer characteristics from p-type to ambipolar with the addition of a top dielectric layer. (a, b) Representative p-type transfer curves measured from the TFTs printed on Si/SiO_2 substrate (a) and PI substrate (b) with the sSWCNTs in the channel directly exposed to ambient conditions. (c, d) Representative ambipolar transfer curves measured from the devices on Si/SiO_2 (c) and PI (d) after another layer of BTO/PMMA gate dielectric was printed on top to fully encapsulate the sSWCNT channel. The schematics of the TFT configurations tested in panels (a-d) are shown as the inset. (e, f) Histograms showing the V_{th} (e) and on/off current ratio (f) distributions of the ambipolar TFTs with BTO/PMMA coverage. (g) C-V characteristics of the fully-printed TFT on polyimide substrate with BTO/PMMA dielectric layer for both top control gate and bottom gate.

to their rigid counterparts. We have also fabricated a large number of such printed dual-gate TFTs in order to study the device-to-device uniformity. As shown in the histograms of Figure 3.4e, the threshold voltage V_{th} has a relatively narrow distribution between -10 V and 10 V with an average value of -0.4 V. From Figure 3.4f, the average current on/off ratio is 3.2×10^2 and the highest on/off ratio achieved is 4.1×10^3. Both figures indicate rather uniform device performance from multiple batches of printed dual-gate TFTs.

3.5 Hysteresis and Long-term Stability

We have also studied the hysteresis and long-term stability of the ambipolar characteristics in the printed dual-gate TFTs. The double sweep (forward and backward sweeps) transfer curves were measured on both the devices on SiO_2/Si (Figure 3.5a) and PI (Figure 3.5b). Hysteresis is generally defined as the difference in V_{GS} voltage at an average I_{DS}, $i.e.$ for the forward and backward sweeping curves. Based on this definition, the hysteresis is 3 V for devices on PI and 1.6 V for devices on SiO_2/Si at a V_{DS} of -10 V. The small hysteresis can be attributed to the top BTO/PMMA layer, which effectively passivates the sSWCNT channel from common absorbents under ambient conditions such as moisture. Furthermore, with the protection by the top BTO/PMMA layer, the ambipolar characteristics also exhibit good long-term stability and remain almost unchanged even after being stored for 4 months (Figure 3.5c).
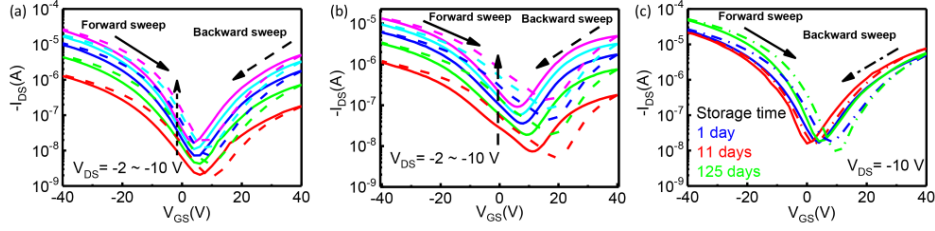
Figure 3.5: Hysteresis and long-term stability of the printed ambipolar TFTs. (a-b) The forward and backward sweep transfer curves measured at various V_{DS} biases showing very small hysteresis for devices on both SiO_2/Si (a) and PI (b) substrates. (c) The transfer curves measured from the same TFT after being stored in ambient condition for up to 4 months.

3.6 Tunable Ambipolar Transfer Characteristics

The tuning of the ambipolar characteristics of the dual-gate TFTs can be achieved by changing the voltage applied on the top gate (the control gate), which controls the charge carriers in the channel and adjusts the threshold voltage. As shown in Figure 3.6a,b, the I_{DS}-V_{GS} curves can be tuned effectively from predominantly p-type to predominantly n-type by simply varying the control gate voltage V_{CS}. As V_{CS} gradually increases from -60 to +60 V, the V_{th} decreases from +15.5 V to -2.5 V for TFTs on silicon (Figure 3.6a) and from +24.5 V to -2.5 V for the flexible devices on PI (Figure 3.6b). The increase in V_{CS} voltage also leads to enhanced n-branch conduction and suppressed p-branch conduction. More specifically, as the V_{CS} changes from -60 to +60 V, the p-branch current ($V_{GS} = -40$ V) decreases from 59 to 5.8 μA for devices on PI and from 79 to 7.7 μA for devices on silicon, while the n-branch current ($V_{GS} = 40$ V) increases from 1.75 to 9.9 μA for devices on PI and from 1.7 to 11 μA for devices on silicon. Both p-branch and n-branch output characteristics (I_{DS}-V_{DS}) are measured and presented in Figure 3.6c-f where nice saturation in the drain current can be observed. It should be noted that the I_{DS}-V_{DS} curves are slightly nonlinear at low V_{DS} biases, indicating the presence of a small Schottky barrier between the printed silver source/drain electrodes and the semiconducting carbon nanotubes. This was not observed in our previous work
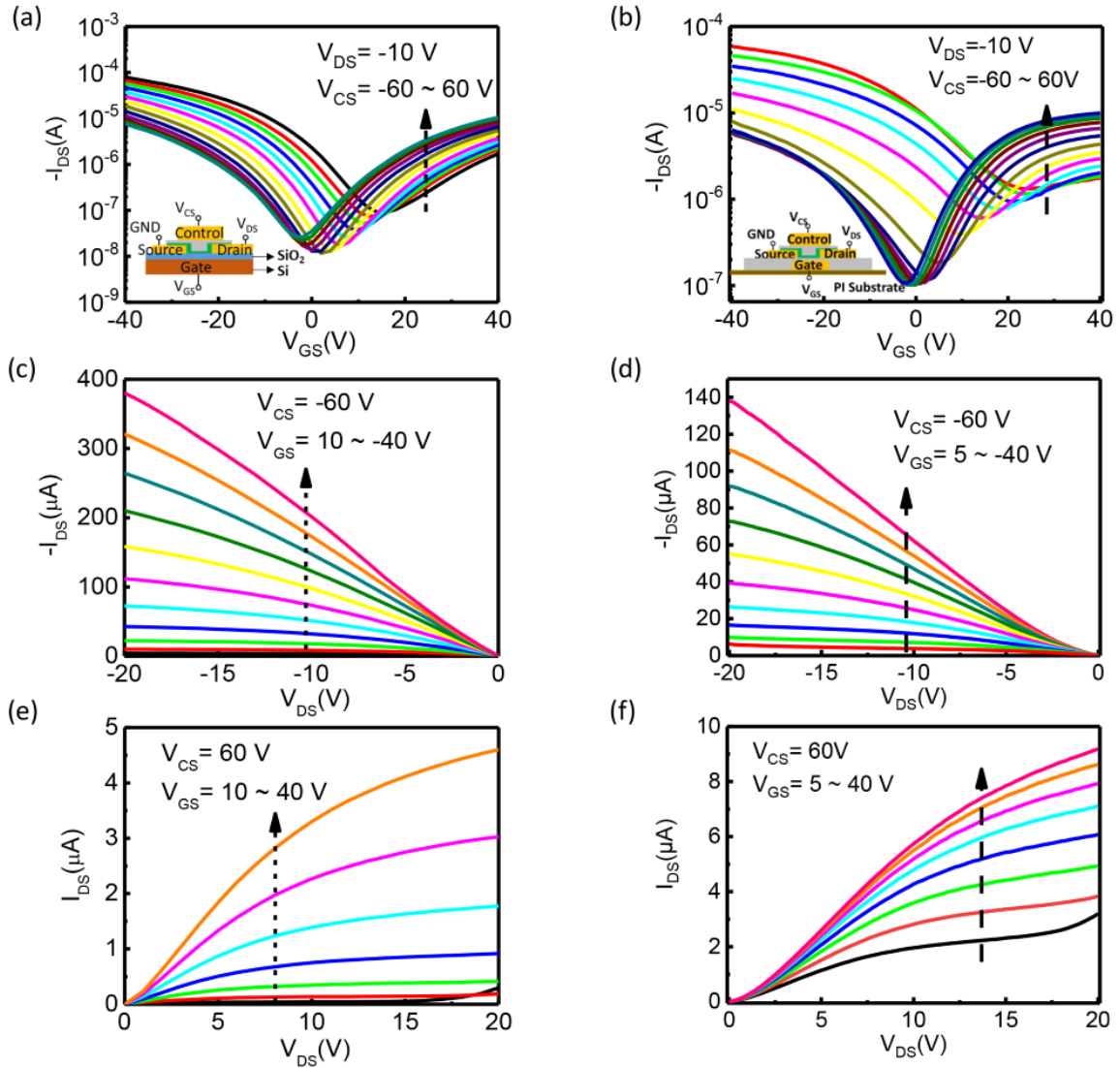
Figure 3.6: Fully-printed dual-gate TFTs with tunable ambipolar transfer characteristics. (a, b) The transfer curves of the printed dual-gate TFTs measured under different control gate voltages V_{CS} for devices on SiO_2/Si (a) and PI (b) substrates. (c, d) p-branch output characteristics achieved from the dual-gate TFTs on SiO_2/Si (c) and PI (d) substrates by applying a constant control gate voltage of -60 V. (e, f) n-branch output characteristics achieved from the dual-gate TFTs on SiO_2/Si (e) and PI (f) substrates by applying a constant control gate voltage of 60 V.

on printed carbon nanotube transistors,[27] in which Ohmic contacts with linear I_{DS}-V_{DS} curves were observed at low V_{DS} biases. We suspect that the Schottky contact might be caused by the different printing sequences used compared to our previous work, with the sSWCNTs printed on top of the silver source/drain electrodes in this work, but fully covered underneath the printed silver source/drain electrodes previously. Without encapsulation by the silver electrodes, the Ag-sSWCNT contact might be prone to contaminants in air during the printing and baking processes, which contributes to the Schottky barrier observed in this work. It is also important to point out that for proper operation of the dual-gate TFT, the control gate voltage (V_{CS}) and the bottom gate voltage (V_{GS}) should be compatible with each other; *i.e.*, they should be either both positive or both negative. If one is set to positive and the other is set to negative, the two gates will attempt to bias the TFT into opposite polarities, and thus, there will always be a conductive channel between the source and drain electrodes. Because channel pinch-off can never happen in such a scenario, the TFT can never enter the saturation region, resulting in superlinear increase in the output characteristics at high V_{DS}. Such bias conditions cause the transistor to not work properly and should therefore be avoided.

3.7   Flexibility and Durability

The flexibility and durability of the printed dual-gate TFTs on the PI substrate are examined, and the results are presented in Figure 3.7. Because of the very thin ($\sim$10 μm) PI substrate used, the devices are expected to be rather bendable. The transfer curves of the device exhibit almost negligible differences when bent down to a curvature radius of 5 mm (Figure 3.7a) The same device also exhibits very minor variations during the cyclic bending tests and manages to maintain its performances after up to 1000 cycles of bending to a curvature

radius of 5 mm (Figure 3.7b), manifesting excellent mechanical robustness of the dual-gate TFTs.
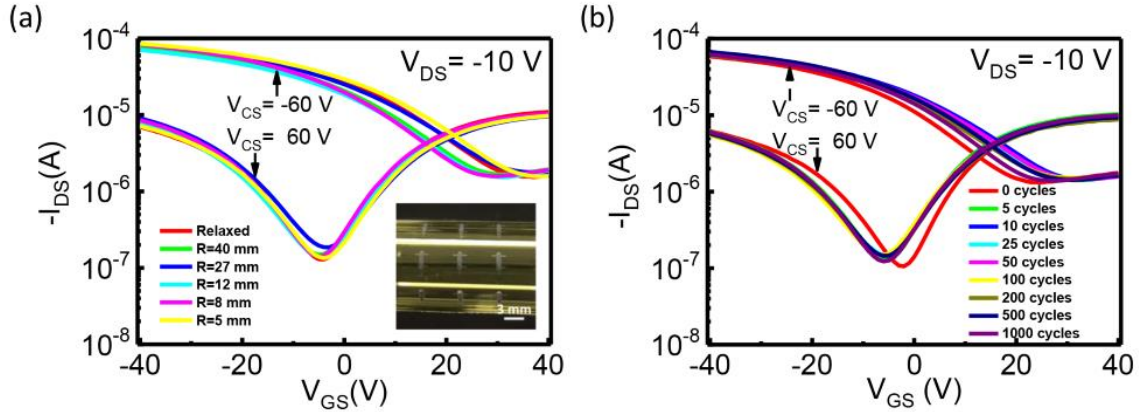
Figure 3.7: Bending tests conducted on fully-printed flexible dual-gate TFTs. (a) Transfer curves of a dual-gate TFT measured with V_{CS} of -60 and 60 V at various curvature radii. Inset: photograph of the sample when bent. (b) Transfer curves of a dual-gate TFT measured with V_{CS} of -60 and 60 V after various bending cycles down to a curvature radius of 5 mm.

3.8   Printed Dual-Gate TFTs for CMOS Logic Circuit

By integrating two printed dual-gate TFTs with comparable ambipolar characteristics, a complementary logic inverter can be realized as illustrated in Figure 3.8a.

Previously reported work on printed logic circuits with carbon nanotube TFTs almost always relied on PMOS-only logic with a resistive load for the pull-down circuit. This is because carbon nanotube TFTs normally only exhibit unipolar p-type characteristics as discussed above. Here, we have managed to achieve a complementary logic inverter by selectively tuning one transistor into a p-type TFT and the other into an n-type TFT by applying different
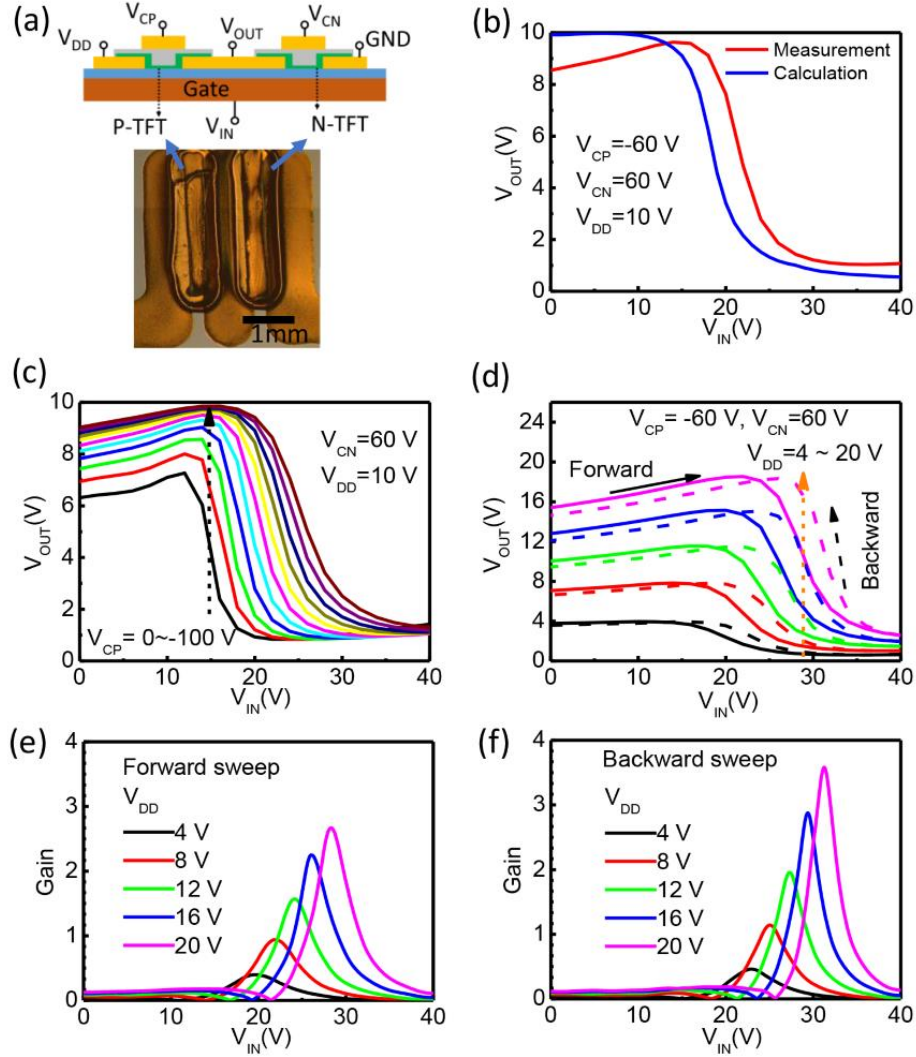
Figure 3.8: CMOS inverter formed by integrating two printed dual-gate TFTs. (a) Schematic diagram and optical micrograph of a printed CMOS inverter, where V_{CP} and V_{CN} denote the control gate voltages for p-TFT and n-TFT, respectively. (b) Measured and calculated inverter voltage transfer characteristics (VTC) with the p-TFT biased with a control gate voltage of -60 V and n-TFT biased with a control gate voltage of 60 V. The supply voltage V_{DD} is 10 V. (c) The inverter VTC measured at different V_{CP}. (d) The forward and backward sweeping inverter VTC measured with different V_{DD}. (e, f) Voltage gain of the printed CMOS inverter for forward (e) and backward (f) sweep of V_{IN}.

57

control gate voltages (V_{CP} = -60 V for the p-TFT and V_{CN} = 60 V for the n-TFT). The measured (red trace) as well as the calculated (blue trace) voltage transfer characteristics (VTC) of the inverter are plotted in Figure 3.8b. The calculated VTC is obtained by using the transfer curves of both TFTs in the inverter and treating them as a resistive divider, and it shows good agreement with the measured data. With a V_{DD} of 10 V, the measured VTC exhibit a peak output voltage of 9.7 V and a minimum output voltage of 1.1 V, which is decently close to rail-to-rail operation. If one needs to further improve the output voltage swing, TFTs with a larger on/off ratio will be needed. The VTCs can also be fine-tuned by the changing the control gate voltage as is shown in Figure 3.8c. As the V_{CP} is being tuned from 0 to -100 V, the corresponding TFT becomes more and more predominantly p-type, which leads to enhanced p-branch current and stronger pull-up performance. As a result, the VTC moves closer and closer toward V_{DD} with the peak output voltage increasing from 7.3 to 9.9 V, approaching the ideal peak output voltage of V_{DD} = 10 V. The VTCs and voltage gain (-dV_{OUT}/dV_{IN}) measured with various supply voltages from 4 to 20 V are presented in Figure 3.8d-f. As the V_{DD} increases, both the peak output voltage (*e.g.*, 3.95 V for V_{DD} = 4 and 18.5 V for V_{DD} = 20 V) and the voltage gain increases monotonically, which is similar to other published results.[29] The peak voltage gain is 3.6 and 2.7 for backward and forward sweeps, respectively. Although the voltage gain of the complementary inverter is still limited, further improvements are possible by optimizing the printing technology to achieve a thinner gate dielectric layer.

3.9   Summary of Work on Printed Dual-Gate Transistors

In summary, we have demonstrated fully printed dual-gate carbon nanotube TFTs on both PI and SiO_2/Si substrates. The flexible devices on PI substrates exhibit comparable performance to their rigid counterparts in terms of their transfer characteristics, output characteristics,

hysteresis, transconductance, carrier mobility, and on/off ratio. We have also shown that the ambipolar characteristics of the dual-gate TFT can be fine-tuned by adjusting the control gate voltages, and predominant n-type behavior (enhanced n-branch current and suppressed p-branch current) or p-type behavior can be achieved by using positive or negative V_{CS} biases, respectively. Based on the dual-gate control, a complementary inverter is demonstrated by employing two dual-gate TFTs biased with different control gate voltages. This work addresses the challenge of constructing CMOS-analogous logic circuits using fully printed carbon nanotube transistors. It will be beneficial for the development of large area, scalable, and lowcost printed flexible electronic systems in the future.

Chapter 4

Flexible Carbon Nanotube Synaptic Transistor for Neurological Electronic Skin Applications

4.1 Introduction

As the largest organ of the human body and the foundation of human physical interaction with the world, skin, with its complex tactile and thermal sensory capabilities, has intrigued and inspired enormous research efforts to mimic or even augment its functions. Artificial electronic skin (E-skin)[1, 14, 35, 101], which was initially implemented primarily as a network of soft pressure sensors for spatial and temporal mapping of tactile information,[8, 15, 102] has recently been reinforced with a variety of additional sensing modalities and human-interactive functionalities, such as visualizable pressure detection,[60],in situ sweat analysis[17] and haptic skin interfaces for virtual reality/augmented reality applications.[103] Previous studies

of E-skin mainly utilize passive pressure-sensitive components such as resistive or capacitive pressure sensors to achieve physical-electrical signal transduction through their conductance or capacitance change.[8, 51, 104] In contrast, the signal transduction mechanism is more "active" in a biological skin system as sensory receptors embedded across the skin would directly transduce the physical contact into information-encoded, pulse-based electrical signals. On the other hand, neuronal functions (*i.e*, the conveyance and transmission of such signals to the central nervous system (CNS) such as the brain and spinal cord) have not been explored in E-skin systems as extensively.

Signal communication between a sensory afferent neuron and a neuron in the CNS is enabled through synapse. The strength of the synapse (synaptic weight) can be adjusted in response to the action potentials from sensory neurons, which is a crucial property that has been proven to be the foundation of mammal memory formation and learning ability.[105, 106] The modulation of synaptic weight can be emulated in electronic devices by modulating the channel conductance of two-terminal memristors or three-terminal artificial synaptic transistors.[107] As the action potential can be emulated by voltage pulse, the induced conductance change is usually presented in the form of a change in channel current, which is usually called postsynaptic current (PSC) in synaptic devices. Thanks to the recent development in flexible neuromorphic electronic materials and device technologies, it is now possible to achieve synaptic devices in flexible[108, 109] or even stretchable forms[52, 110] that can be compatible with soft and curved human skin or internal organs. Among the various neuromorphic electronic materials that have been studied, a one-dimensional (1D) semiconducting single-wall carbon nanotube (sSWCNT) offers an outstanding combination of mechanical robustness,[33, 45] large on/off ratio, and high carrier mobility.[31, 46] Owing to its 1D geometry and small physical size, the conductance of the sSWCNT is demonstrated to be highly sensitive to charged interface trap states,[50] allowing the sSWCNT-based

artificial synaptic transistors to exhibit a broad conductance modulation range.[42] Interest and intrigue toward the sSWCNT in neuromorphic devices have been further expanded due to its established outstanding scalability and mechanical flexibility.[62, 111, 112] Wafer-scale aligned sSWCNT synaptic transistor arrays demonstrate exceptional device uniformity and repeatabilty,[43] whereas flexible sSWCNT synaptic transistors with extraordinary bendability on various flexible substrates[49, 113] show a huge potential in wearable electronic applications.

In this study, we report a biomimetic electronic sensory skin by utilizing a flexible high-performance sSWCNT synaptic thin-film transistor to imitate the chemical synapse between a peripheral nerve and the CNS and thin-film ferroelectret nanogenerator (FENG) to imitate the mechanoreceptor and peripheral nerve itself for transducing and relaying the force stimulus information to the synapse. The illustration of the electronic system and the analogy to its biological counterpart is shown in Figure 4.1a. We have systematically studied the synaptic characteristics including short-term/memory plasticity (STP/MEP), spike-amplitude-dependent plasticity, spike-width-dependent plasticity, paired-pulse facilitation (PPF) and frequency filtering characteristics, analogue-synaptic weight switching behavior with bending and cyclic tests, spike-time-dependent plasticity in the flexible sSWCNT synaptic transistor. The output characteristics of FENG in response to external force stimuli have also been studied. In the reported artificial sensory skin, the FENG sensor converts the tactile information (the force amplitude and frequency) of the physical contact into presynaptic action potential pulses, which are then passed to the gate of the synaptic transistor to render changes in drain current (PSC), mimicking the modulation of synaptic weight in a biological synapse. Such an operation of the synaptic transistor and its ability to maintain the change in conductance states allow the device to process the electrical signals from the sensor and generate history-dependent output that reflects not only the amplitude but also the sequence and frequency of the force stimuli. Our artificial sensory skin allows instantaneous sensing of

force stimuli with biological synapselike transmission, processing and memory of the stimulus signals. With the artificial synaptic transistor potentially interfacing with a motor or actuator unit, the sensory skin could have the potential for controlling skeletal muscle fibers or have applications in neuroprosthetic devices.

4.2 Structure and Working Principle of sSWCNT Synaptic Transistor

Figure 4.1b shows a representative image of arrays of thin-film sSWCNT synaptic transistors fabricated on a flexible polyimide (PI) substrate being wrapped on a glass cylinder. The inset is an optical micrograph of an individual transistor with a channel length of $L = 10~\mu$m and a channel width of $W = 100~\mu$m. The transistor consists of Ti/Au back-gate electrode, Al_2O_3/SiO_x dielectric layer, a solution-processed sSWCNT active channel, and Ti/Pd source and drain electrodes. The microfabrication processes are described in Section 3.1.1, Chapter 3, in detail. The hysteresis characteristics (family of double sweep I_{DS}-V_{GS} curves) of the transistor are shown in Figure 4.1c. Although the ideal CNT does not have surface dangling bonds, interface trap states still exist between the CNT and the oxide dielectric layer in a CNT transistor.[114, 115] Figure 4.1d shows the energy band diagrams, illustrating the oxide/CNT interface states. When a negative gate bias is applied, the energy band of the CNT at the oxide/CNT interface and the interface states bend upward, while the Fermi level (E_F) of the CNT remains flat. In this scenario, more interface donor states become empty and positively charged, causing a negative shift of the corresponding I_{DS}-V_{GS} curve and the threshold voltage (V_{th}). Similarly, when a positive gate bias is applied, the CNT energy band and interface states bend downward, causing more acceptor interface states to be filled and thus negatively charged, which leads to a positive shift of the I_{DS}-V_{GS} curve
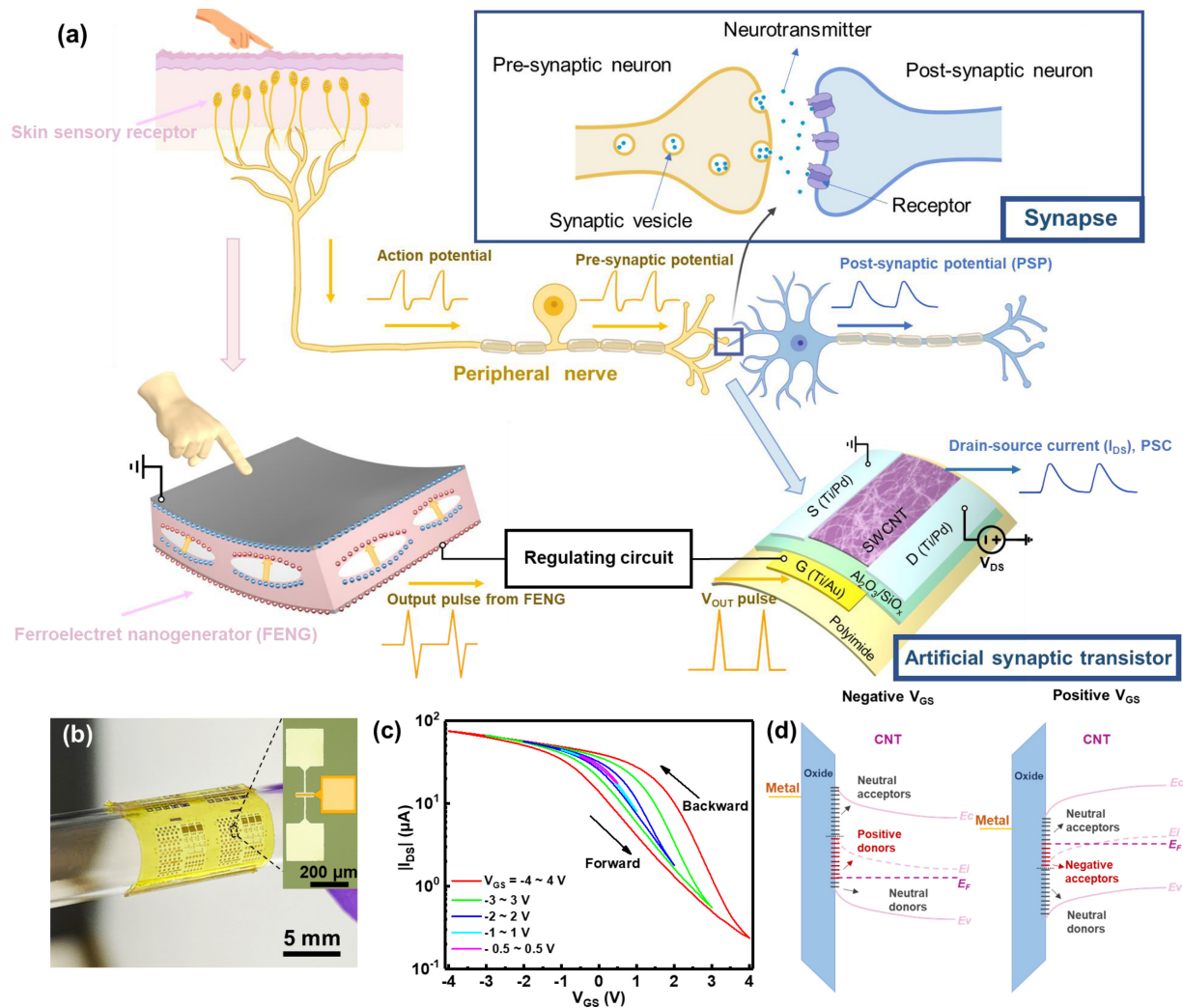
Figure 4.1: (a) Schematic illustration of biological skin, its peripheral nerve and synapse (upper part), in comparison with its artificial electrical counterpart (lower part). The schematic illustration is partially created with BioRender.com. (b) Optical photograph showing a sample of flexible carbon nanotube synaptic transistors. Inset: optical micrograph of an individual synaptic transistor. (c) Double sweep transfer curves of the synaptic transistor showing the hysteresis under different V_{GS} sweeping ranges measured with $|V_{DS}| = 1.0$ V. (d) Energy band diagrams illustrating the origin of hysteresis induced by interface trap states under positive and negative gate biases in sSWCNT synaptic transistor.

and V_{th}. A nonlinear, hysteretic behavior of V_{th} from bidirectional V_{GS} sweeps (V_{GS} sweeping from negative to positive values, and *vice versa*) is observed. It is worth noting that the width of the hysteresis curve is directly associated with the range of V_{GS} sweeping. The value of hysteresis is generally defined as the difference between V_{GS} at average I_{DS}, that is, $(I_{DS\text{-}MAX} + I_{DS\text{-}MIN})/2$ from backward and forward sweeping curves. As shown in Figure 4.1c, when V_{GS} is swept from -4 to +4 V, a hysteresis of 1.44 V is observed. In contrast, if the sweeping range of V_{GS} is reduced to -0.5 to +0.5 V, the I_{DS}-V_{GS} curve only exhibits negligible hysteresis. This phenomenon can be explained by the fact that greater V_{GS} biases result in more significant band bending in semiconductors, which allows a wider range of interface states to be charged and discharged. This increases the net interface charge density at the oxide/CNT interface, causing more significant shift in V_{th} and thus larger hysteresis.

In most logic circuit applications, hysteretic behavior in transistors is considered unfavorable and deemed to be eliminated.[116] However, hysteresis is also a distinctive property that enables memory, which could be harnessed and engineered for neuromorphic computing applications to mimic the behavior of the biological synapse in the human brain. In the human nervous system, a synapse is a gap-junction structure that enables the signal transmission between one neuron cell (presynaptic cell) to another neuron cell or an effector cell (postsynaptic cell) which can actively respond to a stimulus. How strongly the pre- and postsynaptic cells are correlated and can exert influence over each other is evaluated by the weight of the synapse, which can evolve over time and adjust to neuron activities. The adaptation of synaptic weight to the neuron stimulus (usually in the form of action potential) is known as synaptic plasticity. Based on how synaptic plasticity changes in response to different presynaptic action potentials, the synaptic weight can either be increased for an improved signal transmission between two cells through the synapse, decreased for a suppressed signal transmission, or simply remain unchanged. The aforementioned three basic

synaptic plasticities are named potentiation, depression, and elasticity, respectively, and can all be imitated using the sSWCNT artificial synaptic transistors with hysteresis caused by interface states.

4.3   Biomimetic Neurological Functions of sSWCNT Synaptic Transistor

4.3.1   Stimulus and Time-Dependent Plasticity

In a synaptic transistor, the gate terminal is used to imitate the presynaptic neuron, whereas the drain terminal is used to imitate the postsynaptic neuron. The synaptic weight is represented by I_{DS}, which is named postsynaptic current (PSC) in the synaptic transistor context. As explained previously, a negative gate bias will cause a negative shift of the I_{DS}-V_{GS} curve while a positive bias will cause a positive one. When the gate bias is applied in the form of a pulse, the PSC in a synaptic transistor can be modified effectively. For example, a positive gate pulse with sufficient amplitude will result in an immediate increase in PSC (potentiation), whereas a negative gate pulse with sufficient amplitude will induce an immediate drop in PSC (depression). If the amplitude of gate bias is too small to generate noticeable hysteresis, the PSC is likely to remain constant. The amplitude of the action potential that leads to potentiation, depression, or elasticity may have slight variations among different devices, depending on the hysteresis curves of each individual transistor. Figure 4.2a shows the PSC response of the sSWCNT synaptic transistor to three representative presynaptic square wave action potentials (V_{pre}) with different amplitude of $+4$, $+0.5$, and -4 V, all with the same pulse width of 10 ms and baseline of 0 V. The $|V_{DS}|$ is fixed at 1 V during the measurement. The baseline value of the PSC is defined as the average PSC value

66

between 5 and 15 s before the arrival of the V_{pre}, and the PSC data are normalized with respect to this baseline value. Upon arrival of the action potential, $V_{pre} = +4$ V yields a large increase in PSC, which can be interpreted as potentiation of the synaptic weight; V_{pre} = -4 V yields a large decrease in PSC corresponding to depression, and $V_{pre} = +0.5$ V gives elasticity with negligible change in PSC.

For synaptic weight modulation, aside from being stimulus-dependent, the time dependence is also crucial to characterize the memory effect of the artificial synapse. Here, two time-dependent plasticities are proposed, the short-term plasticity (STP) and memory plasticity (MEP). The STP has a time scale on the order of milliseconds to seconds, whereas the MEP is more long-lived and could last for minutes, hours, or even days. In our study, the STP is defined as the amount of percentage change in PSC (ΔPSC) after 1 s of the stimulation of V_{pre}, and MEP is defined as the average ΔPSC between 30 and 50 s after the stimulation. The spike-amplitude-dependent STP and MEP are plotted in Figure 4.2b as a function of the amplitude of V_{pre}, and the results can be well fitted with exponential function in the form of $\Delta \text{PSC} = \mp A_0 \exp(|V_{pre}|/V_A) + w_0$, where V_{pre} is the amplitude of the action potential, V_A is associated with the activation energy of the interface trap states and the "$\mp$" sign indicates the type of plasticity.[117] The value of V_A determines how large the amplitude of V_{pre} needs to be to reach certain amount of STP/MEP. From the device structure point of view, V_A indicates how easily the interface donor/acceptor states can be charged. The smaller the value of V_A, the easier the synaptic transistor can be excited by V_{pre}, thus larger PSC change can be induced. For potentiation and depression, ΔPSC is positive and negative and the corresponding PSC is called excitatory PSC (EPSC) and inhibitory PSC (IPSC), respectively. The fitting equations of MEP and STP by potentiating V_{pre} and depressing V_{pre} are listed in Table 4.1. It is believed that the amount of synaptic vesicles being activated and fusing with a presynaptic membrane to release a neurotransmitter depends on the amplitude of
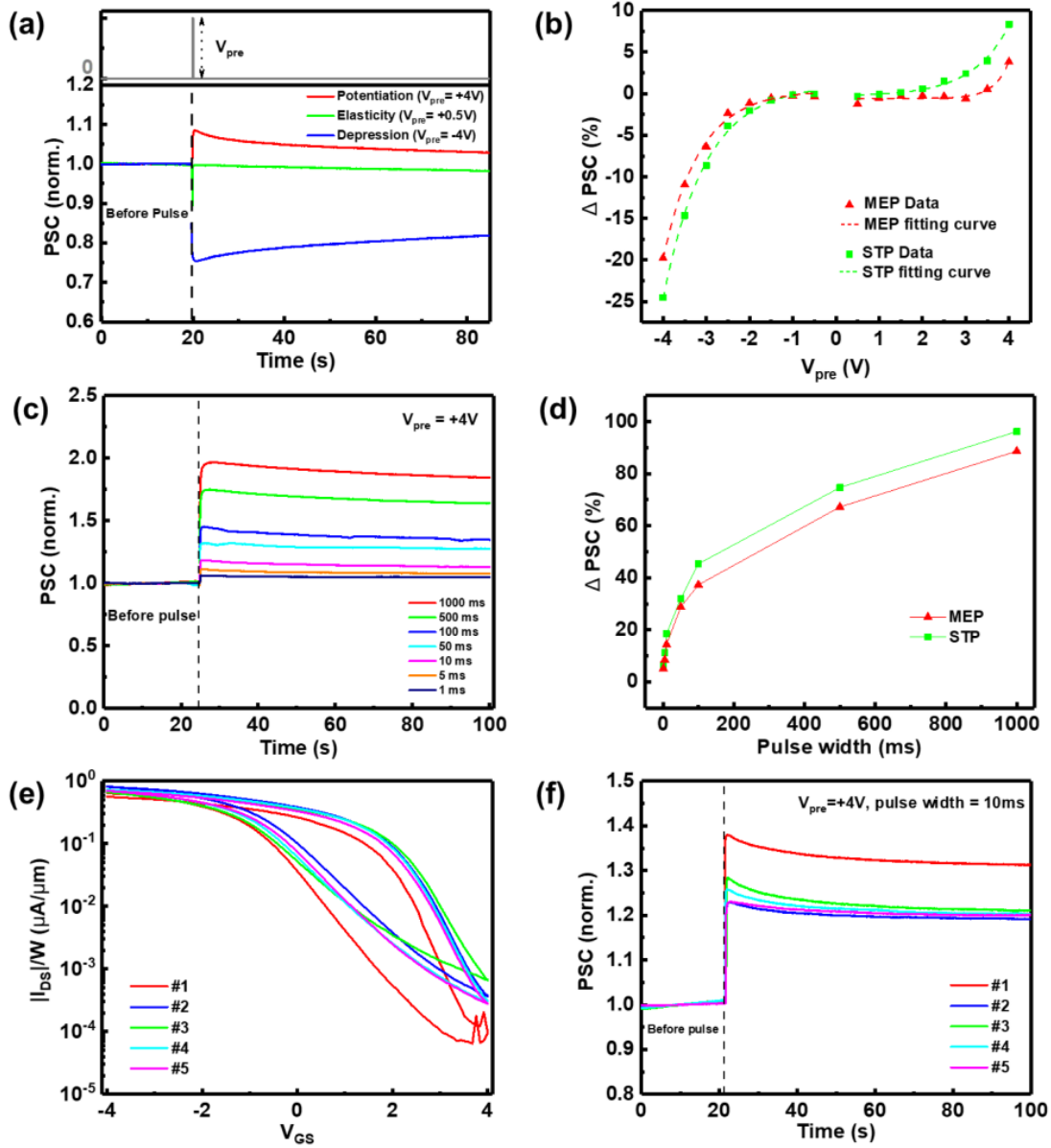
Figure 4.2: (a) Instantaneous PSC (normalized) before and after presynaptic pulse excitation showing potentiation ($V_{pre} = +4$ V), depression ($V_{pre} = -4$ V) and elasticity ($V_{pre} = +0.5$ V). (b) Spike-amplitude dependence of MEP and STP. (c) PSC responses of synaptic transistor with V_{pre} (+4 V) of different pulse width ranging from 1 ms to 1 s. (d) Spike-width dependence of MEP and STP. (e) Double sweep transfer curves of the synaptic transistors showing the hysteresis of different devices. (f) PSC curves of the corresponding devices in Figure e with same excitation of $V_{pre} = +4$ V and pulse width of 10 ms. All measurements are conducted at $|V_{DS}| = 1.0$ V.

68

action potential.[117] In other words, the nature of biological synaptic weight modulation due to the quantitative change of released neurotransmitters is well-represented by the ΔPSC as a result of different magnitude of V_{pre} in the sSWCNT artificial synaptic transistor. To obtain a more comprehensive understanding of how a single action potential can affect the synaptic response of the transistor, action potentials with the same amplitude but different pulse widths are also applied to excite the transistor, and the corresponding PSC responses are measured. Figure 4.2c shows the PSC responses of a synaptic transistor with V_{pre} (+4 V) of various pulse widths ranging from 1 ms to 1 s. The spike-width dependences of STP and MEP are plotted in Figure 4.2d. Results in Figure 4.2c and d suggest a monotonic increase of synaptic response with the increased spike width, which can be attributed to the increased number of charged interface states due to the extended charging time.

From transistor structure and fabrication point of view, device geometry (*e.g.*, channel length L), type of dielectric material being deposited, deposition techniques of the dielectric layer, and the surface treatments of the dielectric layer can all affect the density and distribution of interface trap states, thus affecting the synaptic response of the transistor to V_{pre}. In order to understand the uniformity of the synaptic response, hysteresis curves and PSC curves of multiple devices are measured, and the results are shown Figure 4.2e and f. The synaptic transistors exhibit fairly uniform synaptic responses to the same V_{pre}, suggesting a good controllability over the interface trap states among different devices during the device fabrication processes. The variation of the synaptic behaviors can be attributed to the variation in hysteresis behaviors among transistors.

4.3.2   User-Dependent Plasticity and Flexibility Test

The synaptic behavior is further characterized by user-dependent synaptic plasticity, the change of synaptic weight with regards to the activation history at that synapse. For short-term plasticity, facilitation is one of the most common forms and plays an important role in synaptic computing and information processing.[118, 119] Among the various facilitation forms, PPF is studied by applying a pair of stimuli to the presynapse neuron and monitoring the fractional change of a second response of the synaptic weight to the first one. The magnitude of this fractional change was demonstrated to be a function of the interval between the two action potentials.[120] In our sSWCNT synaptic transistor, the pair of stimuli are emulated by two consecutive presynaptic spikes to the gate of the transistor with an amplitude of +4 V, a width of 10 ms, and a period of 85 ms (*i.e*, duty cycle of 11.76%). The "spike interval" Δt is defined as the time difference between the falling edge of the first spike and the rising edge of the second spike. For the aforementioned spike pair, a Δt of 75 ms is obtained and shown along with the spike pair in the upper panel of Figure 4.3a. It is noted that, for two consecutive pulses ($A1$ and $A2$, shown in bottom panel of Figure 4.3a, the EPSC response is higher for the second peak ($A2$). This behavior was repeatedly observed in multiple experiments and shows how past pulses can be used to increase future EPSC responses, which is indicative of memory behavior. Defined as the percentage of the amplitude of a second spike to the first spike in EPSC, the PPF index is used to evaluate the PPF effect and can vary as the Δt of the presynaptic spikes varies. Figure 4.3b shows the PPF index plotted as a function of Δt, and the plot yields a double exponential curve as the Δt increases from 35 to 1000 ms, indicating that the PPF behavior is characterized by two phases with different relaxation time constants. The obtained data can be fitted well by the equation PPF index = $C_1 \exp(-\Delta t/\tau_1) + C_2 \exp(-\Delta t/\tau_2) + C_0$,[108] where C_1 and C_2 are the maximum amounts of each facilitation phases and τ_1 and τ_2 are the time constants of the

relaxation in each phase. The time constants τ_1 and τ_2 determine how fast the PPF index decays with the increase of spike interval Δt. The larger the value of τ_1 and τ_2, the slower the decay of PPF index would be. From the device structure point of view, τ_1 and τ_2 are also associated with the oxide/semiconductor interface trap states as they indicate how long the charges can retain in these trap states. Detailed fitting equation can be found in Table 4.1. Compared with biological synapse with $\tau_1 \approx 50$ ms and $\tau_2 \approx 300$ ms,[121] our artificial sSWCNT synaptic transistor resembles its biological counterpart with similar PPF behavior.

The facilitation behavior of STP was studied further beyond PPF in information processing function of a synapse. For example, when an animal travels through different locations in a particular environment, certain regions in its hippocampus would fire sequences of spike discharges to the synapses to be processed.[122] The frequency of this train of spikes, usually containing spatial information, can vary and induce different animal behaviors, indicating filtering characteristics of the synapse. In our study, a train of spikes comprising 10 pulses with a width of 1 ms, an amplitude of $+4$ V, and frequencies ranging from 5 to 100 Hz are applied to the artificial synaptic transistor (Figure 4.3c). The EPSC yields a peak once a pulse from the train arrives, and the amplitude gain of the EPSC is defined as the ratio of the height of the peak after the tenth pulse ($A10$) and the height of the peak after the first pulse ($A1$), expressed as $A10/A1$. Figure 4.3d shows the gain of EPSC plotted as a function of the spike train frequency, and the result shows that the amplitude gain increases from 3.3 to 12.5 as the frequency increases from 5 to 100 Hz, suggesting the high-pass filtering behavior of our artificial synaptic transistor. This result is in good accordance with simulations reported in the literature showing elevated synaptic strength (weight) with increasing stimulus frequency.[122]

The ability of the synapse to gradually modulate its synaptic weight by periodic spikes from presynaptic neurons can be emulated by the channel conductance-switching behavior of
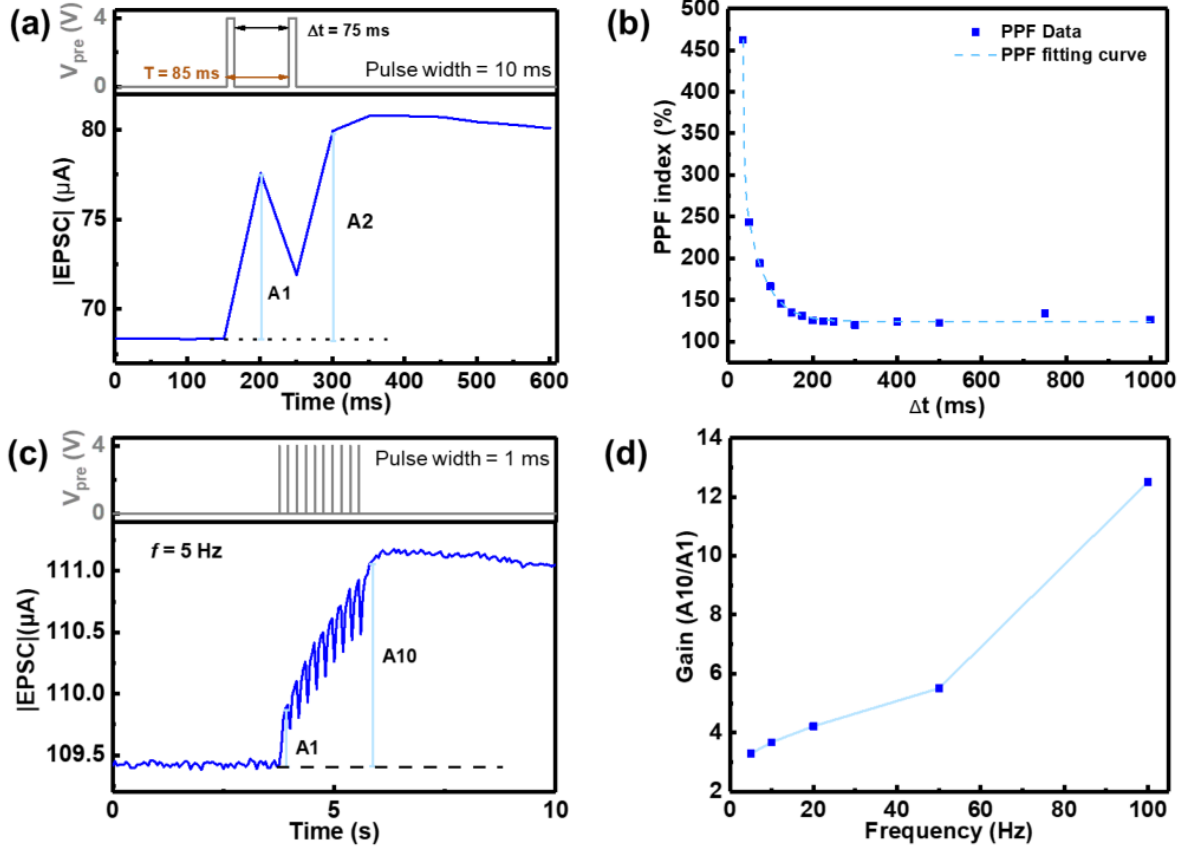
Figure 4.3: Short-term facilitation characteristics of the sSWCNT synaptic transistor. (a) Paired-pulse facilitation measurements showing EPSC change triggered by two consecutive pulses with a spike interval Δt of 75 ms. $A1$ and $A2$ are the height of the peaks in EPSC upon the arrival of the first pulse and the second pulse, respectively. (b) PPF index (defined as $A2/A1 \times 100\%$) plotted as a function of different spike intervals. (c) EPSC change triggered by a train of 10 pulses with a frequency of 5 Hz. $A1$ and $A10$ are the height of the peaks in EPSC upon the arrival of the first pulse and the last pulse, respectively. (d) Amplitude gain (defined as $A10/A1 \times 100\%$) plotted as a function of pulse train frequency showing the high-pass filtering characteristics of the synaptic transistor. All the measurements are conducted at $|V_{DS}| = 1.0$ V.

the artificial synaptic transistor, where the conductance of the channel can be discretely adjusted by the presynaptic pulses and thus exhibit different analogue states.[42, 43] With $|V_{DS}|$ fixed at 1 V, the value of the channel conductance, $G = I_{DS}/V_{DS}$, is equal to PSC, thus the modulation of the conductance could be represented by the EPSC and IPSC change. The potentiation and depression conductance modulation tests are carried out by applying a train of 140 presynaptic spikes with a pulse width of 10 ms, a pulse period of 1 s, and a pulse amplitude of +4 V for potentiation or -4 V for depression. Because of the outstanding mechanical robustness of sSWCNT and the very thin ($\sim 10\mu$m) polyimide substrate used, the sSWCNT synaptic transistors are expected to exhibit good flexibility, and thus bendability and endurance of the synaptic transistors are also examined in this measurement. Figure 4.4a shows the potentiation and depression conductance modulations under different bending conditions. In a relaxed state, the range of the total potentiation conductance modulation after 140 pulses is measured to be 98.9% and and total depression conductance modulation is measured to be -80.3%, according to the Eqs.(4.1) and (4.2)

$$\Delta G_{total\ pot.} = \frac{EPSC_{max} - EPSC_{min}}{EPSC_{min}} \times 100\% \qquad (4.1)$$

$$\Delta G_{total\ dep.} = -\frac{IPSC_{max} - IPSC_{min}}{IPSC_{min}} \times 100\% \qquad (4.2)$$

The inset images in Figure 4.4a reveal the detailed view of the conductance tuning by 20 applied pulses with each small "step" of the postsynaptic current (the value of EPSC or IPSC 1 s after the arrival of a pulse), representing a discrete analogue channel conductance state. Compared with traditional crossbar-structured memristor with limited dynamic range of conductance modulation,[41] the large tuning range of channel conductance of our synaptic transistor could enhance the efficiency of neuromorphic computing when the device
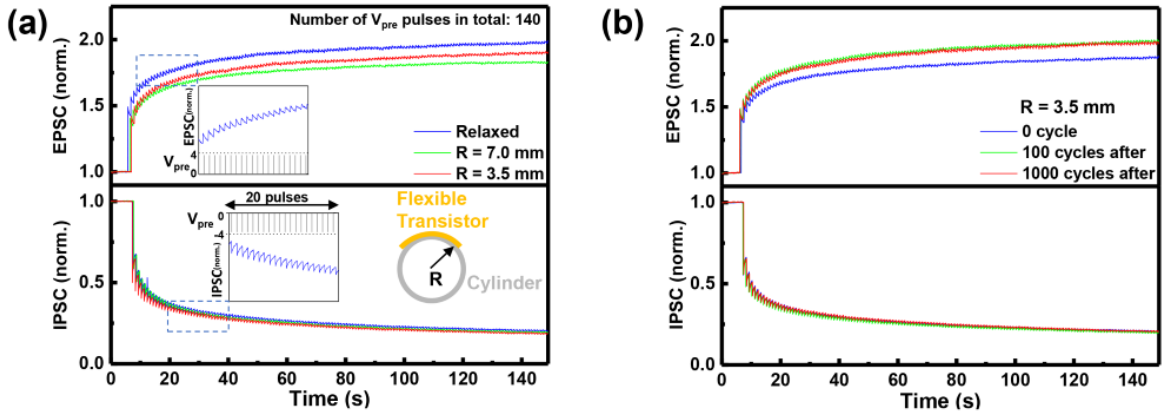
Figure 4.4: Synaptic weight modulation behavior and bending and cyclic tests of synaptic transistor. (a) Synaptic weight modulation curves of a synaptic transistor measured at various curvature radii. Inset: Zoomed-in view of a segment of the modulation curves with 20 cycles showing the detailed change of PSC under potentiating (top) and depressing (bottom) presynaptic action potentials. (b) Synaptic weight modulation curves after various numbers of bending cycles at curvature radius of 3.5 mm. All measurements are conducted at $|V_{DS}| = 1.0$ V.

is implemented in the artificial neural system.[42, 49] For the flexibility tests, the modulation curves of the device in Figure 4.4a exhibit only slight variations under potentiation and negligible changes under depression when the sample is bent down to a curvature radii of 7.5 mm and 3.5 mm, respectively. The modulation curves exhibit similar behavior under cyclic bending tests when the sample is repeatedly bent to a curvature radius of 3.5 mm for up to 1000 cycles, as shown in Figure 4.4b. The results demonstrate the outstanding mechanical flexibility and robustness of the sSWCNT synaptic transistor and thus capacitate the device for applications in soft wearable electronic systems.

In a biological synapse, the synaptic weight responds not only to the action potential from a presynaptic neuron but also to the reflected postsynaptic action potential when the signal is passing through the axon of the postsynaptic neuron.[123] When the time correlation of pre- and postsynaptic spikes follows certain learning rules, a specific memory plasticity known as spike-timing-dependent plasticity (STDP) arises and is regarded as a fundamental process to

74

understand the activity-dependent development in the human brain.[107] In Figure 4.5a, the postsynaptic spike is emulated by a ramped wave with a period of 190 ms being applied to the drain terminal of the synaptic transistor. The postsynaptic spike starts at a baseline of $+1$ V, linearly ramping up to $+2$ V in 90 ms, decreasing to 0 V in 10 ms, and ramping up again to the baseline of $+1$ V in 90 ms. The presynaptic spikes are two 10 ms square waves adjacent to each other and with opposite polarities (amplitude $= +4$ V for the first square wave and -4 V for the second square wave). As shown in Figure 4.5a, the timeline midpoint of the pre-
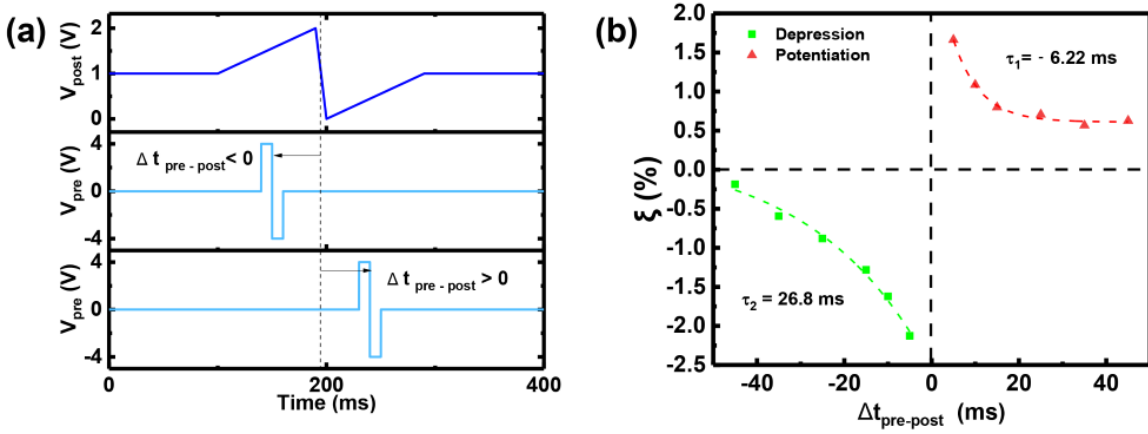
Figure 4.5: Spike-time-dependent plasticity of synaptic transistor. (a) Waveforms of post-synaptic spike and presynaptic spike. (b) Plots of parameter ζ (same value as MEP) of synaptic transistor as a function of different presynaptic and postsynaptic time interval values ($\Delta t_{pre-post}$). Result shows a typical anti-Hebbian STDP behavior.

and postsynaptic spike is defined as t_{pre} and t_{post}, and the spike time difference, $\Delta t_{pre-post} = t_{pre}\text{-}t_{post}$, is used as an indicator of the arrival time sequence of pre and postsynaptic spikes. A negative $\Delta t_{pre-post}$ indicates the arrival of presynaptic spike precedes the postsynaptic spike, and a positive $\Delta t_{pre-post}$ indicates the arrival of a presynaptic spike succeeds the postsynaptic spike. The parameter ζ, which is defined as the MEP value of the synaptic transistor after the activation by both the pre- and postsynaptic spikes, is adapted to characterize the STDP behavior of the device. Figure 4.5b shows the data of ζ plotted as a function of $\Delta t_{pre-post}$;

Table 4.1: Summary of fitting curve equations in synaptic behavior measurements.

Name of the measurement	Equation	$\mathbf{R}^2$
STP (potentiation)	$\Delta PSC = \text{-}0.290 + 0.0739 \cdot \exp(V_{pre}/0.843)$	0.993
STP (depression)	$\Delta PSC = 1.076 \text{-} 0.435 \cdot \exp(-V_{pre}/0.980)$	0.998
MEP (potentiation)	$\Delta PSC = \text{-}0.571 \text{-} 4.087 \cdot 10^{-5} \cdot \exp(V_{pre}/0.345)$	0.956
MEP (depression)	$\Delta PSC = 0.392 \text{-} 0.174 \cdot \exp(-V_{pre}/0.841)$	0.996
PPF	$PPF\ index = \ 3.941 \cdot 10^7 \cdot \exp(-\Delta t/2.835) +$ $363.1 \cdot \exp(-\Delta t/45.10) + 123.82$	0.999
STDP (potentiation)	$\zeta = 0.610 + 2.350 \cdot \exp(-\Delta t_{pre-post}/6.22)$	0.993
STDP (depression)	$\zeta = 0.266 \text{-} 2.819 \cdot \exp(\Delta t_{pre-post}/26.81)$	0.990

the results indicate that positive $\Delta t_{pre-post}$ generates potentiation in the synaptic transistor, whereas negative $\Delta t_{pre-post}$ generates depression. For both potentiation and depression, when the arrival time of the pre- and postsynaptic spike are more correlated (*i.e*, smaller absolute value of $\Delta t_{pre-post}$), greater change in synaptic weight is observed. The measured STDP data can also be fitted with exponential functions, and the time constants are extracted to be 6.22 ms for potentiation and 26.8 ms for depression (see Table 4.1 for detailed fitting equations). The results exhibit a typical anti-Hebbian STDP form[107] and may be utilized in neuromorphic networks for learning and pattern recognition.[42]

4.4 Demonstration of Neurological E-skin with FENG and sSWCNT synaptic transistor

In the human nervous system, the tactile information is picked up by the mechanoreceptors that reside in human skin and passed through the axon of its peripheral nerve in the form of action potential. The action potential containing the information is relayed to the CNS, which then signals other neuron cells or body parts to execute appropriate responses. Flexible tactile transducers such as triboelectric nanogenerator[68] or ferroelectret nanogenerator[66] can be

readily used to convert external force stimulus to a pulsed electrical signal without the need for a power supply, and they exhibit behaviors that closely resemble skin mechanoreceptors. In this study, a flexible polypropylene-based FENG device reported in our previous work is used as the tactile transducer due to its high efficiency and biocompatibility, as shown in Figure 4.6a.[67] A mechanical input (displacement, force, pressure) generates dipole moments across polypropylene's thickness, creating an electric field that is compensated by the accumulation of charge of opposite polarities at both surfaces of the material. This charge can be collected through thin metal film contacts on the polymer surface, resulting in a small electrical current that is proportional to the rate of change in the applied mechanical input, and flows in opposite directions depending on the direction of the input cycle (*e.g.*, compression/ relaxation). This unregulated electrical output pulse from the FENG needs to be regulated using the rectifying and amplifying circuits illustrated in Figure 4.6b. In brief, the pulsed current signal from FENG is first rectified by a p-n junction diode, which serves as a half-wave rectifier to remove the negative component. The rectified current signal will subsequently charge the capacitor in a RC circuit, creating an initial voltage V_0 across that capacitor. Following the zero-input response equation of a first-order RC circuit, the responsive voltage across the capacitor can be written as $v(t) = V_0 \exp(-t/\tau_T), t \geq 0$, which decays exponentially with time constant $\tau_T = R_L C_L$. When the discharged capacitor is recharged by subsequent current pulses, $v(t)$ will increase exponentially to V_0 with the same τ_T. In this study a τ_T of 30 ms is set, producing a theoretical rise/fall time of 66 ms (2.2 τ_T) of the voltage pulse. It is worth noting that while the rise and fall time of the voltage pulse are mainly controlled by τ_T, the period and duty cycle of that pulse are primarily controlled by the period of the applied force to the FENG. The pulsed voltage signal from RC circuit is then sent to the positive input terminal ($V_{IN}{}^+$) of an instrumentation amplifier (TI INA118) and the output of which is amplified as $V_{OUT} = G(V_{IN}{}^+ - V_{IN}{}^-)$, where G is the voltage gain and $G = (50$ k$\Omega/R_G) + 1$. The R_G value in the present work of 10 kΩ results in a theoretical voltage
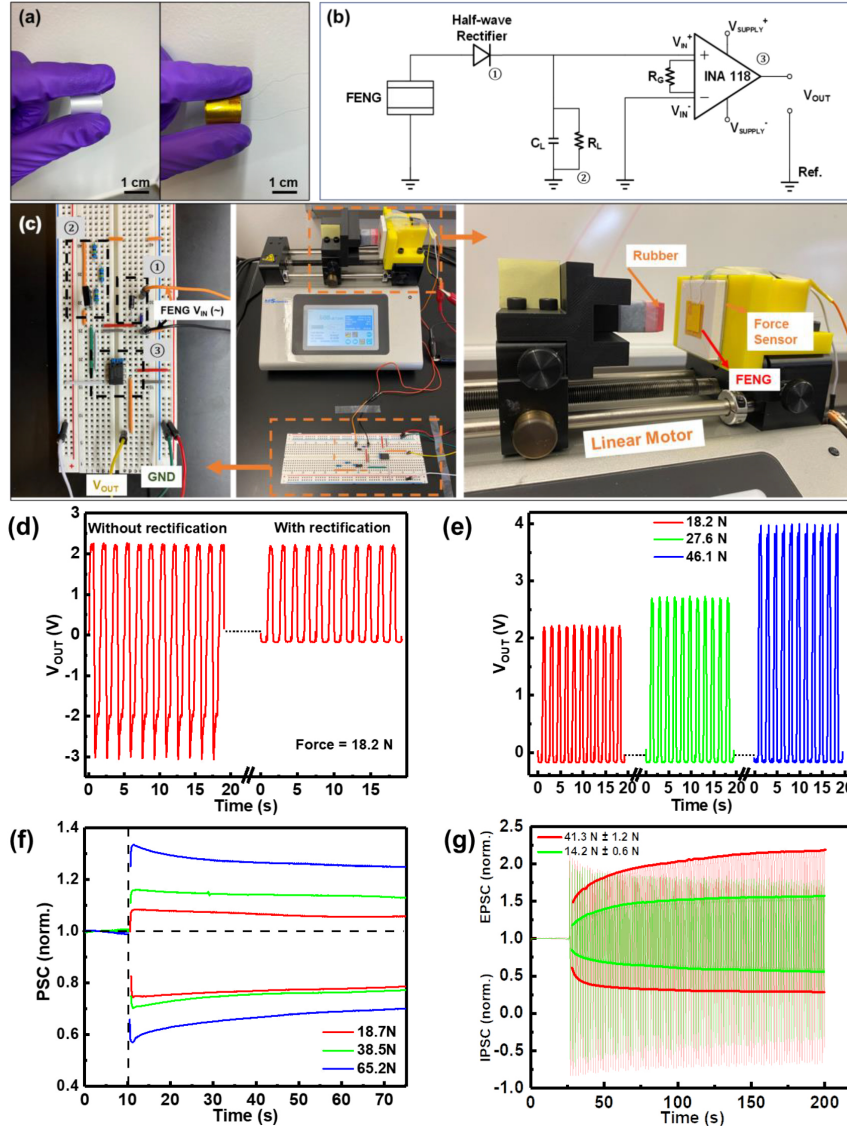
Figure 4.6: Artificial electronic sensory skin with the mechanoreceptor implemented by a FENG and its peripheral nerve implemented by a sSWCNT synaptic transistor. (a) Photograph of a 1.2×1.2 cm^2 flexible FENG film. Left: Pristine PPFE film. Right: Complete FENG device with sputtered silver electrodes and PI encapsulation. (b) Schematic of FENG and the regulating circuit. (c) Photograph of the actual regulating circuit (major components marked in numbers with respect to circuit diagram in (b)) and the mechanical loading test setup. (d) Output signal V_{OUT} with and without half-wave rectification. (e) Rectified output signal V_{OUT} under different loading forces. (f) Instantaneous PSC change (normalized) of a synaptic transistor under different loading forces. (g) Synaptic weight modulation curves measured with periodical loading forces of 41.3 or 14.2 N at a frequency of 0.67 Hz. Solid lines: Peak values of EPSC or IPSC. Background: Measured raw EPSC and IPSC data. All synaptic behavior measurements are conducted at $|V_{DS}| = 1.0$ V.

gain of 6. The amplified pulsed voltage output (V_{OUT}) from the amplifier is then sent to the gate terminal of the sSWCNT synaptic transistor as the presynaptic action potential. This signal processing circuit avoid the impedance mismatch between the FENG and synaptic transistor and allows the tuning of the action potential pulse through altering the period of loading force, time constant of RC circuit, and gain of the amplifier. In Figure 4.6c, the actual implementation of a rectifying and amplifying circuit is displayed on the left side, and the mechanical loading test setup used for generating pulses in the FENG device is shown on the right side. The loading force is exerted by a rubber piston with a contact area of 1.2×1.2 cm^2 mounted on a horizontal-moving linear motor (Legato 110 syringe pump, kd Scientific), and a PI-encapsulated FENG device (1.2×1.2 cm^2, same area as piston head) is mounted on the stationary scaffold with a commercial force sensor (FSR01CE, Ohmite) placed behind the nanogenerator to precisely monitor the magnitude and frequency of the applied forces by the motor. During the measurement, the rubber piston is carefully aligned with the thin-film FENG and pushed toward the device with preset moving distance. Both the V_{OUT} and the force sensor resistance are measured by a semiconductor device analyzer (Keysight B1500A). Figure 4.6d shows the V_{OUT} signal with and without the rectification, and the rectified V_{OUT} signal will be subsequently used as presynaptic action potential pulse for the synaptic transistor. The data show that a train of rectified positive pulses with an average amplitude of 2.2 V, a period of 1.68 s, and a duty cycle of 56.5% is generated with a loading force of 18.2 N and a frequency of 0.67 Hz. Additionally, the amplitude of V_{OUT} increases monotonically with increasing loading force, as shown in Figure 4.6e. The average amplitude of the signal increases from 2.2 to 4.0 V as the applied force increases from 18.2 to 46.1 N with the same frequency. A small negative voltage drift ($\sim$150 mV) of the V_{OUT} signal is observed due to the input offset voltage of the instrumentation amplifier (driven by dual voltage supply of -15 and +15 V). This voltage drift can potentially be reduced using a high-quality amplifier with better precision in our future study. It is also worth mentioning

that the polarity of the pulse can be readily inverted by interchanging the input terminals from $V_{IN}{}^{+}$ to $V_{IN}{}^{-}$ in the amplifier, which allows both potentiation and depression to be achieved in the synaptic transistor.

Finally, the integration of the flexible FENG device with a flexible sSWCNT synaptic transistor to emulate the behavior of a neurological electronic skin is demonstrated. Figure 4.6f shows the instantaneous synaptic weight modulation of the artificial synaptic transistor by the force-encoded presynaptic action potentials. For STP values of potentiation and depression, the synaptic weight changes under a force stimulus of 18.7 or 65.2 N are +8.44 or +32.62% and -25.15 or -41.17%, respectively. Similarly, for MEP values of potentiation and depression, the synaptic weight changes under force stimulus of 18.7 or 65.2 N are +6.07 or +26.05% and -22.60 or -32.10%, respectively. The data are normalized to the baseline PSC, which is defined as the average PSC from 0 to 5 s. The results above show that an increased magnitude of the force stimulus perceived by FENG is transduced into greater change in PSC and thus greater modification of synaptic weight. The history-dependent, discrete modulation of synaptic weight under continuous stimulation has also been studied, and the results are presented in Figure 4.6g. Trains of 100 potentiating and depressing action potential pulses with a frequency of 0.67 Hz are generated by stimulating the FENG with forces of 41.2 or 14.2 N and relayed to the synaptic transistor to be processed. In Figure 4.6g, the peak values of PSC change to each potentiation or depression pulse are sorted out and connected by a solid line to show the trend of synaptic weight modification, with the real-time actual responses of PSC also shown in the background. The synaptic weight responses of the transistor show gradual analogue modulation of the synaptic weight similar to what is shown in Figure 4.4. After 100 action potential spikes from the FENG, a total synaptic weight modification of +118.9 or +56.5% for potentiation at 41.3(±1.2) or 14.2(±0.6) N and -72.1 or -44.3% for depression at 41.3(±1.2) or 14.2(±0.6) N can be

observed. The variation in the loading force is due to the slight movement of the supporting scaffold during the continuous measurement. Successfully reproducing analogue-like synaptic weight modulation with force-encoded information further demonstrates the feasibility of interfacing a FENG-driven circuit with a sSWCNT synaptic transistor as a sensory electronic skin and nerve. This is a step toward the use of flexible electronic devices for neuroprosthetics applications.

4.5 Summary

In summary, we have demonstrated a biomimicking sensory electronic skin system whose neurological function of biological synapse is realized by a flexible sSWCNT artificial synaptic transistor. Temporal synaptic behaviors such as STP and MEP have been demonstrated with potentiating, depressing, or elastic action potentials at different amplitudes, widths, and polarities. Short-term and history-dependent nature of the synaptic transistor is elaborated by PPF, high-pass filtering characteristics, and synaptic weight modulation behavior, whereas long-term learning and memory ability of the transistor is represented by the STDP. The sensory function of the electronic skin is achieved using a FENG as the sensor, which directly generates pulsed electrical signals or action potentials in response to force stimuli. By integrating a synaptic transistor with the sensory component of the electronic skin, tactile information containing the magnitude and activating history of the force stimuli is successfully transduced and relayed to the presynaptic terminal of the synaptic transistor and then processed and transmitted in the form of change in synaptic weight. By interfacing with motor units of animal or human bodies in the future, our sensory electronic skin can have the potential of facilitating the advancement of wearable neuromorphic applications such as an artificial nerve system or smart medical prosthetics.

Chapter 5

Multimodal Artificial Neurological Sensory-Memory System (Neurological Sensory E-skin) Based on Flexible Carbon Nanotube Synaptic Transistor

5.1   Introduction

For many years, the artificial intelligence has been striving to imitate and reproduce the abilities of human brain to perform critical and sophisticated tasks such as decision-making, reasoning and learning. These logic and cognitive functions of brain, however, is not innate and stationary. Just as other living animals, the neural system of human being will persistently evolve over the progression of its surrounding ecological and social environment through physical (visual, auditory, somatosensory, *etc.*) contacts and interactions, which is majorly

enabled by the human sensory system. Such evolution of human intelligence is considered fundamentally as a memory-based process.[124] The sensory information from different sensory receptors will be integrated, processed and memorized in the neural system, which could serve as the key factor in implementing consequential decision, cognition, or learning/memory tasks. Due to the special structural and functional characteristics of sensory receptors, neurons and synapses, it is hard to faithfully emulating the biological sensory and memory nervous systems in traditional von Neumann architecture without costing considerable computational resources.[51] Thus, new approaches to artificial intelligence have sprung from the idea that intelligence can emerge as much from artificial sensory-memory system consists of biomimetic sensors and synaptic devices, as it does from artificial neural network algorithms and models. Thanks to the advancement in microelectronic design and fabrication technologies, the artificial sensory-memory system can even be achieved in flexible formats.[7] This means such a sensory-memory system holds the potential of being wearable and can be considered as E-skin with neurological functions.[125]

In human sensory system, four types of sensory receptors constitute the foundation of five basic human senses (sight, hearing, touch, smell and taste): photoreceptors, mechanoreceptors, thermoreceptors and chemoreceptors.[126] Among the different categories of receptors, photoreceptors are specialized in visual phototransduction and are concentrated around center of the retina, whereas the mechanoreceptors are more widely distributed around the human body. The mechanoreceptors can be found in the human skin to transduce touch, stretch and in the ear to transduce sound. The electronic analogues of photoreceptors can be readily implemented by photodetectors,[127, 128] or photosensitized synaptic devices.[129, 130] The realization of electronic mechanoreceptors, on the other hand, prefers versatile device that can transduce mechanical signal in different forms. Among the flexible artificial mechanoreceptors

based on change of resistance,[60] change of capacitance,[9] piezoelectricity,[10] or triboelectricity,[68] polypropylene-based ferroelectret nanogenerator (FENG) has been demonstrated to be efficient in generating pulsed electrical signals in response to tactile stimuli and sound vibrations, as described in Chapter 2, Section 2.2.

When the sensory receptors receive external stimuli, they will first transduce different forms of physical stimuli into information-encoded, brain-interpretable electrical pulses called "action potentials", as shown in Figure 5.1. The action potentials will then be passed along the axon of the neuron to central neural system to be processed. The synapse, functioning as an essential structure between the input (pre-synaptic) neuron and the target (post-synaptic) neuron, permits the transmission of action potentials from one neuron to another. The synapse also possesses the ability to adjust its own strength (synaptic weight) in response to the information contained in the input action potentials and will maintain that change of strength even after the extinction of input. Such a behavior is generally known as "synaptic plasticity" and it is widely accepted as one of the fundamental cellular mechanisms that underlies the formation of memory and learning operations in human brain.[4] The structure and behavior of the biological synapse can be emulated by synaptic transistor in which the synaptic weight is represented by the channel conductance (G). The modification of channel conductance in response to the pulsed gate signals can be regarded as the electronic analogue of synaptic plasticity, which leads to the artificial synapse-like memory.

In this study, an artificial multimodal sensory-memory system (neurological sensory E-skin) has been developed and endowed with bioreceptor-like sensory capability and synaptic-like memory to mimic the biological sensory-memory behaviors. Three out of the five human basic sensing abilities- touch, hearing and sight are enabled by utilizing FENG as both tactile sensor and acoustic sensor and phototransistor as optical sensor. The physical stimuli are converted to information-containing electrical pulses and then relayed through regulating circuits into
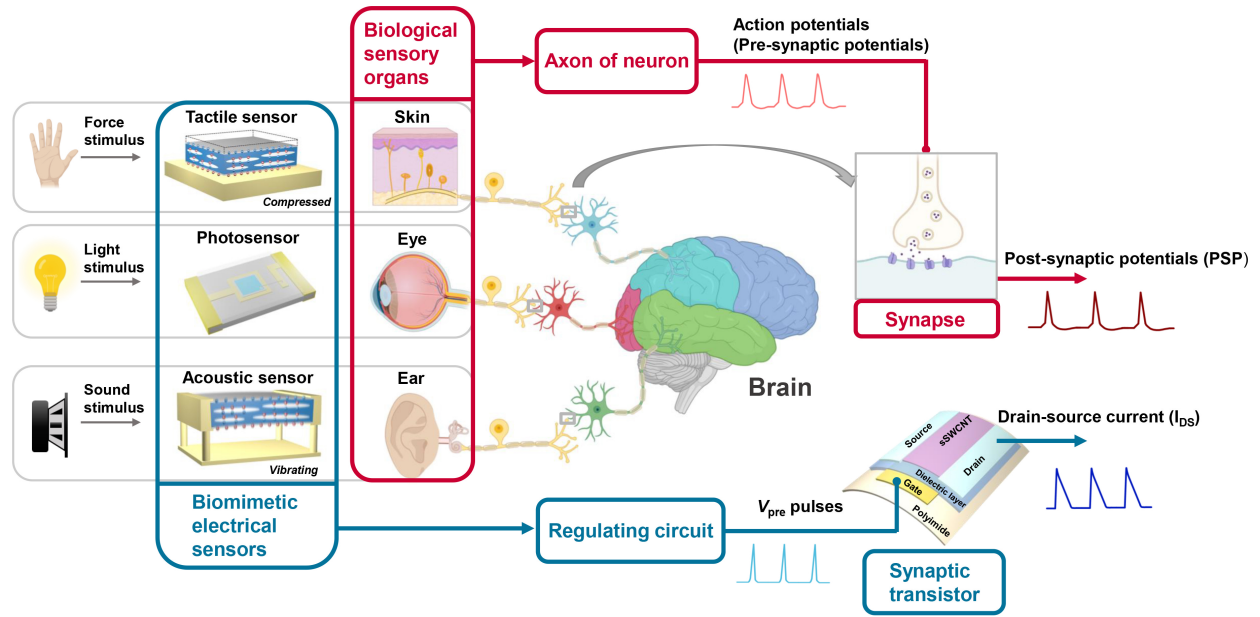
Figure 5.1: Schematic illustration of biological visual, auditory and tactile sensory organs and process of information transmission and storage through neuron and synapse (circled and highlighted in red), in comparison with the artificial sensory-memory system consisting of corresponding biomimetic physical sensors and artificial synaptic transistor (circled and highlighted in blue). The schematic illustration is partially created with BioRender.com.

the artificial nervous system, represented by the flexible semiconducting single-wall carbon nanotube (sSWCNT) synaptic thin-film transistor, to be processed and stored. The synaptic weight response behaviors (synaptic plasticity) of the artificial synaptic transistor to single-pulse stimulus and continuous, long-term stimuli from visual, auditory and tactile- induced electrical pulses with different input stimulus intensities have been systematically studied to characterize the dynamic modification profiles of the synaptic memory. Based on this sensory-memory system, we manage to reproduce some well-known human memory and learning models. The multi-store model of memory (Atkinson–Shiffrin memory model), which describes the memory states transition from short-term memory to long-term memory through rehearsal, is imitated by applying sequences of visual stimuli with different number of repetitions and different light intensities. The classical conditioning experiment (Pavlov's dog's experiment), which established the associative learning model, is also investigated by

85

synergizing visual and auditory stimuli and monitoring the learning behavior of the synaptic transistor in response to the individual and interrelated stimuli. The "brain-like" intelligence achieved through this artificial multimodal sensory-memory system may be used for imitating multiplex and multifunctional biological sensory and nervous system and may open up a new avenue for constructing environment-interactive artificial intelligence.

5.2 Characterization of Sensing Components

The pulsed electrical output signals from the visual, auditory and tactile sensory circuit are presented in Figure 5.2a, b and c, respectively. In a sensory-memory system, the sensory transduction process can be regarded as the "pre-synaptic" process. The electrical pulses generated from these sensory circuits will eventually be relayed to the artificial synapse to be processed, thus these electrical pulses (action potentials) can also be called pre-synaptic pulses (V_{pre}). As shown in Figure 5.1, these sensory circuits are analogous to the photoreceptors and mechanoreceptors in biological sensory organs such as eye, ear, and skin. According to the types of input signal, the output V_{pre} can be categorized into visual V_{pre}, auditory V_{pre} and tactile V_{pre}.

5.2.1 Optical Sensor

As illustrated in the inset of Figure 5.2a, a periodical sequence of light pulses representing the visual stimuli can be transduced into the corresponding sequence of visual V_{pre} through an ambient-light phototransistor and the regulating circuit-A (circuit diagram in Figure 5.3a). The pulsed signals originate from Keysight 33510B waveform generator and are sent to a white light LED (Ø=5 mm, US-EL-CP-010, ELEGOO) to generated pulsed visual stimuli. The ambient light phototransistor (Ø=5 mm, ALS-PT243-3C/L177, EVERLIGHT) is placed

43 mm away from the LED to transduce the visual stimuli, a photometer (1330B-V Digital Light Meter, DR. METER) is placed at the same position as the phototransistor to monitor the input light intensities of the visual stimuli. The visual pre-synaptic pulses are measured and recorded by an oscilloscope (Analog Discovery 2, DIGILENT) at sample rate of 400 Hz. The detailed diagrams of phototransistor are shown in Figure 5.3b and 3c, and the details the visual V_{pre} are summarized in Table 5.1.
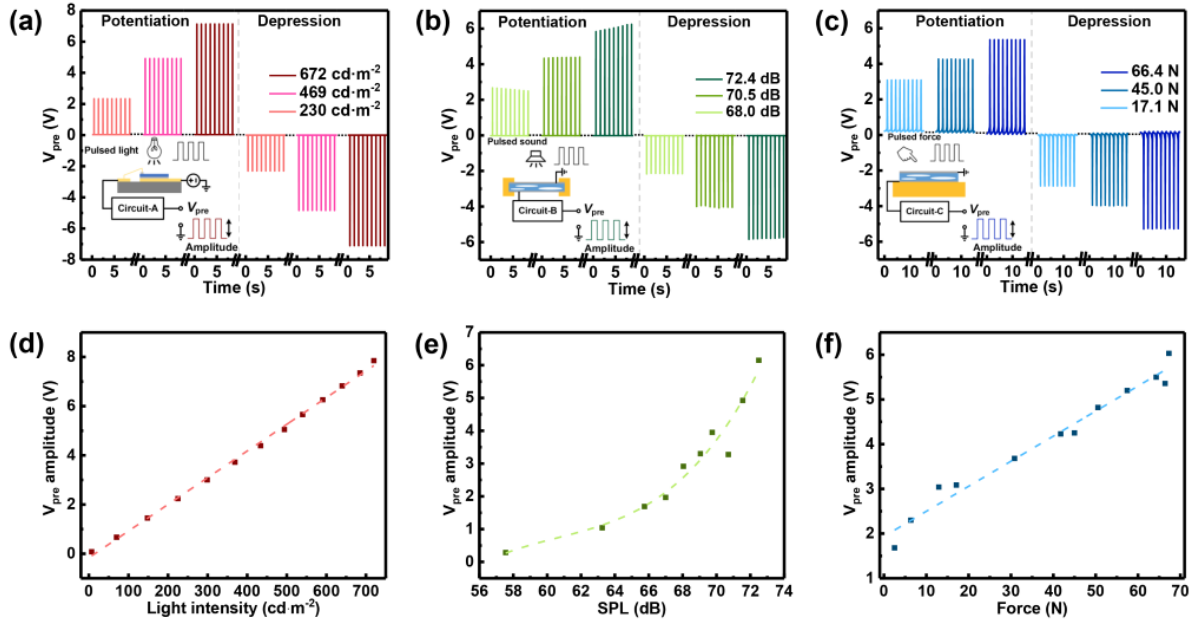
Figure 5.2: Transduction characterizations of the multimodal sensory system. Potentiation (positive) and depression (negative) pre-synaptic pulses (V_{pre}) induced by (a) visual stimuli, (b) auditory stimuli, and (c) tactile stimuli. Inset of each figure: simplified illustration of the corresponding transduction process. (d) Plot of the amplitudes of visual V_{pre} versus the light intensities of input visual stimuli. (e) Plot of the amplitudes of auditory V_{pre} versus the SPLs of input auditory stimuli. (f) Plot of the amplitudes of tactile V_{pre} versus the forces of input tactile stimuli. In panels d-f, the dashed lines represent the fitting curve with the fitting equations shown in Table 5.1.

For biomimetic synaptic weight modulation, both potentiation pulses (pulses that cause the increase of the synaptic weight) and depression pulses (pulses that cause decrease of

the synaptic weight) are required, and this potentiation-depression pulses pair are usually represented by electrical pulses with opposite polarities. This can be realized by interchanging the output terminals of the regulating circuit-A through a switch, whereas for integrated optoelectronic synaptic device, a combination of light pulses and electrical pulses are often required to achieve the bidirectional synaptic weight modulation.[131] In this study, the potentiation pulse is represented by a positive pulse while the depression pulse is represented by a negative pulse. Figure 5.2a shows that near-symmetrical potentiation and depression pulses are generated successfully under the same light intensity of visual stimuli, which will be crucial for achieving symmetrical long-term plasticity profile in synaptic devices.[43] Moreover, Figure 5.2a also shows that visual stimuli with greater incident light intensity result in visual V_{pre} with greater amplitude. The amplitude of visual V_{pre} is increased from 2.3 V to 7.1 V when the light intensity is increased from 230 cd·m^{-2} to 672 cd·m^{-2}, suggesting a positive correlation of the input light stimuli and the generated electrical signals. This positive correlation is further quantified by plotting the visual V_{pre} amplitudes as a function of incident light intensities in Figure 5.2d. The data can be well fitted by a linear curve, and the detailed fitting equation can be found in Table 5.1. This positive and linear correlation between the incident light intensity and visual V_{pre} amplitude can be explained by the linear relationship between photocurrent and light intensity (Figure 5.3d).

5.2.2   Acoustic and Tactile Sensor

The flexible FENG sensors are made from PPFE films. The PPFE film (80 μm in thickness, Emfit Corporation) is sputter-coated with Ag film (500 nm, Hummer X, Anatech Inc) on each side. After the deposition of the two Ag electrodes, they are wired out through copper wires and tapes. For the acoustic sensor application, only the Ag electrode- copper wire connection area is covered with polyimide film (20 μm, Kapton) as protection layer. For the
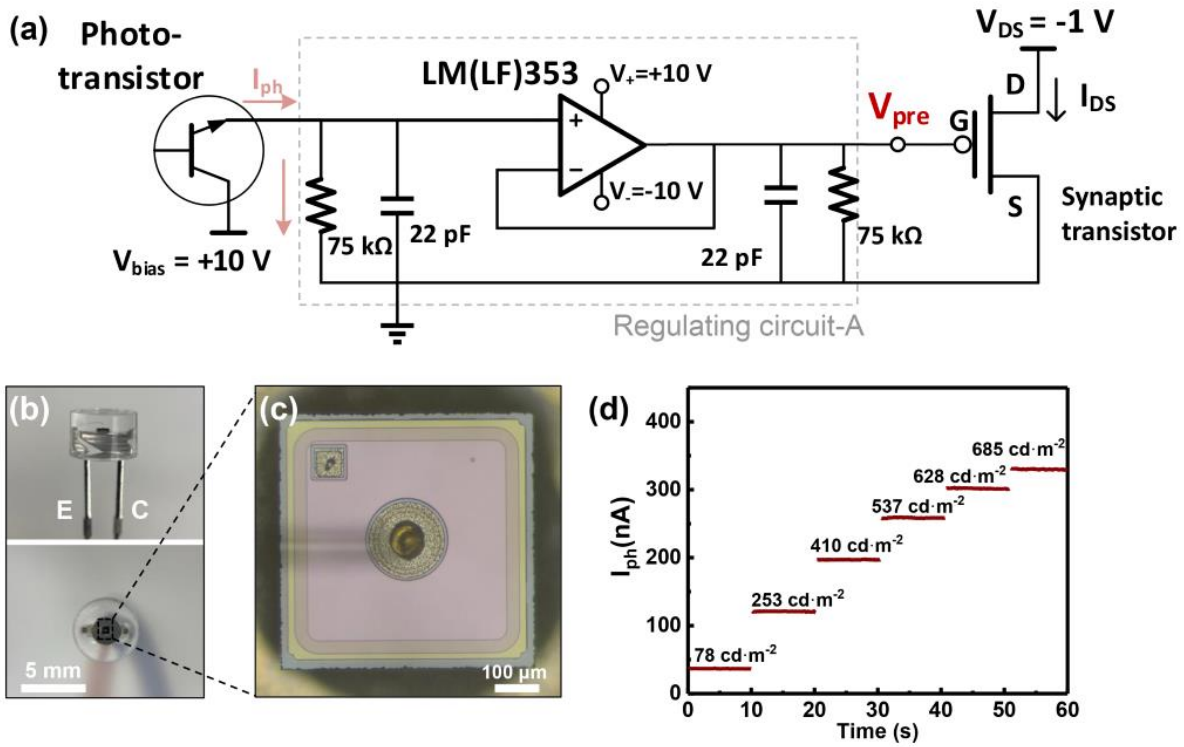
Figure 5.3: (a) Schematic illustration of the visual sensory-memory system circuit. (b) Photograph of the ambient-light phototransistor. Top: side view, bottom: top view. (c) Top view microscopic image of the phototransistor core. (d) Photocurrent-input light intensity characteristic curve.

force sensor application, the whole FENG device is encapsulated by the polyimide film as protection layer.

The transduction of auditory stimuli and tactile stimuli are enabled by utilizing the same flexible polypropylene-based ferroelectret nanogenerators (FENG), but in different form factors and operating modes. When external mechanical perturbations are applied along the perpendicular direction to the FENG's surface, the perturbations will induce a change of internal dipole moments in the FENG, altering the electrical field distribution within the film and producing free charges at the surface electrodes, which eventually give rise to the output electrical signals. The inset of Figure 5.2b shows the schematic illustration of the acoustic signal transduction, where the FENG operates in a "freestanding" mode with only

89

the four edges of the FENG fixed in a frame to allow free vibration of the film. In contrast, for transduction of tactile inputs, the FENG operates in a "blocked" mode with one side of the FENG firmly supported by a rigid substrate (inset of Figure 5.2c).
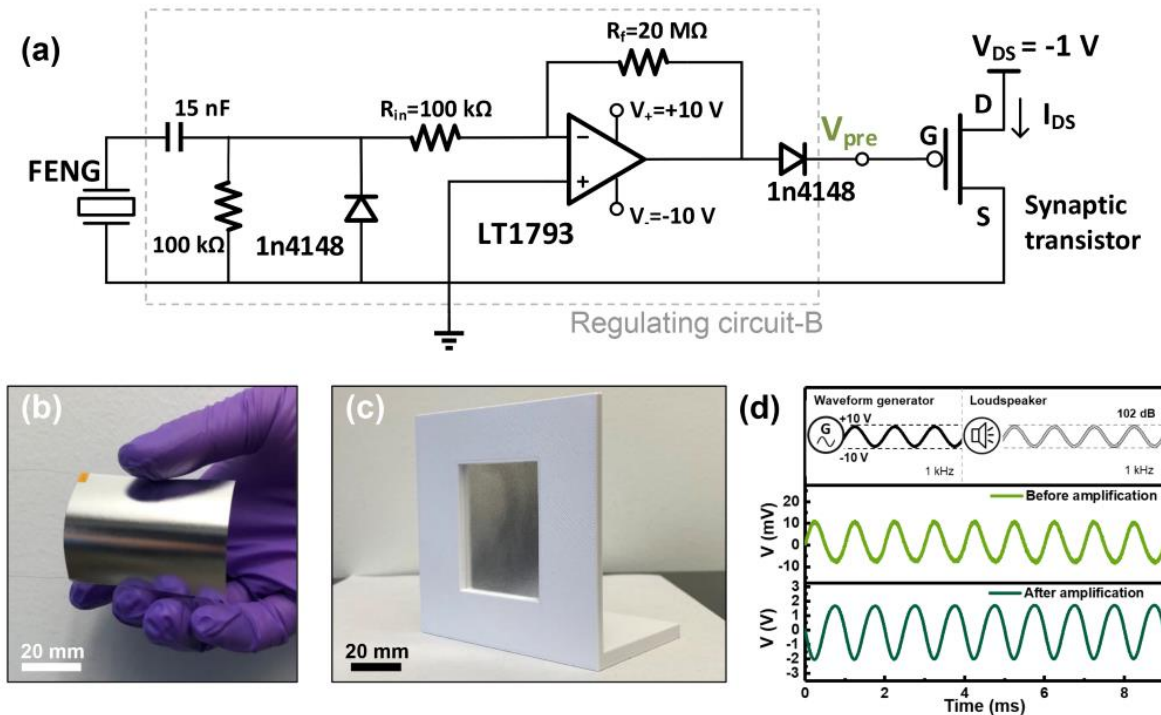
Figure 5.4: (a) Schematic illustration of the auditory sensory-memory system circuit. (b) Photograph of the FENG as acoustic sensor (before mounting on the scaffold). (c) Photograph of the FENG as acoustic sensor on the scaffold. (d) Sound vibration transduction test of FENG as acoustic sensor.

Apart from the difference in operation modes, because the pressure induced by an acoustic signal is generally much lower compared to tactile stimulus, FENG with a larger effective area of 4×5 cm^2 (optical image in Figure 5.4b) and regulating circuit-B (circuit diagram in Figure 5.4a) with a much higher gain of 200 are needed to transduce and amplify the auditory stimulus. In contrast, for handling the tactile stimulus, FENG device with an effective area
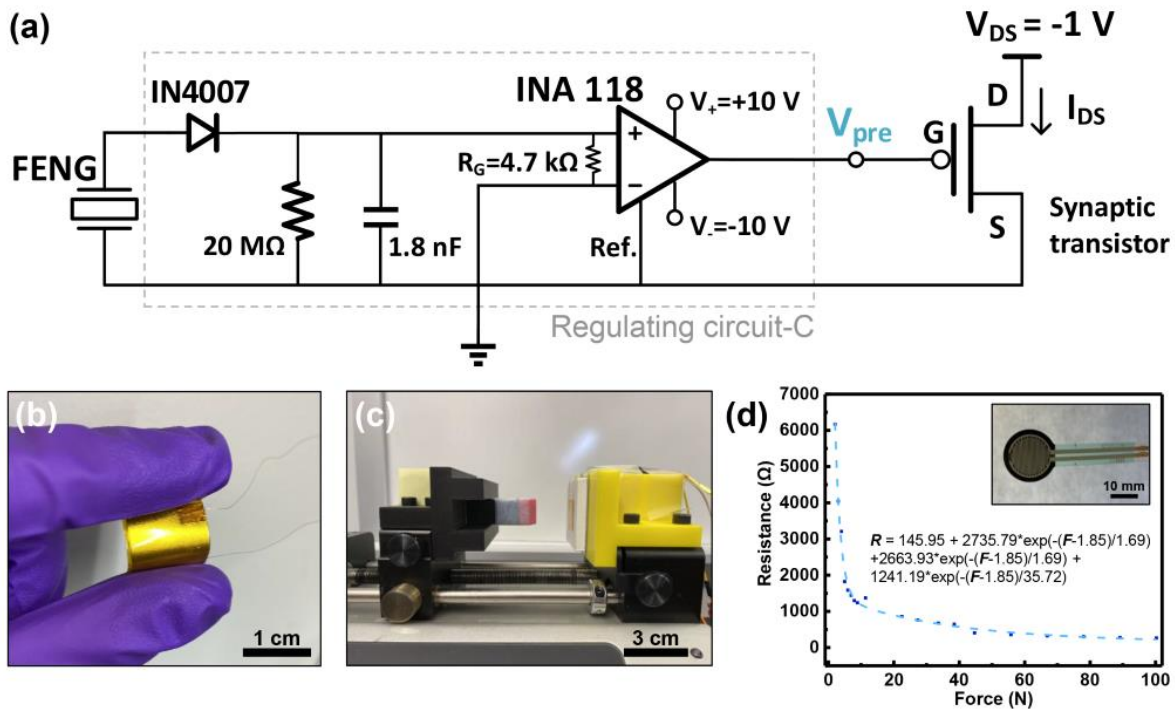
Figure 5.5: (a) Schematic illustration of the tactile sensory-memory system circuit. (b) Photograph of the FENG as tactile sensor. (c) Photograph of the mechanical loading test setup. (d) Calibration curve and fitting equation of the resistance change-based commercial force sensor (Ø=0.5", force sensing resistor, POLOLU). Inset: photograph of the commercial force sensor.

of 1.2×1.2 cm^2 (optical image in Figure 5.5b) and regulating circuit-C (circuit diagram in Figure 5.5a) with a moderate gain of 11 are used. To further demonstrate the ability of FENG to transform small auditory vibrations into noticeable electrical signals, as shown in the Figure 5.4d, sinusoidal sound wave with frequency of 1 kHz, sound pressure level (SPL) of 102 dB is generated by a loudspeaker and then delivered to the FENG. The pristine transduced electrical signal shows the same frequency of 1 kHz as the input sound wave and V_{pp} of near 20 mV. After amplification, the waveform retains the frequency and shows an amplified V_{pp} of near 4 V, which confirms the transduction and amplification fidelity of the acoustic FENG sensor and circuit.

For auditory stimulus generation and detection, the pulsed signals originate from the Keysight 33510B waveform generator and are sent to a loudspeaker (Ø=3", HiFi full-range, DROK) to generated pulsed auditory stimuli. The FENG film is attached to a scaffold (as shown in Figure 5.4c) with an open window and aligned with the center of the loudspeaker and is placed 2 cm away from the loudspeaker. A decibel meter (HT-80A Decibel Meter, RISEPRO) is placed at the same position as the FENG to monitor the input SPLs of the auditory stimuli. The auditory pre-synaptic pulses are measured and recorded by an oscilloscope (Analog Discovery 2, DIGILENT) at sample rate of 800 Hz. For tactile stimulus generation and detection, The PI-encapsulated FENG is mounted on a fixed scaffold and is aligned with a rubber piston mounted on a linear motor (Legato 110 syringe pump, kd Scientific). The loading test setup is shown in Figure 5.5c. During the experiment, the rubber piston will be brought in contact with the FENG periodically with preset frequency and moving distance, generating pulsed compressive tactile stimuli. A commercial force sensor (Ø=0.5", force sensing resistor, POLOLU, shown in Figure 5.5d) is placed in tandem with the FENG to measure the magnitude of the applied force. The tactile pre-synaptic pulses are measured and recorded by an oscilloscope (Analog Discovery 2, DIGILENT) at sample rate of 400 Hz.

As illustrated in the inset of Figure 5.2b and c, periodical acoustic pulses with different SPLs are used as the input auditory stimuli and periodical compression with different levels of applied force are used as the input tactile stimuli, respectively. Similar to visual V_{pre} in Figure 5.2a, near-symmetrical potentiation and depression pulses with opposite polarities can also be generated with both auditory and tactile stimuli as shown in Figure 5.2b and c. Figure 5.2b and c also show monotonic increase in generated electrical signals for auditory and tactile stimuli with increasing intensity. Specifically, the amplitude of generated auditory V_{pre} increases from 2.6 V to 6.0 V when the SPL is increased from 68.0 dB to 72.4 dB and the amplitude of tactile V_{pre} increases from 3.1 V to 5.4 V when the force is increased from

Table 5.1: Summary of multimodal generation process of physical stimuli, characterizations of V_{pre}, polarity switching methods of V_{pre} and V_{pre} amplitude- stimulus intensity fitting equations.

Stimulus type	Visual	Auditory	Tactile
Generation of the physical stimuli	Waveform generator (square pulses, 1 Hz, 1% duty cycle, tunable amplitudes) → White-light LED	Waveform generator (square pulses, 1 Hz, 1% duty cycle, tunable amplitudes) → Loudspeaker	Linear motor (0.67 Hz, tunable moving distances)
Induced presynaptic pulses (V_{pre})	Square pulses, 1 Hz, 10 ms pulse width, various amplitudes	Composite triangular pulses, 1 Hz, 5-6 ms pulse width (major peak),various amplitudes	Triangular pulses, 0.6 Hz, 180-200 ms pulse width, various amplitudes
Switching polarity of V_{pre}	Toggle the two output terminals of regulating circuit-A that connect to the G and S of the synaptic transistor	Toggle the direction of the diode that connects to the G of the synaptic transistor	Toggle the two input terminals of the amplifier
V_{pre} amplitude (V)-input stimulus intensity (s) fitting curve equation	$V=0.0107s-0.164$ $R^2=0.998$	$V=0.00208s^3-0.375s^2+23.0s-480$ $R^2=0.953$	$V=0.0547s+1.937$ $R^2=0.972$

17.1 N to 66.4 N. The amplitudes of auditory V_{pre} as a function of SPLs can be fitted with a polynomial curve (Figure 5.2e) and the amplitudes of tactile V_{pre} as a function of the applied forces can be fitted with a linear curve (Figure 5.2f). More details about the auditory and tactile V_{pre} and the fitting equations can be found in Table 5.1.

5.3 Synaptic Response Measurement of The Synaptic Transistor

As illustrated in Figure 5.1, after the action potentials are generated by the input sensory circuits, in order to mimic the behavior of the biological synapses, flexible sSWCNT artificial synaptic transistors developed and reported in our previous work have been utilized.[125]

The optical and microscopic images of the transistor are shown in Figure 5.6a and b. The hysteretic transfer characteristics of the transistors that are caused by the charge trap states at the interface between the carbon nanotube and the gate oxide,[125] which lead to the synaptic behavior are presented in Figure 5.6c. The gate terminal of the synaptic transistor is
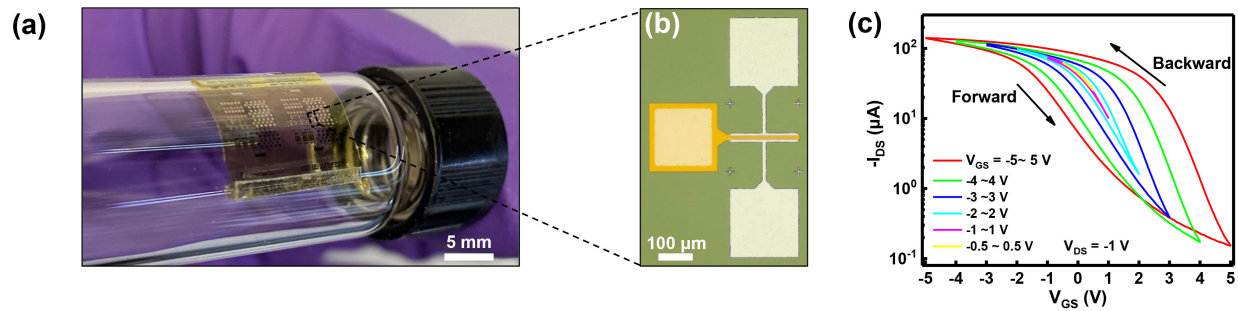
Figure 5.6: (a) Photograph of flexible sSWCNT synaptic transistors on polyimide substrate. (b) Microscopic image of a representative synaptic transistor with channel length (L) of 10 μm and channel length (W) of 200 μm. (c) Bi-directional transfer curves (I_{DS}-V_{GS}) of the synaptic transistor showing the levels of hysteresis under different ranges of V_{GS} sweeping.

treated as the pre-synaptic neuron and the drain terminal is treated as post-synaptic neuron. With the drain-to-source voltage (V_{DS}) fixed at a constant value of -1 V, the synaptic weight of the synaptic transistor can be represented by either the drain-to-source current (I_{DS}) or the channel conductance (G). When a positive gate pulse is applied to the synaptic transistor, the channel conductance increases immediately and this enhancement in conductance will be maintained after the gate pulse is off. This is known as potentiation. Similarly, when a negative gate pulse is applied to the synaptic transistor, the channel conductance decreases immediately and this degeneration will also be maintained after the gate pulse is off. This is known as depression. The changes of synaptic weight in response to different electrical pulse activations are collectively called "synaptic plasticity".

5.3.1 Single-Pulse Plasticity Measurement

Figure 5.7a, b and c show the synaptic plasticity of the sSWCNT synaptic transistor in response to a single potentiation V_{pre} and depression V_{pre} with different stimulating intensities from visual, auditory and tactile stimulus, respectively. Before the measurements, the baselines of the channel conductance for potentiation tests are initiated to stable low conductance states ($G < 10$ μS) through negative gate pulses tuning and the baselines of the channel conductance for depression tests are initiated to stable high conductance states ($G > 60$ μS) through positive gate pulses tuning. After the application of single pulse, it can be seen clearly that the potentiation (positive) pulse leads to an increase in channel conductance while the depression (negative) pulse leads to a decrease in channel conductance. This phenomenon is in accordance with our previous report and confirms that positive V_{pre} will lead to potentiation while negative V_{pre} will lead to depression.[125] Furthermore, in order to study the synaptic plasticity of the synaptic transistor to the input stimulus intensity, for the same set of tests where the polarities and categories of pre-synaptic pulses are the same but only intensities are different, the baselines of the channel conductance are initiated at the same value before the measurements. The results in Figure 5.7a, b and c show that the physical stimulus with higher intensity can lead to greater channel conductance change, thus larger synaptic plasticity, suggesting the successful signal transmission between multimodal sensory inputs and the sSWCNT artificial synaptic transistor. In this study, the maximum conductance change in 20 s after the input pulse, noted as the ΔG_{peak}, is utilized to characterize the short-term plasticity of the synaptic transistor, whereas the average conductance change between 60 s and 80 s after the input pulse, noted as ΔG_{mem}, is utilized to characterize the retention of the plasticity, which can also be seen as the "memory" of the synaptic transistor. Figure 5.7a shows $|\Delta G_{peak}|$ increases from 13.4 μS to 40.7 μS for potentiation and from 4.38 μS to 42.42 μS for depression when input light intensity increases from 230 cd·m^{-2} to 672
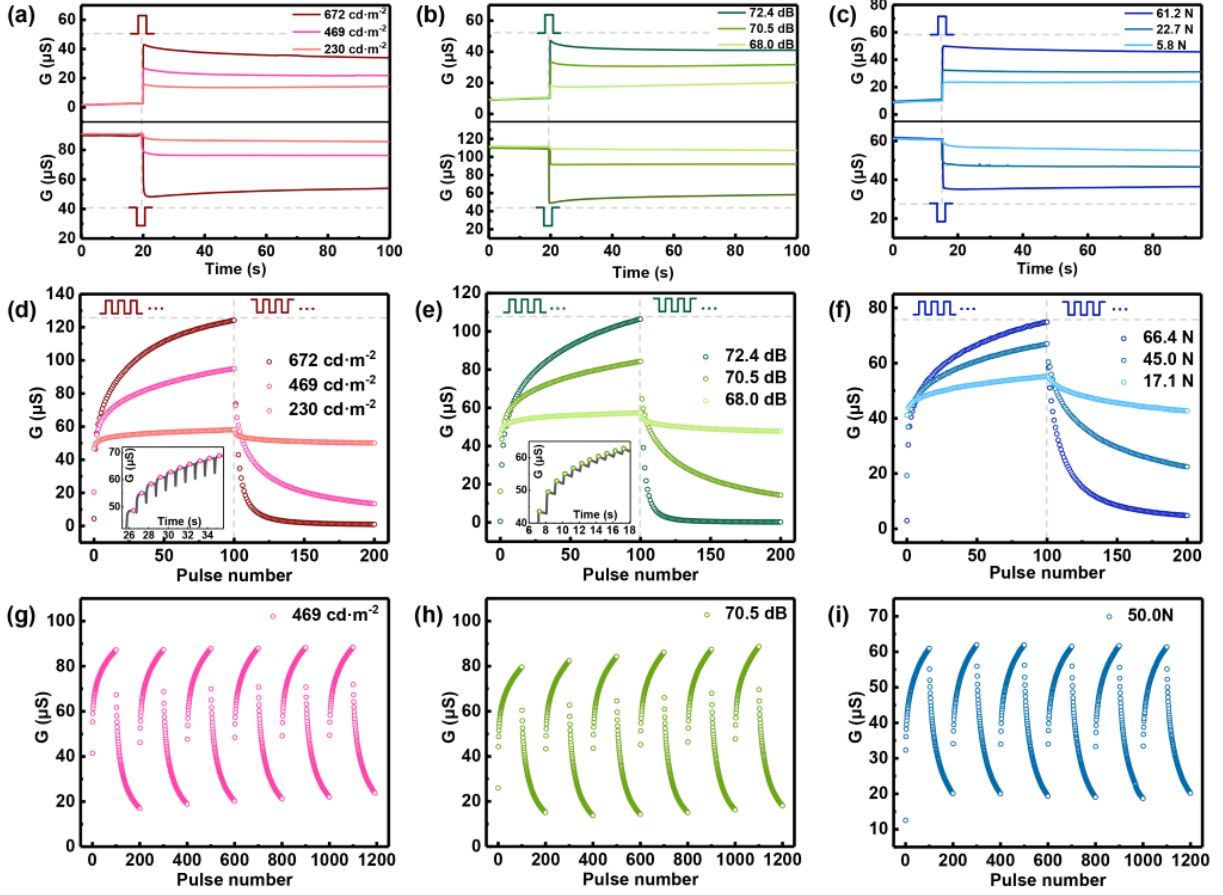
Figure 5.7: Single-pulse plasticity and long-term plasticity characteristics of the artificial synaptic transistor. (a-c) Single-pulse plasticity curves of synaptic transistor in response to a single potentiation or depression pre-synaptic pulse induced by (a) visual stimulus, (b) auditory stimulus, and (c) tactile stimulus with various stimulation intensities. (d-f) Long-term plasticity profiles of the synaptic transistor in response to a sequence of potentiation and depression pre-synaptic pulses (100 each for potentiation and depression) generated from (d) periodic visual stimuli with different light intensities. Inset: detailed time-domain conductance response curve (2nd to 11th pulse with a light intensity of 469 cd·m^{-2}); (e) periodic auditory stimuli with different SPLs. Inset: detailed time-domain conductance response curve (2nd to 12th pulse with a SPL level of 70.5 dB); (c) periodic tactile stimuli with different values of force. (g-i) Repeatability and endurance tests of synaptic transistor in response to extended period of (g) visual V_{pre}, (h) auditory V_{pre}, and (i) tactile V_{pre}.

96

cd·m^{-2}. The corresponding $|\Delta G_{mem}|$ also increases from 12.0 μS to 32.4 μS for potentiation and 5.27 μS to 36.4 μS for depression, which indicates a positive correlation of ΔG_{peak} and ΔG_{mem} with the incident light intensity. Similar phenomena can also be observed in Figure 5.7b for auditory stimulus and Figure 5.7c for tactile stimulus. The detailed values of ΔG_{peak} and ΔG_{mem}, as well as the retention rate, which is defined as $(\Delta G_{peak}\,/\Delta G_{mem}) \times 100$ %, for all three kinds of physical stimuli are plotted in Figure 5.8 and summarized in Table 5.2. The results show that for all forms (visual, auditory, tactile) and intensities of the physical stimuli studied, over 80% for the retention rate of the single pulse plasticity can be achieved, suggesting a good synapse-like memorization behavior of the synaptic transistor.

5.3.2   Long-Term Plasticity Measurement

While memory can be regarded as the foundation of human intelligence, the perceptual capability of human can be further enhanced through practice or training, that is, the repetition of external stimuli in a periodic way and thus perceptual learning is enabled. In artificial sensory-memory system, such learning behavior can be preliminary characterized by the long-term plasticity measurement, which is conducted by applying sequences of periodical potentiation and depression presynaptic pulses to the synaptic device and monitoring the modulation of channel conductance with respect to each of the input V_{pre}. Figure 5.7d, e and f show the long-term plasticity curves of the synaptic transistor with one hundred visual, auditory, tactile potentiation and depression V_{pre}, respectively, and the inset of the Figure 5.7d and e show the detailed time-domain modulation curve of the synaptic transistor by visual and auditory V_{pre}. In the measurement, the intensity of the input physical stimuli has also been varied to study the change of long-term plasticity profile under different stimulation conditions. In Figure 5.7d, e and f, the channel conductance starts from its minimum value (G_{min}) and then reaches the maximum value (G_{max}) after the potentiation V_{pre} sequence

and gradually fall back to close to G_{min} after the depression V_{pre} sequence, suggesting a symmetrical conductance modulation profile for potentiation and depression. In Figure 5.7d, for input visual stimuli with light intensity of 672 cd·m^{-2}, 469 cd·m^{-2} and 230 cd·m^{-2}, the conductance modulation range (G_{max}-G_{min}) is 123.2 μS, 81.6 μS, and 11.3 μS, respectively, and the on/off ratio (G_{max}/G_{min}) is 131.2, 7.07 and 1.24, respectively. For long-term plasticity measurements with auditory and tactile stimulation, the results are similar to the visual stimulation above and the detailed data for (G_{max}-G_{min}) and (G_{max}/G_{min}) are summarized in Table 5.2. From the results above, it is clear that the V_{pre} sequences with different stimulation intensities are perceived as distinct long-term plasticity profiles by the sensory-memory system. The high-intensity long-term stimuli result in wide-range, swift tuning of the conductance with the modulation value of each step being large, whereas the low-intensity long-term stimuli show a small-range, delicate tuning profile, with the modulation value of each step being small. For potential applications in a neurorobotic system, one can utilize the change in synaptic weight (G or I_{DS}) of the controlling synaptic device to trigger movement of the actuator, thus different biomimetic locomotion can be enabled.[52, 59, 132, 133] By potentially interfacing the sensory-memory system with neurorobotic actuating component, the distinct long-term plasticity profiles can be further utilized to enable different modes of actuation. As an example, according to Figure 5.7d, in order to achieve similar conductance tuning range from approximately 45 μS to 55 μS, one may choose to use high intensity light stimulus (672 cd·m^{-2}) to accomplish the conductance modulation from 46.53 to 55.97 μS (ΔG=9.44 μS) with only one step (one light pulse) in the "swift mode"; or use moderate intensity light stimulus (469 cd·m^{-2}) to modulate the conductance from 46.80 μS to 56.44 μS, (ΔG=9.81 μS) within two steps (two light pulses) in the "coarse mode". Such swift or coarse mode operation can lead to fast response and large movement of the actuator. With low intensity light stimulus (230 cd·m^{-2}), the system operates in the "fine mode" and a much more subtle adjustment of the conductance can be achieved. This allows 50 discrete conductance states

or 50 steps to be established within the conductance range of 46.80 μS to 56.44 μS (ΔG=9.64 μS), which may empower the actuator to perform slower but more intricate motion or gesture.
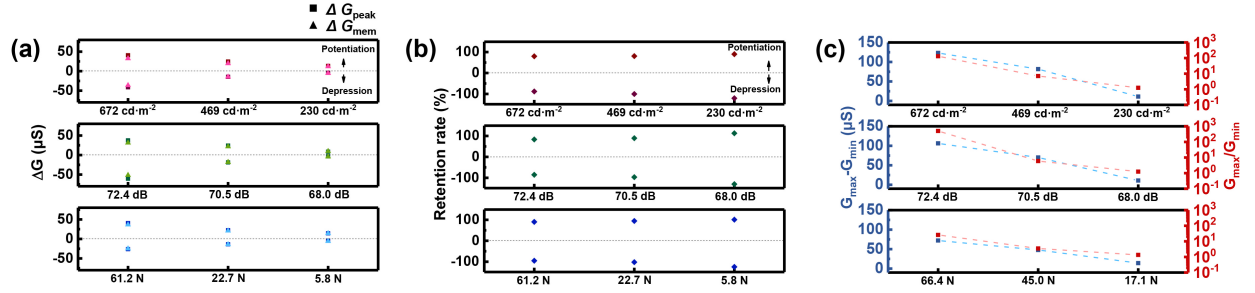
Figure 5.8: (a) Plots of conductance plasticity ΔG_{peak} and ΔG_{mem} induced by visual, auditory and tactile stimulus under different stimulating intensities. (b) Plots of retention rate (ΔG_{peak} /$\Delta G_{mem}\times$ 100 %) of visual, auditory and tactile stimulus- induced plasticity. (c) Plots of conductance modulation range (G_{max}-G_{min}) and on/off ratio (G_{max}/G_{min}) in long-term plasticity measurements with periodical visual, auditory and tactile stimuli under different stimulating intensities. Detailed values of ΔG_{peak}, ΔG_{mem}, retention rate, G_{max}-G_{min}, and G_{max}/G_{min} are summarized in Table 5.2 below.

5.3.3 Flexibility and Stability Test

To further examine the electrical stability and endurance of the synaptic transistor to the V_{pre}, the long-term plasticity measurement is repeated for 6 cycles and the plasticity profiles of visual, auditory and tactile stimuli are shown in Figure 3g, 3h and 3i, respectively. After the initial cycle, the plasticity curves are stabilized and show only slight cycle-to-cycle variations, suggesting a high modulation uniformity and operating stability of the artificial sensory-memory system. Due to the very thin polyimide substrate ($\sim 10\mu$m) used and the mechanical robustness of the sSWCNT networks,[33] the long-term plasticity tests have also been successfully conducted with the synaptic transistor bent to a curvature radius of 7.5 mm. As illustrated in Figure 5.9a and b, the conductance modulation curves of auditory

Table 5.2: Summary of ΔG_{peak}, ΔG_{mem}, retention rate, G_{max}-G_{min}, and G_{max}/G_{min} values in Figure 5.8.

Stimulus type	Visual			Auditory			Tactile		
Stimulus intensity(single-pulse plasticity)	**672 cd·m^{-2}**	**469 cd·m^{-2}**	**230 cd·m^{-2}**	**72.4 dB**	**70.5 dB**	**68.0 dB**	**61.2 N**	**22.7 N**	**5.8 N**
$\Delta G_{peak}(\mu S)$-potentiation	40.74	24.62	13.36	37.54	24.28	8.62	40.54	22.16	14.31
$\Delta G_{mem}(\mu S)$-potentiation	32.45	19.83	12.02	31.31	21.65	9.71	36.51	20.95	14.441
Retention rate(%)-potentiation	79.65	80.55	89.94	83.42	89.16	112.75	90.05	94.54	100.92
$\Delta G_{peak}(\mu S)$-depression	-41.42	-14.50	-4.38	-60.54	-18.89	-3.15	-26.22	-13.77	-4.61
$\Delta G_{mem}(\mu S)$-depression	-36.45	-14.53	-5.27	-51.60	-18.28	-4.09	-24.92	-14.05	-5.75
Retention rate(%)-depression	88.00	100.22	120.46	85.22	96.78	130.08	95.05	102.07	124.62
Stimuli intensity(long-pulse plasticity)	**672 cd·m^{-2}**	**469 cd·m^{-2}**	**230 cd·m^{-2}**	**72.4 dB**	**70.5 dB**	**68.0 dB**	**66.4 N**	**45.0 N**	**17.1 N**
G_{max}-$G_{min}(\mu S)$	123.25	81.61	11.31	106.19	69.99	10.97	72.00	47.73	14.09
$G_{max}/G_{min}(\mu S)$	131.19	7.07	1.24	500.17	5.90	1.24	25.83	3.48	1.34

stimuli and visual stimuli exhibit only slight variations under bending state compared with relaxed state, which demonstrates the outstanding mechanical flexibility of the synaptic transistor and it may enable the potential application of the sensory-memory system in wearable electronics.
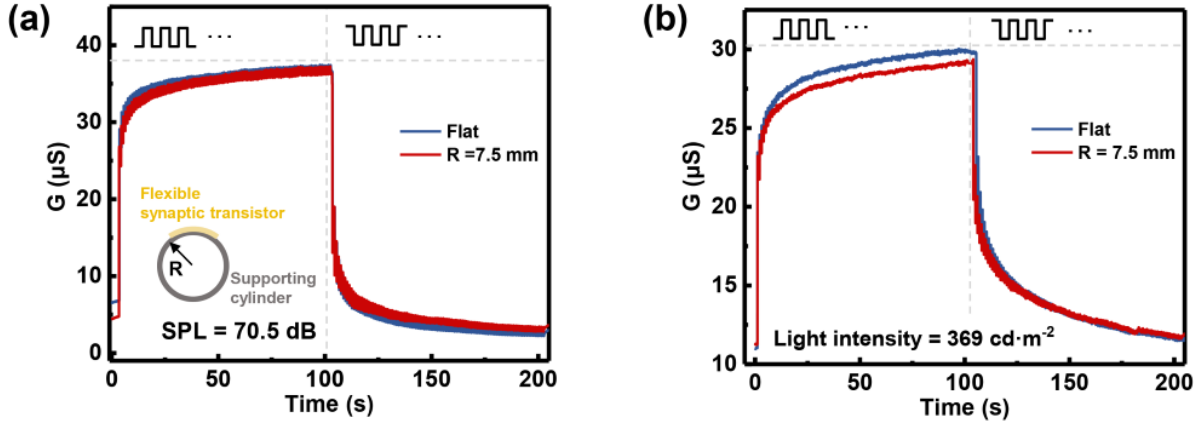
Figure 5.9: Conductance modulation curves of flexible sSWCNT synaptic transistors measured under relaxed state and bent state (curvature radius: 7.5 mm) with (a) periodical auditory stimuli. Inset: schematic illustration of flexibility test setup. (b) periodical visual stimuli.

5.4 Psychological Model Implementation

Beyond purely emulating the biological sensory and synaptic behaviors, the artificial neurological sensory-memory system may also be useful in implementing psychological models related to the human memory and learning process and behavior

5.4.1   Implementation of "Atkinson-Shiffrin model"

The multi-store model (Atkinson-Shiffrin model) is an explanation of human memory proposed by Atkinson and Shiffrin in 1968.[134] As shown in Figure 5.10a, human memory is considered to be composed of information being stored in three separate memory stages. The information detected by the sensory receptors firstly enters the sensory register to be stored for a very short period of time, then if attention is paid, the information in sensory register will be transferred to short-term memory (STM) for temporary memory storage, which typically has a duration of a few seconds. Through an elaborative rehearsal of the input information, the STM can be further transferred into a more long-live memory called long-term memory (LTM), and the probability of this STM-LTM conversion can be positively linked to the number of rehearsal repetitions.[135]

In the artificial neurological sensory-memory system, the loss of the memory (or the event of "forgetting") is defined as the decaying of the conductance below a certain threshold. The time span between the end of the input stimulus and the "forgetting" point is defined as the memory time (Δt_{mem}) and is going to be used to indicate the retention ability of the memory thus to differentiate the STM and LTM. Figure 5.10b illustrates the conductance change of the synaptic transistor in response to 20, 50, and 100 visual potentiation pulses, respectively, where the light intensity, pulse width and period are set as 469 cd·m^{-2}, 10 ms and 1 s, for all three pulse sequences. A conductance of 75 μS is set as the "forgetting" threshold. For memory formed with 20 visual stimulation pulses, the conductance decays below the threshold within just a few seconds, yields a $\Delta t_{mem} = 3.35$ s, which can be classified as the STM. In contrast, for memory with 50 stimulation pulses, which corresponds to an increase in repetition of the rehearsal of the stimulus, the Δt_{mem} increases significantly to 83.4 s. For 100 pulses of stimulation, $\Delta t_{mem} > 100$ s is achieved, which can be regarded as LTM. Apart
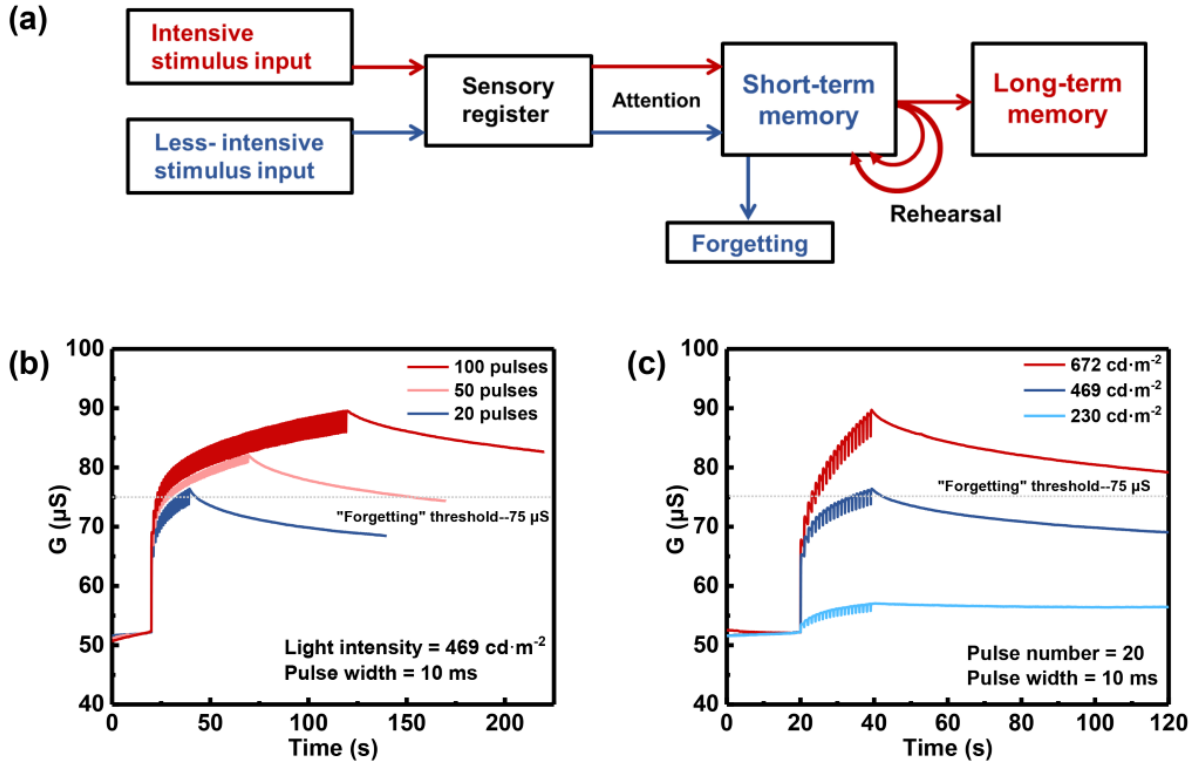
Figure 5.10: Electronic implementation of the multi-store model- "Atkinson-Shiffrin model" of human memory by the neurological sensory-memory system. (a) The psychological model proposed by Atkinson and Shiffrin illustrating the short-term memory (STM) to long-term memory (LTM) transition in human brain. (b) Illustration of imitating STM to LTM transition through rehearsal by repeated visual stimuli. (c) Illustration of promoting STM to LTM transition through increased intensity of visual stimuli.

from the study of STM to LTM conversion through rehearsal, we also studied the effect of the stimulation intensity on this conversion. Figure 5.10c shows the conductance change of the synaptic transistor in response to 20 visual potentiation pulses with various light intensity of 672 cd·m^{-2}, 469 cd·m^{-2}, and 230 cd·m^{-2}, respectively. For the same conductance threshold of 75 μS, LTM with $\Delta t_{mem} > 80$ s is obtained with 672 cd·m^{-2} light stimuli, while STM with $\Delta t_{mem} = 3.35$ s is obtained with 469 cd·m^{-2} light stimuli. For low intensity stimulation with 230 cd·m^{-2}, the conductance fails to reach the threshold, leads to essentially $\Delta t_{mem} = 0$. In Atkinson-Shiffrin model, information can only be transferred to the STM when sufficient attention is given to it, otherwise it is forgotten. Therefore, stimulation with greater intensity

facilitates the process of sensory register to STM transition by increasing the attention level, subsequently enhances the information retention time in short-term memory and finally results in the increasing of the probability of STM to LTM transformation.

5.4.2 Implementation of "Pavlov's dog's experiment"

The classical conditioning, represented by the experiment famously known as "Pavlov's dog's experiment", is illustrated in Figure 5.11a. The experiment describes an associative learning process in biological brain, which occurs when a neutral/conditioned stimulus is accompanied with an unconditioned stimulus. The unconditioned stimulus to an animal is usually physiologic and innate (*e.g.* the appearance of the food), and it will trigger an unconditioned response (*e.g.* salivation) without the necessity of learning. The conditioned stimulus, on the other hand, is a neutral stimulus (*e.g.* the sound of a ringing bell) in the first place. When the neutral stimulus is coupled with the unconditioned stimulus and after the neutral-unconditioned stimuli pair is repeated, the neutral stimulus alone can elicit response, which is called conditioned response, and the neutral stimulus is thus transformed into conditioned stimulus. In contrast to the rise of unconditioned response to unconditioned stimulus, the acquirement of conditioned response requires associative learning. In the Pavlov's dog's experiment, the unconditioned stimulus is represented by the appearance of the food (mainly visual stimulus), which will then cause the dog to salivate even without any training. The sound from a ringing bell (mainly auditory stimulus) is initially considered as a neutral stimulus since it does not elicit salivation in the first place. During conditioning process, the food is repeatedly presented to the dog after the ringing of a bell. After the conditioning process, the sound of the bell is converted to conditioned stimulus and the dog have learned to salivate even when it only hears the sound from a bell. The successful activating of the conditioned response suggests that an association has been

successfully built between the conditioned stimulus and unconditional stimulus in the animal brain by learning. The artificial sensory-memory system provides a biomimicking approach to closely emulate the conditioning processes in Pavlov's dog's experiment. Thanks to the ability of the multimodal physical signal detection and processing, the visual V_{pre} can be treated as the dog's neuron-level sensory unconditioned response of the appearance of the "food", which is regarded as the unconditioned stimulus, whereas the auditory V_{pre} can be treated as neuron-level sensory conditioned response of the "ringing bell", which transits from neutral stimulus to conditioned stimulus after conditioning. The artificial synaptic transistor is considered as the synapse in the dog's brain and will convert the sensory responses to synaptic responses. As illustrated in Figure 5.11b, a visual V_{pre} sequence comprising 10 pulses with a pulse amplitude of 5 V, a pulse width of 10 ms and a period of 100 ms, is designed to be the sensory responses of unconditioned stimuli, while an auditory V_{pre} sequence comprising 10 pulses with a pulse amplitude of 2.5 V, a pulse width of 10 ms and a period of 100 ms is designed to be the sensory responses of neutral/conditioned stimuli. During one training cycle, the visual V_{pre} and auditory V_{pre} in the sequence are applied alternately with an interval of 50 ms. The experimental results of the actual presynaptic pulses induced by visual and auditory stimuli are shown in the bottom panel of Figure 5.11b and they exhibit close resemblance with the designed ones, indicating a successful realization of designed V_{pre} in the artificial sensory-memory system. Figure 5.11c shows the comprehensive process of emulating the Pavlov's dog's experiment in the artificial sensory-memory system in response to actual physical stimuli. In the experiment, the "salivation" threshold is defined as a channel conductance of 54 μS. When the channel conductance reaches above this threshold, the dog is assumed to obtain the ability to salivate to the input stimuli. Before training, the neutral stimuli (auditory stimuli) result in small conductance responses that fall below the threshold, whereas the unconditioned stimuli (visual stimuli) induce significant conductance responses that exceed the salivation threshold ("Before training" phase in Figure 5.11c). During the

training process, a total of 6 cycles of training sequences are applied, and the conductance responses profile suggests that an association of the neutral stimuli and unconditioned stimuli is being established. A detailed view of the conductance responses profile during the third training cycle is shown in the inset of the "Training" phase plot. After training is completed, due to the synaptic memory which the transistor acquired during the training process, the synaptic transistor can reach above the "salivation" threshold when the auditory stimuli are given alone without the existence of visual stimuli. This phenomenon suggests that correlation of the neutral stimuli and unconditioned stimuli has been built which leads to the transition of the neutral stimuli to the conditioned stimuli by successfully triggering the conditioned responses. It is also worth noting that the conditioned responses are less permanent than unconditioned responses. In the "After training" phase, the conditioned conductance responses induced by conditioned (auditory) stimuli gradually decay over an extended period of time and eventually drop below the "salivation" threshold after 21 hr, which indicate that the conditioned stimuli have transited back to neutral stimuli. This can be understood as the conditioned response and the neutral stimulus-conditioned stimulus conversion and association are obtained by learning and memory, and the memory can fade over time if it is not rehearsed according to the Atkinson-Shiffrin model. However, the neutral stimulus-conditioned stimulus association can always be rebuilt, or even strengthened, by additional retraining.
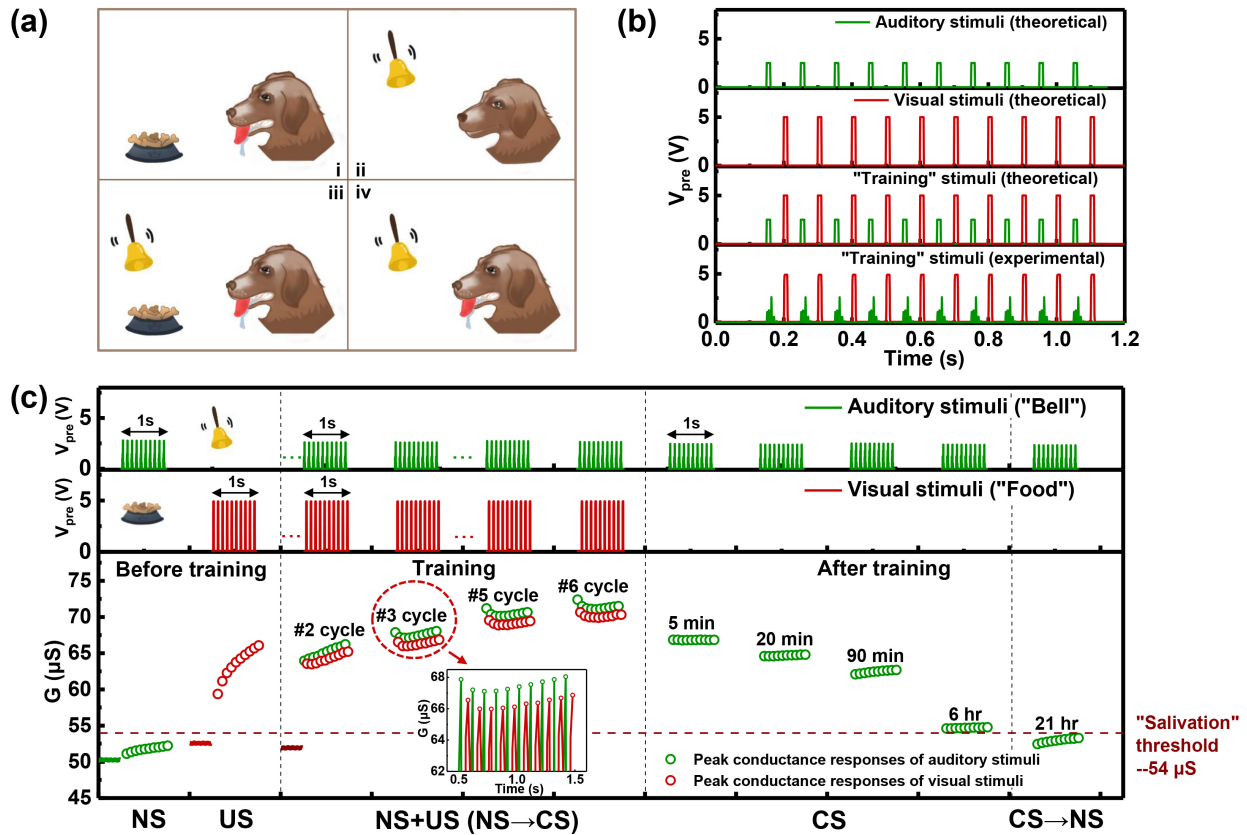
Figure 5.11: Electronic implementation of the classical conditioning experiment- "Pavlov's dog's experiment" by the multimodal neurological sensory-memory system. (a) Schematic illustration of practical Pavlov's dog's experiment. (b) Theoretical and experimental visual and auditory pre-synaptic pulses that are applied to the synaptic transistor to simulate the sensory responses of auditory stimuli ("bell" signals) and visual stimuli ("food" signals) in biological Pavlov's dog's experiment. (c) Complete associative learning simulation with profiles of sensory responses of visual stimuli (unconditioned stimuli, US) and auditory stimuli (neutral/conditioned stimuli, NS/CS) and the corresponding synaptic transistor's channel conductance responses profile. Inset: detailed view of the channel conductance responses profile during the 3rd training cycle.

5.5 Summary

In summary, we have presented a multimodal artificial sensory-memory system (neurological sensory E-skin) that possesses the bio-mimicking sensory transduction and neurological, synapse-like information processing and memorizing capabilities. Successful transduction of visual, auditory and tactile stimuli into pulsed, information-containing electrical pre-synaptic pulses has been achieved through sensors such as phototransistor and FENG in acoustic sensor mode and force sensor mode. The synaptic plasticity of the flexible sSWCNT artificial synaptic transistor has been studied by inducing single-pulse plasticity and long-term plasticity with single and sequence of pre-synaptic pulses included by actual physical stimuli. The synapse-like processing and memory behavior, tunable long-term synaptic plasticity profile and cycle-to-cycle modulation stability have all been demonstrated. Empowered by this artificial sensory-memory system, electronic analogues of two famous psychological models and experiments of brain memory and learning are implemented. The "multi-store model" shows the STM to LTM transition with increased light-stimuli rehearsal and intensity. A bio-plausible classical conditioning experiment- "Pavlov's dog's experiment", is also successfully implemented by integrating actual visual stimuli (physical representation of the image of "food") and actual auditory stimuli (physical representation of the sound of "bell") in the synaptic transistor to enable the imitation of associative learning behavior. The multimodal artificial sensory-memory system demonstrated in this study can potentially widen the application scenario of the artificial intelligence by introducing environment-interactive functions and may also find applications in the fields such as cyborg systems and neuroprosthetics.

Chapter 6

Summary and Future Works

6.1 Summary

In this thesis, we have demonstrated our research on design, fabrication, characterization and integration of novel flexible electronic devices, such as transistors and sensors, to realize biomimetic E-skin with neurological and multiple sensing functions.

Among the many novel active sensors and energy devices being explored for E-skin, the polypropylene-base FENG has caught the eyes due to its small thickness, flexibility and large electromechanical transformation efficiency. It has been predicted as the suitable candidate for self-powered, multifuncational mechancial sensors and has been successfully implemented later in the neurological E-skin research. TENG made from intrinsically stretchable materials also has a great potential to meet requirements of being both soft and efficient. We have presented a lithography-free and low-cost TENG device comprising a porous-structured PDMS layer and a stretchable PEDOT:PSS electrode. The porous PDMS structure is formed by using self-assembled polystyrene beads as the sacrificial template and it is highly ordered

with great uniformity and high structural stability under compression force. Moreover, the porous PDMS TENG has exhibited improved output voltage and current of 1.65 V and 0.54 nA compared to its counterpart with non-porous PDMS with 0.66 V and 0.34 nA. The effect of different loading force and frequency on the output response of the TENG device has also been studied. This work could shed light on diverse structural modification methods for improving the performance of PDMS-based TENG and the development of intrinsically stretchable TENG for wearable device applications.

Semiconducting single-wall carbon nanotubes (sSWCNTs) have been widely used as the channel material for high-performance printed flexible thin-film transistors (TFTs). We have studied the microfabricated sSWCNTs TFTs on polyimide substrate and the experimental results have shown that the TFTs are suitable for sensor control in active matrix backplane and for neuromorphic applications. Then, we have demonstrated fully printed dual-gate sSWCNT TFTs that exhibit almost symmetric ambipolar characteristics. With the applied control gate voltage varying from -60 to +60 V, a threshold voltage tuning range of 27 V has been achieved, allowing the device to be effectively tuned into either predominantly p-type or predominantly n-type. The tunable ambipolar characteristics are found to be very stable over a long period of time (4 months). By integrating two printed dual-gate TFTs biased with different control gate voltages, a complementary metal oxide semiconductor inverter with close to rail-to-rail output voltage swing has been demonstrated. The use of a dual-gate structure for achieving n-type printed carbon nanotube TFTs is much more controllable and repeatable compared to other methods such as chemical doping. Our work have shown the feasibility of implementing more sophisticated complementary logic circuits using printed flexible carbon nanotube transistors.

While there have already been many reports on artificial synaptic transistors implemented on rigid substrates, the use of flexible devices could potentially enable an even broader range of

applications. In this work, we have reported artificial synaptic TFTs built on an ultrathin flexible substrate using high carrier mobility sSWCNTs. The synaptic characteristics of the flexible synaptic transistor including short-term/memory plasticity, spike-amplitude-dependent plasticity, spike-width-dependent plasticity, paired-pulse facilitation, and spike-time-dependent plasticity have all been systematically characterized. Furthermore, we have demonstrated a flexible force-sensing neurological electronic skin and its peripheral nerve with a FENG serving as the sensory mechanoreceptor that generates action potentials to be processed and transmitted by the artificial synapse. In such force-sensing neurological electronic skin, the flexible FENG sensor converts the tactile input (magnitude and frequency of force) into presynaptic action potential pulses, which are then passed to the gate of the synaptic transistor to induce change in its postsynaptic current, mimicking the modulation of synaptic weight in a biological synapse. The demonstrated prototype force-sensing neurological electronic skin closely imitates the behavior of actual human skin, and it allows for instantaneous detection of force stimuli and offers biological synapse-like behavior to relay the stimulus signals to the next stage. The flexible sensory skin could potentially be used to interface with skeletal muscle fibers for applications in neuroprosthetic devices.

Finally, the aforementioned prototype force-sensing neurological electronic skin has been expanded to a multimodal artificial sensory-memory system consists of photosensor, FENG-based mechanical sensors and flexible carbon nanotube synaptic transistor that possesses biomimetic visual, auditory and tactile sensing capabilities and synapse-like signal processing and memorizing behaviors. The transduction of physical signals into information-containing, pre-synaptic action potentials and the synaptic plasticity of the transistor in response to single and long-term action potential excitations have been systematically characterized, and the bioreceptor-like sensing and synapse-like memorizing behaviors have been demonstrated.

Based on the memory and learning characteristics of the sensory-memory system, the well-known psychological model describing human memory- "multi-store memory" model and the classical conditioning experiment that demonstrates the associative learning of brain- "Pavlov's dog's experiment", have both been electronically implemented using external physical signals as the sources of the stimulus. The biomimetic intelligence demonstrated in this neurological sensory-memory system shows potential in promoting the advancement in multi-modal, user-environment interactive AI.

6.2 Outlook

Based on the results achieved so far, several potential research related to the device-level and system-level studies of neurological E-skin may be carried out for the next step. And they are listed as follows:

6.2.1 Fully-Printed Stretchable Synaptic Transistor

One of the prominent characterization of natural human skin is its mechanical compliance. The mechanically stretchability of skin allows it to conformally covers movable body parts like joints and endure motion-related stress and strain without incurring physical damage. Therefore, for potential applications in wearable neurological E-skin or skin-based diagnostic platforms, it is desirable to fabricate stretchable electronic devices on soft elastic substrates rather than flexible polymer substrate to achieve the full mechanical robustness of human skin. Stretchable synaptic transistor, due to its complex structure and functions, can be regarded as a benchmark for the development of stretchable electronic devices for E-skin applications. The previous study from our group have successfully demonstrated stretchable

sSWCNT TFTs using all intrinsically stretchable materials and all printing process,[28] as shown in Figure 6.1a and b.

Figure 6.1c shows the intrinsically stretchable TFTs can withstand tensile strain up to 50% in both channel length and width direction, and incur only minimal changes in device performance. Similar techniques of this study can be adopted to build stretchable synaptic transistors. For the next step of our research, we may try to substitute the stretchable dielectric layer from $BaTiO_3$/PDMS composite to elastic dielectric materials with EDL effect[52, 110] to introduce the synaptic functions into the stretchable transistor. The fully printed, stretchable synaptic sSWCNT TFTs may pave way for low-cost, large area, soft wearable bioelectronics and soft machines.

6.2.2   Synaptic Transistor with Chemical Sensing Modality

In this thesis, the demonstrated sensing modalities (visual, auditory and tactile) of the neurological E-skin are primarily physical. In Chapter 1, however, we have also developed interests in the chemical sensing modalities, such as sweat chemicals sensing and gas sensing, which may be one of the directions of our next step of research. The chemical sensing modalities are critical for realizing the diagnostic and health-monitoring functions and can potentially be incorporated into the sensory system of the neurological E-skin. This can be achieved by sSWCNT transistor-based chemical/biological sensors (Figure 6.2a) while the sSWCNT itself have been studied majorly as channel material of conventional or synaptic flexible TFTs in our previous study. It is known that the electrical properties of the sSWCNT largely depends on the its physical properties.[137] Through physisorption and molecular interaction with gas and/or protein molecules, the sSWCNT would undergo drastic charge environment change, thus leads to significant change in channel conductance and the detection of chemical signals,[136] as presented in Figure 6.2b. By further functionalizing the
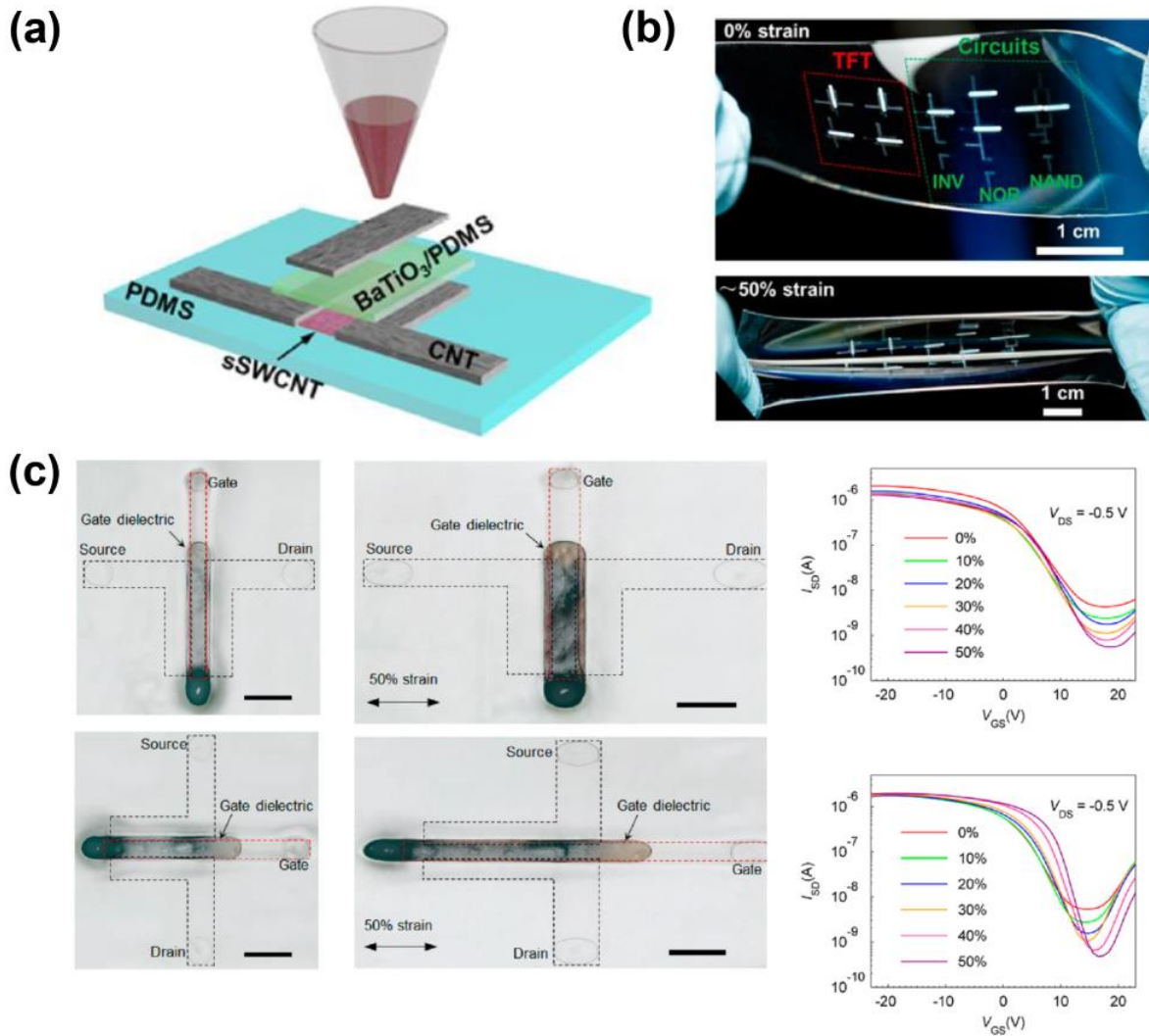
Figure 6.1: Fully printed and intrinsically stretchable CNT TFTs. (a) Schematic illustration of printing method and the structure of a printed TFT. (b) Photographs of the printed stretchable TFTs and logic circuit at relaxed state (top) and under tensile strain of $\sim 50\%$ (bottom). (c) Photographs and transfer curves (I_{DS}-V_{GS}) of the printed stretchable TFT under the stretching test up to 50% tensile strain along the channel length direction (top) and channel width direction (bottom). Reprinted from Ref.[28].

114
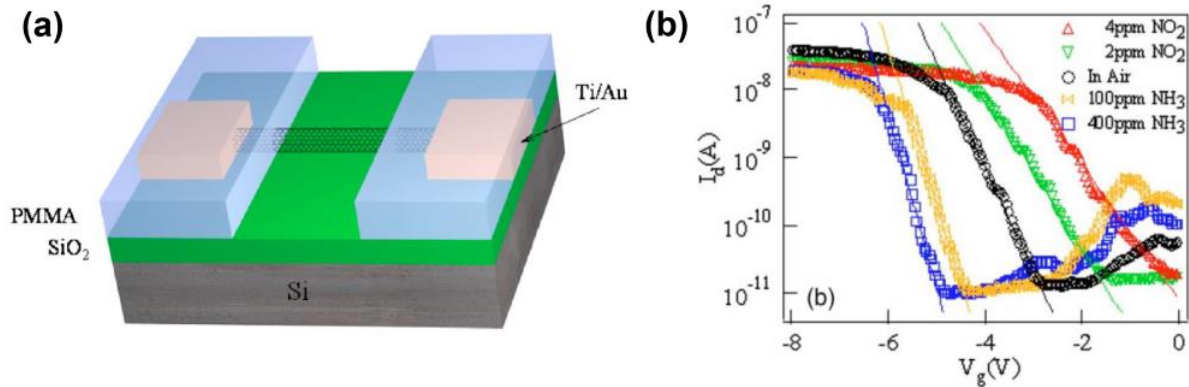
Figure 6.2: sSWCNT transistor-based chemical/biological sensors. (a) Schematic illustration of a center-exposed sSWCNT transistor-based gas sensor. (b) Transfer curve shift in response to different ambient conditions. Reprinted from Ref.[136].

surface of sSWCNT with specified chemical/biological receptors, specific detection of glucose, carbohydrate, antibody or even DNA can be enabled.[138, 139, 140, 141] Another advantage of using sSWCNT transistor-based biosensors is the potential fabrication feasibility. The sSWCNT sensors will share most of the fabrication processes with the sSWCNT synaptic transistor and can be fabricated and integrated monolithically with the synaptic transistor, which might considerably reduce the manufacturing cost and increase the integration density.

6.2.3 Neurological E-skin for Motion Control

The human interactions with the world require not only perceptual abilities from sensory organs and nervous systems, but the also the motor functions such as waving a hand to react to the external stimulus. Lee *et al.* presented an artificial optoelectronic sensorimotor system in Figure 6.3a by combining a photodetector, a synaptic transistor and a polymer actuator.[132] The optical stimuli were first transduced into electrical pulses and processed as synaptic responses of the synaptic transistor, as shown in Figure 6.3b. The output signals from the synaptic transistor were then converted to voltage signals to activate the movement
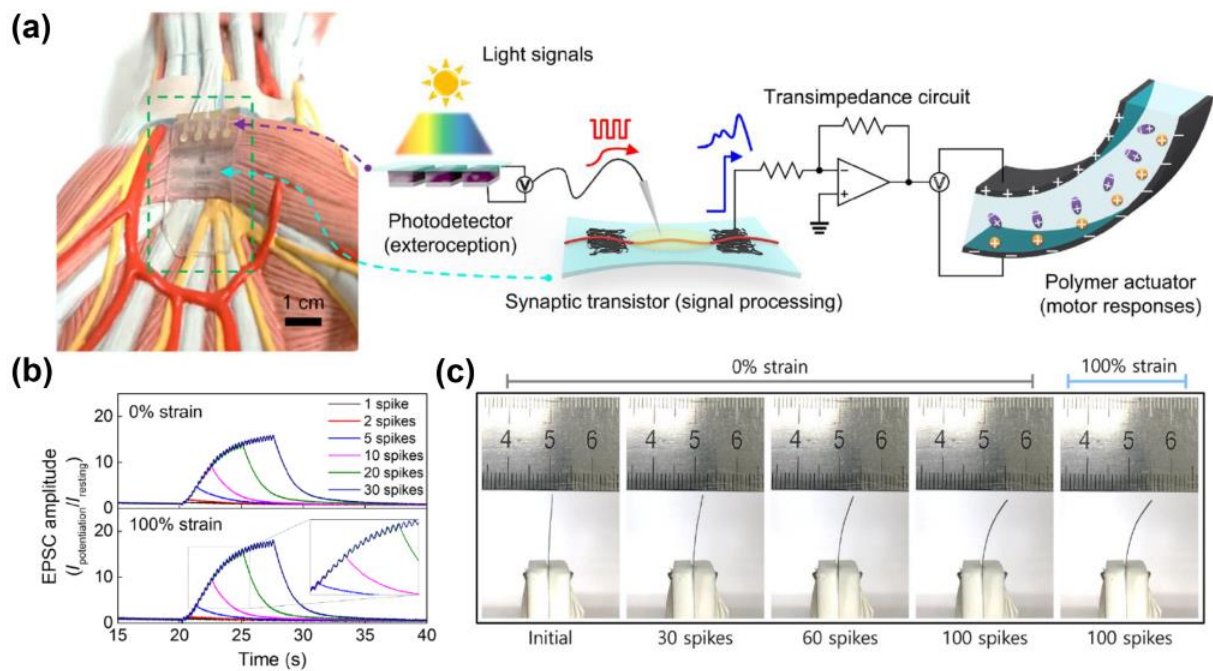
Figure 6.3: (a) Schematics illustrating the artificial optoelectronic sensorimotor system and the flow of signals. (b) Light-triggered synaptic responses (EPSC) of the stretchable synaptic transistor by 1 to 30 spikes with 0 (top) or 100% (bottom) tensile strain. (c) Photographs of the polymer actuator activated by different number of spikes (0 to 100) with 0 or 100% tensile strain. Reprinted from Ref.[132].

of the polymer actuator. Inspired by this optoelectronic sensorimotor system, in this thesis, we have demonstrated the multimodal sensory-memory system, the next step of the research can consequentially focus on interfacing the sensory-memory system with the artificial motor units to realize the sensorimotor system that can response to multiple types of input stimuli. Due to the synapse-like memory effect of the sSWCNT synaptic transistor, the actuation of the motor unit is expected to be maintained even after the external stimuli are gone. For soft robotics or neuromuscle applications, constructing such a multifunctional artificial sensorimotor system consists of sensory, memory and motor components may be a significant step toward faithfully mimicking the actual human behaviors in machines.

117

References

[1] Alex Chortos, Jia Liu, and Zhenan Bao. "Pursuing prosthetic electronic skin." *Nature materials* 15.9 (2016), pp. 937–950.

[2] Ian Darian-Smith, KO Johnson, C LaMotte, Y Shigenaga, P Kenins, and P Champness. "Warm fibers innervating palmar and digital skin of the monkey: responses to thermal stimuli." *Journal of neurophysiology* 42.5 (1979), pp. 1297–1315.

[3] Harvey Lodish, Arnold Berk, S Lawrence Zipursky, Paul Matsudaira, David Baltimore, and James Darnell. "Neurotransmitters, synapses, and impulse transmission." *Molecular Cell Biology. 4th edition.* WH Freeman, 2000.

[4] Guo-qiang Bi and Mu-ming Poo. "Distributed synaptic modification in neural networks induced by patterned stimulation." *Nature* 401.6755 (1999), pp. 792–796.

[5] Yuhao Liu, Matt Pharr, and Giovanni Antonio Salvatore. "Lab-on-skin: a review of flexible and stretchable electronics for wearable health monitoring." *ACS nano* 11.10 (2017), pp. 9614–9635.

[6] Jason Heikenfeld, Andrew Jajack, Benjamin Feldman, Steve W Granger, Supriya Gaitonde, Gavi Begtrup, and Benjamin A Katchman. "Accessing analytes in biofluids for peripheral biochemical monitoring." *Nature biotechnology* 37.4 (2019), pp. 407–419.

[7] Fuqin Sun, Qifeng Lu, Simin Feng, and Ting Zhang. "Flexible Artificial Sensory Systems Based on Neuromorphic Devices." *ACS nano* 15.3 (2021), pp. 3875–3899.

[8] Kuniharu Takei, Toshitake Takahashi, Johnny C Ho, Hyunhyub Ko, Andrew G Gillies, Paul W Leu, Ronald S Fearing, and Ali Javey. "Nanowire active-matrix circuitry for low-voltage macroscale artificial skin." *Nature materials* 9.10 (2010), pp. 821–826.

[9] Hongyang Shi, Mohammed Al-Rubaiai, Christopher M Holbrook, Jinshui Miao, Thassyo Pinto, Chuan Wang, and Xiaobo Tan. "Screen-Printed Soft Capacitive Sensors for Spatial Mapping of Both Positive and Negative Pressures." *Advanced Functional Materials* 29.23 (2019), p. 1809116.

[10] Feng Ru Fan, Wei Tang, and Zhong Lin Wang. "Flexible nanogenerators for energy harvesting and self-powered electronics." *Advanced Materials* 28.22 (2016), pp. 4283–4305.

[11]   Yunqi Cao, José Figueroa, Wei Li, Zhiqiang Chen, Zhong Lin Wang, and Nelson Sepúlveda. "Understanding the dynamic response in ferroelectret nanogenerators to enable self-powered tactile systems and human-controlled micro-robots." *Nano Energy* 63 (2019), p. 103852.

[12]   Guang Zhu, Caofeng Pan, Wenxi Guo, Chih-Yen Chen, Yusheng Zhou, Ruomeng Yu, and Zhong Lin Wang. "Triboelectric-generator-driven pulse electrodeposition for micropatterning." *Nano letters* 12.9 (2012), pp. 4960–4965.

[13]   Dae-Hyeong Kim, Nanshu Lu, Roozbeh Ghaffari, Yun-Soung Kim, Stephen P Lee, Lizhi Xu, Jian Wu, Rak-Hwan Kim, Jizhou Song, Zhuangjian Liu, et al. "Materials for multifunctional balloon catheters with capabilities in cardiac electrophysiological mapping and ablation therapy." *Nature materials* 10.4 (2011), pp. 316–323.

[14]   Mallory L Hammock, Alex Chortos, Benjamin C-K Tee, Jeffrey B-H Tok, and Zhenan Bao. "25th anniversary article: the evolution of electronic skin (e-skin): a brief history, design considerations, and recent progress." *Advanced materials* 25.42 (2013), pp. 5997–6038.

[15]   Takao Someya, Yusaku Kato, Tsuyoshi Sekitani, Shingo Iba, Yoshiaki Noguchi, Yousuke Murase, Hiroshi Kawaguchi, and Takayasu Sakurai. "Conformable, flexible, large-area networks of pressure and thermal sensors with organic transistor active matrixes." *Proceedings of the National Academy of Sciences* 102.35 (2005), pp. 12321–12325.

[16]   Jaemin Kim, Mincheol Lee, Hyung Joon Shim, Roozbeh Ghaffari, Hye Rim Cho, Donghee Son, Yei Hwan Jung, Min Soh, Changsoon Choi, Sungmook Jung, et al. "Stretchable silicon nanoribbon electronics for skin prosthesis." *Nature communications* 5.1 (2014), pp. 1–11.

[17]   Wei Gao, Sam Emaminejad, Hnin Yin Yin Nyein, Samyuktha Challa, Kevin Chen, Austin Peck, Hossain M Fahad, Hiroki Ota, Hiroshi Shiraki, Daisuke Kiriya, et al. "Fully integrated wearable sensor arrays for multiplexed in situ perspiration analysis." *Nature* 529.7587 (2016), pp. 509–514.

[18]   Tomoyuki Yokota, Peter Zalar, Martin Kaltenbrunner, Hiroaki Jinno, Naoji Matsuhisa, Hiroki Kitanosako, Yutaro Tachibana, Wakako Yukita, Mari Koizumi, and Takao Someya. "Ultraflexible organic photonic skin." *Science advances* 2.4 (2016), e1501856.

[19]   Toshiyo Tamura, Yuka Maeda, Masaki Sekine, and Masaki Yoshida. "Wearable photoplethysmographic sensors—past and present." *Electronics* 3.2 (2014), pp. 282–302.

[20]   Adam T Zocco. "Pentacene-based Organic Thin-film Transistors on Paper." PhD thesis. University of Cincinnati, 2013.

[21]   Kwon-Shik Park, Saeroonter Oh, Pilsang Yun, Jong Uk Bae, and In Byeong Kang. "Prospects of oxide TFTs approaching LTPS." *2015 22nd International Workshop on Active-Matrix Flatpanel Displays and Devices (AM-FPD)*. IEEE. 2015, pp. 241–244.

[22] Dongseob Ji, Jisu Jang, Joon Hui Park, Dasol Kim, You Seung Rim, Do Kyung Hwang, and Yong-Young Noh. "Recent progress in the development of backplane thin film transistors for information displays." *Journal of Information Display* 22.1 (2021), pp. 1–11.

[23] Guohua Hu, Tom Albrow-Owen, Xinxin Jin, Ayaz Ali, Yuwei Hu, Richard CT Howe, Khurram Shehzad, Zongyin Yang, Xuekun Zhu, Robert I Woodward, et al. "Black phosphorus ink formulation for inkjet printing of optoelectronics and photonics." *Nature communications* 8.1 (2017), pp. 1–10.

[24] Daryl McManus, Sandra Vranic, Freddie Withers, Veronica Sanchez-Romaguera, Massimo Macucci, Huafeng Yang, Roberto Sorrentino, Khaled Parvez, Seok-Kyun Son, Giuseppe Iannaccone, et al. "Water-based and biocompatible 2D crystal inks for all-inkjet-printed heterostructures." *Nature nanotechnology* 12.4 (2017), pp. 343–350.

[25] He Yan, Zhihua Chen, Yan Zheng, Christopher Newman, Jordan R Quinn, Florian Dötz, Marcel Kastler, and Antonio Facchetti. "A high-mobility electron-transporting polymer for printed transistors." *Nature* 457.7230 (2009), pp. 679–686.

[26] Hiromi Minemawari, Toshikazu Yamada, Hiroyuki Matsui, Jun'ya Tsutsumi, Simon Haas, Ryosuke Chiba, Reiji Kumai, and Tatsuo Hasegawa. "Inkjet printing of single-crystal films." *Nature* 475.7356 (2011), pp. 364–367.

[27] Le Cai, Suoming Zhang, Jinshui Miao, Zhibin Yu, and Chuan Wang. "Fully printed foldable integrated logic gates with tunable performance using semiconducting carbon nanotubes." *Advanced Functional Materials* 25.35 (2015), pp. 5698–5705.

[28] Le Cai, Suoming Zhang, Jinshui Miao, Zhibin Yu, and Chuan Wang. "Fully printed stretchable thin-film transistors and integrated logic circuits." *Acs Nano* 10.12 (2016), pp. 11459–11468.

[29] Pattaramon Vuttipittayamongkol, Fanqi Wu, Haitian Chen, Xuan Cao, Bilu Liu, and Chongwu Zhou. "Threshold voltage tuning and printed complementary transistors and inverters based on thin films of carbon nanotubes and indium zinc oxide." *Nano Research* 8.4 (2015), pp. 1159–1168.

[30] Ali Javey, Jing Guo, Qian Wang, Mark Lundstrom, and Hongjie Dai. "Ballistic carbon nanotube field-effect transistors." *nature* 424.6949 (2003), pp. 654–657.

[31] Qing Cao, Hoon-sik Kim, Ninad Pimparkar, Jaydeep P Kulkarni, Congjun Wang, Moonsub Shim, Kaushik Roy, Muhammad A Alam, and John A Rogers. "Medium-scale carbon nanotube thin-film integrated circuits on flexible plastic substrates." *Nature* 454.7203 (2008), pp. 495–500.

[32] Chuan Wang, Kuniharu Takei, Toshitake Takahashi, and Ali Javey. "Carbon nanotube electronics–moving forward." *Chemical Society Reviews* 42.7 (2013), pp. 2592–2609.

[33] Chuan Wang, Jun-Chau Chien, Kuniharu Takei, Toshitake Takahashi, Junghyo Nah, Ali M Niknejad, and Ali Javey. "Extremely bendable, high-performance integrated circuits using semiconducting carbon nanotube networks for digital, analog, and radio-frequency applications." *Nano letters* 12.3 (2012), pp. 1527–1533.

[34] Haitian Chen, Yu Cao, Jialu Zhang, and Chongwu Zhou. "Large-scale complementary macroelectronics using hybrid integration of carbon nanotubes and IGZO thin-film transistors." *Nature communications* 5.1 (2014), pp. 1–12.

[35] Kuniharu Takei, Wei Gao, Chuan Wang, and Ali Javey. "Physical and chemical sensing with electronic skin." *Proceedings of the IEEE* 107.10 (2019), pp. 2155–2167.

[36] Pak Heng Lau, Kuniharu Takei, Chuan Wang, Yeonkyeong Ju, Junseok Kim, Zhibin Yu, Toshitake Takahashi, Gyoujin Cho, and Ali Javey. "Fully printed, high performance carbon nanotube thin-film transistors on flexible substrates." *Nano letters* 13.8 (2013), pp. 3864–3869.

[37] Xuan Cao, Haitian Chen, Xiaofei Gu, Bilu Liu, Wenli Wang, Yu Cao, Fanqi Wu, and Chongwu Zhou. "Screen printing as a scalable and low-cost approach for rigid and flexible thin-film transistors using separated carbon nanotubes." *ACS nano* 8.12 (2014), pp. 12769–12776.

[38] Mingjing Ha, Yu Xia, Alexander A Green, Wei Zhang, Mike J Renn, Chris H Kim, Mark C Hersam, and C Daniel Frisbie. "Printed, sub-3V digital circuits on plastic from aqueous carbon nanotube inks." *ACS nano* 4.8 (2010), pp. 4388–4395.

[39] Leon Chua. "Memristor-the missing circuit element." *IEEE Transactions on circuit theory* 18.5 (1971), pp. 507–519.

[40] Dmitri B Strukov, Gregory S Snider, Duncan R Stewart, and R Stanley Williams. "The missing memristor found." *nature* 453.7191 (2008), pp. 80–83.

[41] Sung Hyun Jo, Ting Chang, Idongesit Ebong, Bhavitavya B Bhadviya, Pinaki Mazumder, and Wei Lu. "Nanoscale memristor device as synapse in neuromorphic systems." *Nano letters* 10.4 (2010), pp. 1297–1301.

[42] Sungho Kim, Jinsu Yoon, Hee-Dong Kim, and Sung-Jin Choi. "Carbon nanotube synaptic transistor network for pattern recognition." *ACS applied materials & interfaces* 7.45 (2015), pp. 25479–25486.

[43] Ivan Sanchez Esqueda, Xiaodong Yan, Chris Rutherglen, Alex Kane, Tyler Cain, Phil Marsh, Qingzhou Liu, Kosmas Galatsis, Han Wang, and Chongwu Zhou. "Aligned carbon nanotube synaptic transistors for large-scale neuromorphic computing." *ACS nano* 12.7 (2018), pp. 7352–7361.

[44] Mohammed A Zidan, John Paul Strachan, and Wei D Lu. "The future of electronics based on memristive systems." *Nature electronics* 1.1 (2018), pp. 22–29.

[45] Xuan Cao, Yu Cao, and Chongwu Zhou. "Imperceptible and ultraflexible p-type transistors and macroelectronics based on carbon nanotubes." *ACS nano* 10.1 (2016), pp. 199–206.

[46]   Dong-Ming Sun, Chang Liu, Wen-Cai Ren, and Hui-Ming Cheng. "A review of carbon nanotube-and graphene-based flexible thin-film transistors." *Small* 9.8 (2013), pp. 1188–1205.

[47]   Ping Feng, Weiwei Xu, Yi Yang, Xiang Wan, Yi Shi, Qing Wan, Jianwen Zhao, and Zheng Cui. "Printed Neuromorphic Devices Based on Printed Carbon Nanotube Thin-Film Transistors." *Advanced Functional Materials* 27.5 (2017), p. 1604447.

[48]   Jonathan Rivnay, Sahika Inal, Alberto Salleo, Róisın M Owens, Magnus Berggren, and George G Malliaras. "Organic electrochemical transistors." *Nature Reviews Materials* 3.2 (2018), pp. 1–14.

[49]   Sungho Kim, Bongsik Choi, Meehyun Lim, Jinsu Yoon, Juhee Lee, Hee-Dong Kim, and Sung-Jin Choi. "Pattern recognition using carbon nanotube synaptic transistors with an adjustable weight update protocol." *ACS nano* 11.3 (2017), pp. 2814–2822.

[50]   Adam W Bushmaker, Vanessa Oklejas, Don Walker, Alan R Hopkins, Jihan Chen, and Stephen B Cronin. "Single-ion adsorption and switching in carbon nanotubes." *Nature communications* 7.1 (2016), pp. 1–8.

[51]   Yeongin Kim, Alex Chortos, Wentao Xu, Yuxin Liu, Jin Young Oh, Donghee Son, Jiheong Kang, Amir M Foudeh, Chenxin Zhu, Yeongjun Lee, et al. "A bioinspired flexible organic artificial afferent nerve." *Science* 360.6392 (2018), pp. 998–1003.

[52]   Hyunseok Shim, Kyoseung Sim, Faheem Ershad, Pinyi Yang, Anish Thukral, Zhoulyu Rao, Hae-Jin Kim, Yanghui Liu, Xu Wang, Guoying Gu, et al. "Stretchable elastic synaptic transistors for neurologically integrated soft engineering systems." *Science advances* 5.10 (2019), eaax4961.

[53]   Jinran Yu, Xixi Yang, Guoyun Gao, Yao Xiong, Yifei Wang, Jing Han, Youhui Chen, Huai Zhang, Qijun Sun, and Zhong Lin Wang. "Bioinspired mechano-photonic artificial synapse based on graphene/MoS2 heterostructure." *Science Advances* 7.12 (2021), eabd9117.

[54]   M Glick, Y Benlachtar, and RI Killey. "Performance and power consumption of digital signal processing based transceivers for optical interconnect applications." *2009 11th International Conference on Transparent Optical Networks*. IEEE. 2009, pp. 1–4.

[55]   Alan Bannon, Christopher Peter Hurrell, Derek Hummerston, and Colin Lyden. "An 18 b 5 MS/s SAR ADC with 100.2 dB dynamic range." *2014 Symposium on VLSI Circuits Digest of Technical Papers*. IEEE. 2014, pp. 1–2.

[56]   Thai T Vu, Nguyen Van Huynh, Dinh Thai Hoang, Diep N Nguyen, and Eryk Dutkiewicz. "Offloading energy efficiency with delay constraint for cooperative mobile edge computing networks." *2018 IEEE Global Communications Conference (GLOBECOM)*. IEEE. 2018, pp. 1–6.

[57]   Dapeng Liu, Qianqian Shi, Shilei Dai, and Jia Huang. "The Design of 3D-Interface Architecture in an Ultralow-Power, Electrospun Single-Fiber Synaptic Transistor for Neuromorphic Computing." *Small* 16.13 (2020), p. 1907472.

[58] Ji-Man Yu, Chungryeol Lee, Da-Jin Kim, Hongkeun Park, Joon-Kyu Han, Jae Hur, Jin-Ki Kim, Myung-Su Kim, Myungsoo Seo, Sung Gap Im, et al. "All-Solid-State Ion Synaptic Transistor for Wafer-Scale Integration with Electrolyte of a Nanoscale Thickness." *Advanced Functional Materials* 31.23 (2021), p. 2010971.

[59] Ke He, Yaqing Liu, Ming Wang, Geng Chen, Ying Jiang, Jiancan Yu, Changjin Wan, Dianpeng Qi, Meng Xiao, Wan Ru Leow, et al. "An artificial somatic reflex arc." *Advanced Materials* 32.4 (2020), p. 1905399.

[60] Chuan Wang, David Hwang, Zhibin Yu, Kuniharu Takei, Junwoo Park, Teresa Chen, Biwu Ma, and Ali Javey. "User-interactive electronic skin for instantaneous pressure visualization." *Nature materials* 12.10 (2013), pp. 899–904.

[61] Sri Ganesh R Bade, Xin Shan, Phong Tran Hoang, Junqiang Li, Thomas Geske, Le Cai, Qibing Pei, Chuan Wang, and Zhibin Yu. "Stretchable Light-Emitting Diodes with Organometal-Halide-Perovskite–Polymer Composite Emitters." *Advanced Materials* 29.23 (2017), p. 1607053.

[62] Xuan Cao, Christian Lau, Yihang Liu, Fanqi Wu, Hui Gui, Qingzhou Liu, Yuqiang Ma, Haochuan Wan, Moh R Amer, and Chongwu Zhou. "Fully screen-printed, large-area, and flexible active-matrix electrochromic displays using carbon nanotube thin-film transistors." *ACS nano* 10.11 (2016), pp. 9816–9822.

[63] Le Cai, Suoming Zhang, Yiheng Zhang, Junqiang Li, Jinshui Miao, Qifan Wang, Zhibin Yu, and Chuan Wang. "Direct printing for additive patterning of silver nanowires for stretchable sensor and display applications." *Advanced Materials Technologies* 3.2 (2018), p. 1700232.

[64] Clementine M Boutry, Levent Beker, Yukitoshi Kaizawa, Christopher Vassos, Helen Tran, Allison C Hinckley, Raphael Pfattner, Simiao Niu, Junheng Li, Jean Claverie, et al. "Biodegradable and flexible arterial-pulse sensor for the wireless monitoring of blood flow." *Nature biomedical engineering* 3.1 (2019), pp. 47–57.

[65] Rusen Yang, Yong Qin, Liming Dai, and Zhong Lin Wang. "Power generation with laterally packaged piezoelectric fine wires." *Nature nanotechnology* 4.1 (2009), pp. 34–39.

[66] Wei Li, David Torres, Tongyu Wang, Chuan Wang, and Nelson Sepúlveda. "Flexible and biocompatible polypropylene ferroelectret nanogenerator (FENG): on the path toward wearable devices powered by human motion." *Nano Energy* 30 (2016), pp. 649–657.

[67] Yunqi Cao, José Figueroa, Juan J Pastrana, Wei Li, Zhiqiang Chen, Zhong Lin Wang, and Nelson Sepúlveda. "Flexible ferroelectret polymer for self-powering devices and energy storage systems." *ACS applied materials & interfaces* 11.19 (2019), pp. 17400–17409.

[68] Feng-Ru Fan, Zhong-Qun Tian, and Zhong Lin Wang. "Flexible triboelectric generator." *Nano energy* 1.2 (2012), pp. 328–334.

[69] Zhenhua Luo, Dibin Zhu, Junjie Shi, Steve Beeby, Chunhong Zhang, Plamen Proynov, and Bernard Stark. "Energy harvesting study on single and multilayer ferroelectret foams under compressive force." *IEEE Transactions on Dielectrics and Electrical Insulation* 22.3 (2015), pp. 1360–1368.

[70] Wei Li, David Torres, Ramón Dıaz, Zhengjun Wang, Changsheng Wu, Chuan Wang, Zhong Lin Wang, and Nelson Sepúlveda. "Nanogenerator-based dual-functional and self-powered thin patch loudspeaker or microphone for flexible electronics." *Nature communications* 8.1 (2017), pp. 1–9.

[71] Jie Chen, Hengyu Guo, Xianming He, Guanlin Liu, Yi Xi, Haofei Shi, and Chenguo Hu. "Enhancing performance of triboelectric nanogenerator by filling high dielectric nanoparticles into sponge PDMS film." *ACS applied materials & interfaces* 8.1 (2016), pp. 736–744.

[72] Yanbo Zhu, Bin Yang, Jingquan Liu, Xingzhao Wang, Luxian Wang, Xiang Chen, and Chunsheng Yang. "A flexible and biocompatible triboelectric nanogenerator with tunable internal resistance for powering wearable devices." *Scientific reports* 6.1 (2016), pp. 1–10.

[73] Sihong Wang, Long Lin, and Zhong Lin Wang. "Nanoscale triboelectric-effect-enabled energy conversion for sustainably powering portable electronics." *Nano letters* 12.12 (2012), pp. 6339–6346.

[74] Feng-Ru Fan, Long Lin, Guang Zhu, Wenzhuo Wu, Rui Zhang, and Zhong Lin Wang. "Transparent triboelectric nanogenerators and self-powered pressure sensors based on micropatterned plastic films." *Nano letters* 12.6 (2012), pp. 3109–3114.

[75] Keun Young Lee, Jinsung Chun, Ju-Hyuck Lee, Kyeong Nam Kim, Na-Ri Kang, Ju-Young Kim, Myung Hwa Kim, Kyung-Sik Shin, Manoj Kumar Gupta, Jeong Min Baik, et al. "Hydrophobic sponge structure-based triboelectric nanogenerator." *Advanced materials* 26.29 (2014), pp. 5037–5042.

[76] Yue Wang, Chenxin Zhu, Raphael Pfattner, Hongping Yan, Lihua Jin, Shucheng Chen, Francisco Molina-Lopez, Franziska Lissel, Jia Liu, Noelle I Rabiah, et al. "A highly stretchable, transparent, and conductive polymer." *Science advances* 3.3 (2017), e1602076.

[77] Xianming He, Xiaojing Mu, Quan Wen, Zhiyu Wen, Jun Yang, Chenguo Hu, and Haofei Shi. "Flexible and transparent triboelectric nanogenerator based on high performance well-ordered porous PDMS dielectric film." *Nano Research* 9.12 (2016), pp. 3714–3724.

[78] Xuexian Chen, Liming Miao, Hang Guo, Haotian Chen, Yu Song, Zongming Su, and Haixia Zhang. "Waterproof and stretchable triboelectric nanogenerator for biomechanical energy harvesting and self-powered sensing." *Applied Physics Letters* 112.20 (2018), p. 203902.

[79] Canan Dagdeviren, Byung Duk Yang, Yewang Su, Phat L Tran, Pauline Joe, Eric Anderson, Jing Xia, Vijay Doraiswamy, Behrooz Dehdashti, Xue Feng, et al. "Conformal piezoelectric energy harvesting and storage from motions of the heart, lung, and diaphragm." *Proceedings of the National Academy of Sciences* 111.5 (2014), pp. 1927–1932.

[80] Martin Kaltenbrunner, Tsuyoshi Sekitani, Jonathan Reeder, Tomoyuki Yokota, Kazunori Kuribara, Takeyoshi Tokuhara, Michael Drack, Reinhard Schwödiauer, Ingrid Graz, Simona Bauer-Gogonea, et al. "An ultra-lightweight design for imperceptible plastic electronics." *Nature* 499.7459 (2013), pp. 458–463.

[81] Mingjing Ha, Jung-Woo T Seo, Pradyumna L Prabhumirashi, Wei Zhang, Michael L Geier, Michael J Renn, Chris H Kim, Mark C Hersam, and C Daniel Frisbie. "Aerosol jet printed, low voltage, electrolyte gated carbon nanotube ring oscillators with sub-5 μs stage delays." *Nano letters* 13.3 (2013), pp. 954–960.

[82] Bongjun Kim, Michael L Geier, Mark C Hersam, and Ananth Dodabalapur. "Inkjet printed circuits on flexible and rigid substrates based on ambipolar carbon nanotubes with high operational stability." *ACS applied materials & interfaces* 7.50 (2015), pp. 27654–27660.

[83] Wenya Xu, Junyan Dou, Jianwen Zhao, Hongwei Tan, Jun Ye, Masayoshi Tange, Wei Gao, Weiwei Xu, Xiang Zhang, Wenrui Guo, et al. "Printed thin film transistors and CMOS inverters based on semiconducting carbon nanotube ink purified by a nonlinear conjugated copolymer." *Nanoscale* 8.8 (2016), pp. 4588–4598.

[84] Qiqi Xu, Jianwen Zhao, Vincenzo Pecunia, Wenya Xu, Chunshan Zhou, Junyan Dou, Weibing Gu, Jian Lin, Lixin Mo, Yanfei Zhao, et al. "Selective conversion from p-type to n-type of printed bottom-gate carbon nanotube thin-film transistors and application in complementary metal–oxide–semiconductor inverters." *ACS applied materials & interfaces* 9.14 (2017), pp. 12750–12758.

[85] Kris Myny. "The development of flexible integrated circuits based on thin-film transistors." *Nature electronics* 1.1 (2018), pp. 30–39.

[86] Subho Dasgupta, Robert Kruk, Norman Mechau, and Horst Hahn. "Inkjet printed, high mobility inorganic-oxide field effect transistors processed at room temperature." *ACS nano* 5.12 (2011), pp. 9628–9638.

[87] Yuzhi Li, Linfeng Lan, Sheng Sun, Zhenguo Lin, Peixiong Gao, Wei Song, Erlong Song, Peng Zhang, and Junbiao Peng. "All inkjet-printed metal-oxide thin-film transistor array with good stability and uniformity using surface-energy patterns." *ACS applied materials & interfaces* 9.9 (2017), pp. 8194–8200.

[88] Bongjun Kim, Jaeyoung Park, Michael L Geier, Mark C Hersam, and Ananth Dodabalapur. "Voltage-controlled ring oscillators based on inkjet printed carbon nanotubes and zinc tin oxide." *ACS applied materials & interfaces* 7.22 (2015), pp. 12009–12014.

[89] Li Ding, Zhiyong Zhang, Shibo Liang, Tian Pei, Sheng Wang, Yan Li, Weiwei Zhou, Jie Liu, and Lian-Mao Peng. "CMOS-based carbon nanotube pass-transistor logic integrated circuits." *Nature communications* 3.1 (2012), pp. 1–7.

[90] Luckshitha Suriyasena Liyanage, Xiaoqing Xu, Greg Pitner, Zhenan Bao, and H-S Philip Wong. "VLSI-compatible carbon nanotube doping technique with low work-function metal oxides." *Nano letters* 14.4 (2014), pp. 1884–1890.

[91] Soo Min Kim, Jin Ho Jang, Ki Kang Kim, Hyeon Ki Park, Jung Jun Bae, Woo Jong Yu, Il Ha Lee, Gunn Kim, Duong Dinh Loc, Un Jeong Kim, et al. "Reduction-controlled viologen in bisolvent as an environmentally stable n-type dopant for carbon nanotubes." *Journal of the American Chemical Society* 131.1 (2009), pp. 327–331.

[92] Jialu Zhang, Chuan Wang, Yue Fu, Yuchi Che, and Chongwu Zhou. "Air-stable conversion of separated carbon nanotube thin-film transistors from p-type to n-type using atomic layer deposition of high-κ oxide and its application in CMOS logic circuits." *Acs Nano* 5.4 (2011), pp. 3284–3292.

[93] Huiliang Wang, Brian Cobb, Albert van Breemen, Gerwin Gelinck, and Zhenan Bao. "Highly Stable Carbon Nanotube Top-Gate Transistors with Tunable Threshold Voltage." *Advanced Materials* 26.26 (2014), pp. 4588–4593.

[94] Mark-Jan Spijkman, Kris Myny, Edsger CP Smits, Paul Heremans, Paul WM Blom, and Dago M De Leeuw. "Dual-gate thin-film transistors, integrated circuits and sensors." *Advanced Materials* 23.29 (2011), pp. 3231–3242.

[95] Bongjun Kim, Kelly Liang, Michael L Geier, Mark C Hersam, and Ananth Dodabalapur. "Enhancement of minority carrier injection in ambipolar carbon nanotube transistors using double-gate structures." *Applied Physics Letters* 109.2 (2016), p. 023515.

[96] GH Gelinck, E Van Veenendaal, and R Coehoorn. "Dual-gate organic thin-film transistors." *Applied Physics Letters* 87.7 (2005), p. 073508.

[97] Kenji Nomura, Toshio Kamiya, and Hideo Hosono. "Ambipolar oxide thin-film transistor." *Advanced Materials* 23.30 (2011), pp. 3431–3434.

[98] Yu-Ming Lin, Hsin-Ying Chiu, Keith A Jenkins, Damon B Farmer, Phaedon Avouris, and Alberto Valdes-Garcia. "Dual-gate graphene FETs with $f\_\{T\}$ of 50 GHz." *IEEE Electron Device Letters* 31.1 (2009), pp. 68–70.

[99] Artem G Shulga, Laura Piveteau, Satria Z Bisri, Maksym V Kovalenko, and Maria A Loi. "Double gate PbS quantum dot field-effect transistors for tuneable electrical characteristics." *Advanced Electronic Materials* 2.4 (2016), p. 1500467.

[100] Yu-Ming Lin, Keith A Jenkins, Alberto Valdes-Garcia, Joshua P Small, Damon B Farmer, and Phaedon Avouris. "Operation of graphene transistors at gigahertz frequencies." *Nano letters* 9.1 (2009), pp. 422–426.

[101] John A Rogers, Takao Someya, and Yonggang Huang. "Materials and mechanics for stretchable electronics." *science* 327.5973 (2010), pp. 1603–1607.

[102] Takao Someya, Tsuyoshi Sekitani, Shingo Iba, Yusaku Kato, Hiroshi Kawaguchi, and Takayasu Sakurai. "A large-area, flexible pressure sensor matrix with organic field-effect transistors for artificial skin applications." *Proceedings of the National Academy of Sciences* 101.27 (2004), pp. 9966–9970.

[103] Xinge Yu, Zhaoqian Xie, Yang Yu, Jungyup Lee, Abraham Vazquez-Guardado, Haiwen Luan, Jasper Ruban, Xin Ning, Aadeel Akhtar, Dengfeng Li, et al. "Skin-integrated wireless haptic interfaces for virtual and augmented reality." *Nature* 575.7783 (2019), pp. 473–479.

[104] Stefan CB Mannsfeld, Benjamin CK Tee, Randall M Stoltenberg, Christopher V HH Chen, Soumendra Barman, Beinn VO Muir, Anatoliy N Sokolov, Colin Reese, and Zhenan Bao. "Highly sensitive flexible pressure sensors with microstructured rubber dielectric layers." *Nature materials* 9.10 (2010), pp. 859–864.

[105] Jeffrey A Kleim, John H Freeman, Rochelle Bruneau, Brian C Nolan, Natalie R Cooper, Alison Zook, and Drew Walters. "Synapse formation is associated with memory storage in the cerebellum." *Proceedings of the National Academy of Sciences* 99.20 (2002), pp. 13228–13231.

[106] Agnès Gruart, Marıa Dolores Muñoz, and José M Delgado-Garcıa. "Involvement of the CA3–CA1 synapse in the acquisition of associative learning in behaving mice." *Journal of Neuroscience* 26.4 (2006), pp. 1077–1087.

[107] Hea-Lim Park, Yeongjun Lee, Naryung Kim, Dae-Gyo Seo, Gyeong-Tak Go, and Tae-Woo Lee. "Flexible neuromorphic electronics for computing, soft robotics, and neuroprosthetics." *Advanced Materials* 32.15 (2020), p. 1903558.

[108] Qingzhou Liu, Yihang Liu, Ji Li, Christian Lau, Fanqi Wu, Anyi Zhang, Zhen Li, Mingrui Chen, Hongyu Fu, Jeffrey Draper, et al. "Fully printed all-solid-state organic flexible artificial synapse for neuromorphic computing." *ACS applied materials & interfaces* 11.18 (2019), pp. 16749–16757.

[109] Yoeri van de Burgt, Ewout Lubberman, Elliot J Fuller, Scott T Keene, Grégorio C Faria, Sapan Agarwal, Matthew J Marinella, A Alec Talin, and Alberto Salleo. "A non-volatile organic electrochemical device as a low-voltage artificial synapse for neuromorphic computing." *Nature materials* 16.4 (2017), pp. 414–418.

[110] F Molina-Lopez, TZ Gao, U Kraft, C Zhu, Thomas Öhlund, Raphael Pfattner, VR Feig, Y Kim, S Wang, Y Yun, et al. "Inkjet-printed stretchable and low voltage synaptic transistor array." *Nature communications* 10.1 (2019), pp. 1–10.

[111] Chuan Wang, Jialu Zhang, Koungmin Ryu, Alexander Badmaev, Lewis Gomez De Arco, and Chongwu Zhou. "Wafer-scale fabrication of separated carbon nanotube thin-film transistors for display applications." *Nano Letters* 9.12 (2009), pp. 4285–4291.

[112] Min Yu, Haochuan Wan, Le Cai, Jinshui Miao, Suoming Zhang, and Chuan Wang. "Fully printed flexible dual-gate carbon nanotube thin-film transistors with tunable ambipolar characteristics for complementary logic circuits." *ACS nano* 12.11 (2018), pp. 11572–11578.

[113] Kunlong Yang, Sijian Yuan, Yuxiang Huan, Jiao Wang, Li Tu, Jiawei Xu, Zhuo Zou, Yiqiang Zhan, Lirong Zheng, and Fernando Seoane. "Tunable flexible artificial synapses: A new path toward a wearable electronic system." *npj Flexible Electronics* 2.1 (2018), pp. 1–9.

[114] Rebecca Sejung Park, Max Marcel Shulaker, Gage Hills, Luckshitha Suriyasena Liyanage, Seunghyun Lee, Alvin Tang, Subhasish Mitra, and H-S Philip Wong. "Hysteresis in carbon nanotube transistors: measurement and analysis of trap density, energy level, and spatial distribution." *ACS nano* 10.4 (2016), pp. 4599–4608.

[115] Joon Sung Lee, Sunmin Ryu, Kwonjae Yoo, Insung S Choi, Wan Soo Yun, and Jinhee Kim. "Origin of gate hysteresis in carbon nanotube field-effect transistors." *The Journal of Physical Chemistry C* 111.34 (2007), pp. 12504–12507.

[116] Woong Kim, Ali Javey, Ophir Vermesh, Qian Wang, Yiming Li, and Hongjie Dai. "Hysteresis caused by water molecules in carbon nanotube field-effect transistors." *Nano Letters* 3.2 (2003), pp. 193–198.

[117] Andrew J Arnold, Ali Razavieh, Joseph R Nasr, Daniel S Schulman, Chad M Eichfeld, and Saptarshi Das. "Mimicking neurotransmitter release in chemical synapses via hysteresis engineering in MoS2 transistors." *ACS nano* 11.3 (2017), pp. 3110–3118.

[118] LF Abbott and Wade G Regehr. "Synaptic computation." *Nature* 431.7010 (2004), pp. 796–803.

[119] Robert S Zucker and Wade G Regehr. "Short-term synaptic plasticity." *Annual review of physiology* 64.1 (2002), pp. 355–405.

[120] Wade G Regehr. "Short-term presynaptic plasticity." *Cold Spring Harbor perspectives in biology* 4.7 (2012), a005702.

[121] Daniel Johnston and Samuel Miao-Sin Wu. *Foundations of cellular neurophysiology.* MIT press, 1994.

[122] Vitaly A Klyachko and Charles F Stevens. "Excitatory and feed-forward inhibitory hippocampal synapses work synergistically as an adaptive filter of natural spike trains." *PLoS Biol* 4.7 (2006), e207.

[123] Debarghya Sarkar, Jun Tao, Wei Wang, Qingfeng Lin, Matthew Yeung, Chenhao Ren, and Rehan Kapadia. "Mimicking biological synaptic functionality with an indium phosphide synaptic device on silicon for scalable neuromorphic computing." *ACS nano* 12.2 (2018), pp. 1656–1663.

[124] Changjin Wan, Pingqiang Cai, Ming Wang, Yan Qian, Wei Huang, and Xiaodong Chen. "Artificial sensory memory." *Advanced Materials* 32.15 (2020), p. 1902434.

[125] Haochuan Wan, Yunqi Cao, Li-Wei Lo, Junyi Zhao, Nelson Sepulveda, and Chuan Wang. "Flexible carbon nanotube synaptic transistor for neurological electronic skin applications." *ACS nano* 14.8 (2020), pp. 10402–10412.

[126] Yei Hwan Jung, Byeonghak Park, Jong Uk Kim, and Tae-il Kim. "Bioinspired electronics for artificial sensory systems." *Advanced Materials* 31.34 (2019), p. 1803637.

[127] Leilei Gu, Swapnadeep Poddar, Yuanjing Lin, Zhenghao Long, Daquan Zhang, Qianpeng Zhang, Lei Shu, Xiao Qiu, Matthew Kam, Ali Javey, et al. "A biomimetic eye with a hemispherical perovskite nanowire array retina." *Nature* 581.7808 (2020), pp. 278–282.

[128] Lukas Mennel, Joanna Symonowicz, Stefan Wachter, Dmitry K Polyushkin, Aday J Molina-Mendoza, and Thomas Mueller. "Ultrafast machine vision with 2D material neural network image sensors." *Nature* 579.7797 (2020), pp. 62–66.

[129] Seunghwan Seo, Seo-Hyeon Jo, Sungho Kim, Jaewoo Shim, Seyong Oh, Jeong-Hoon Kim, Keun Heo, Jae-Woong Choi, Changhwan Choi, Saeroonter Oh, et al. "Artificial optic-neural synapse for colored and color-mixed pattern recognition." *Nature communications* 9.1 (2018), pp. 1–8.

[130] Jia Sun, Seyong Oh, Yongsuk Choi, Seunghwan Seo, Min Jun Oh, Minhwan Lee, Won Bo Lee, Pil J Yoo, Jeong Ho Cho, and Jin-Hong Park. "Optoelectronic synapse based on igzo-alkylated graphene oxide hybrid structure." *Advanced Functional Materials* 28.47 (2018), p. 1804397.

[131] Srilakshmi Subramanian Periyal, Metikoti Jagadeeswararao, Si En Ng, Rohit Abraham John, and Nripan Mathews. "Halide Perovskite Quantum Dots Photosensitized-Amorphous Oxide Transistors for Multimodal Synapses." *Advanced Materials Technologies* 5.11 (2020), p. 2000514.

[132] Yeongjun Lee, Jin Young Oh, Wentao Xu, Onnuri Kim, Taeho Roy Kim, Jiheong Kang, Yeongin Kim, Donghee Son, Jeffery B-H Tok, Moon Jeong Park, et al. "Stretchable organic optoelectronic sensorimotor synapse." *Science advances* 4.11 (2018), eaat7387.

[133] Mohammad Karbalaei Akbari and Serge Zhuiykov. "A bioinspired optoelectronically engineered artificial neurorobotics device with sensorimotor functionalities." *Nature communications* 10.1 (2019), pp. 1–10.

[134] Richard C Atkinson and Richard M Shiffrin. "Human memory: A proposed system and its control processes." *Psychology of learning and motivation*. Vol. 2. Elsevier, 1968, pp. 89–195.

[135] Takeo Ohno, Tsuyoshi Hasegawa, Tohru Tsuruoka, Kazuya Terabe, James K Gimzewski, and Masakazu Aono. "Short-term plasticity and long-term potentiation mimicked in single inorganic synapses." *Nature materials* 10.8 (2011), pp. 591–595.

[136] Xiaolei Liu, Zhicheng Luo, Song Han, Tao Tang, Daihua Zhang, and Chongwu Zhou. "Band engineering of carbon nanotube field-effect transistors via selected area chemical gating." *Applied Physics Letters* 86.24 (2005), p. 243501.

[137] Brett Lee Allen, Padmakar D Kichambare, and Alexander Star. "Carbon nanotube field-effect-transistor-based biosensors." *Advanced Materials* 19.11 (2007), pp. 1439–1451.

[138]   Koen Besteman, Jeong-O Lee, Frank GM Wiertz, Hendrik A Heering, and Cees Dekker. "Enzyme-coated carbon nanotubes as single-molecule biosensors." *Nano letters* 3.6 (2003), pp. 727–730.

[139]   Alexander Star, Vikram Joshi, Tzong-Ru Han, M Virginia P Altoé, George Grüner, and J Fraser Stoddart. "Electronic detection of the enzymatic degradation of starch." *Organic letters* 6.13 (2004), pp. 2089–2092.

[140]   Alexander Star, Jean-Christophe P Gabriel, Keith Bradley, and George Grüner. "Electronic detection of specific protein binding using nanotube FET devices." *Nano letters* 3.4 (2003), pp. 459–463.

[141]   Alexander Star, Eugene Tu, Joseph Niemann, Jean-Christophe P Gabriel, C Steve Joiner, and Christian Valcke. "Label-free detection of DNA hybridization using carbon nanotube network field-effect transistors." *Proceedings of the National Academy of Sciences* 103.4 (2006), pp. 921–926.